Summer 8-15-2016

Synthesis of Two-Dimensional Copper Indium Disulfide Nanocrystals and Study of Exciton Splitting in Thin Nanosheets

Linjia Mu
Washington University in St. Louis

Recommended Citation

Mu, Linjia, "Synthesis of Two-Dimensional Copper Indium Disulfide Nanocrystals and Study of Exciton Splitting in Thin Nanosheets" (2016). *Arts & Sciences Electronic Theses and Dissertations*. 875.
https://openscholarship.wustl.edu/art_sci_etds/875

WASHINGTON UNIVERSITY IN ST. LOUIS

Department of Chemistry

Dissertation Examination Committee:
William E. Buhro, Chair
Richard A. Loomis
Liviu Mirica
Bryce Sadtler
Li Yang

Synthesis of Two-Dimensional Copper Indium Disulfide Nanocrystals and Study of Exciton Splitting in Thin Nanosheets

by
Linjia Mu

A dissertation presented to the
Graduate School of Arts & Sciences
of Washington University in
partial fulfillment of the
requirements for the degree
of Doctor of Philosophy

August 2016
St. Louis, Missouri

Table of Contents

List of Figures

Chapter 2 Synthesis of Copper Indium Disulfide Nanoplatelets by a One-pot Method

Chapter 3 Influence of the Nanoscale Kirkendall Effect on the Morphology of Copper Indium Disulfide Nanoplatelets Synthesized by Ion Exchange

Chapter 4 Exciton Splitting in Thin Copper Indium Disulfide Nanosheets

List of Tables

Chapter 2 Synthesis of Copper Indium Disulfide Nanoplatelets by a One-pot Method

Chapter 3 Influence of the Nanoscale Kirkendall Effect on the Morphology of Copper Indium Disulfide Nanoplatelets Synthesized by Ion Exchange

Chapter 4 Exciton Splitting in Thin Copper Indium Disulfide Nanosheets

List of Abbreviations

EDS	energy-dispersive X-ray spectroscopy
HRTEM	high-resolution transmission electron microscope
ML	monolayer
NP	nanoplatelet
PL	photoluminescence
TEM	transmission electron microscope
XRD	X-ray diffraction
2D	two-dimensional

Acknowledgments

First of all, I would like to express my sincere and deepest gratitude to my research advisor, Professor William E. Buhro, for his wise and patient guidance and passionate encouragement throughout my graduate research. He has always been so supportive to my ideas and constantly provided constructive suggestions. I thank Professor Buhro for being such a great teacher and my role model as a scientist, and I'm so grateful to work for him.

I would like to thank Professor Richard A. Loomis and Professor Liviu Mirica for taking the time to attend my annual committee meetings and serving as my dissertation committee members, providing much helpful advice to my research projects. I would also like to thank Professor Bryce Sadtler and Professor Li Yang for serving as my dissertation committee members and all the helpful discussions in the group meetings. Additionally, I thank Professor Richard A. Loomis for his help with spectroscopy, and Professor Li Yang for the theoretical calculations of the exciton splitting to confirm my experimental observations.

I'm very grateful for the help from the former and present members in Buhro group and Loomis group. I especially thank Dr. Fudong Wang for being a great mentor and continuously providing valuable suggestions and help throughout my research. Any many thanks to Dr. Paul J. Morrison, Dr. Yuanyuan Wang, Dr. Waynie M. Schuette and Yang Zhou for their help and discussions about experiments.

I would like to express my appreciation to Department of Chemistry for the opportunity to do my graduate study and research here, and to Dr. Ed Hiss, Dr. Rachel Dunn, Karen Klein, Barbara Tessmer, Jessica Owens, Greg Noelken, Phyllis Noelken and all the other department staff members for their assistance.

My special thanks go to my parents for their unconditional love and support throughout my life, and for always encouraging me to fulfill my dreams. I would also like to thank all my family for keeping thinking about me far from home and celebrating my progress. And thanks to all my friends, old and new, for accompanying me through success and frustrations during my graduate studies.

Lastly, I would like to thank Washington University in St. Louis and National Science Foundation for the financial support for my research projects.

Linjia Mu

Washington University in St. Louis

May 2016

Dedicated to my family and friends.

ABSTRACT OF THE DISSERTATION

Synthesis of Two-Dimensional Copper Indium Disulfide Nanocrystals and Study of Exciton Splitting in Thin Nanosheets

by

Linjia Mu

Doctor of Philosophy in Chemistry

Washington University in St. Louis, 2016

Professor William E. Buhro, Chair

This dissertation presents the preparation of two-dimensional (2D) $CuInS_2$ nanocrystals by the ion-exchange method and the exciton splitting observed in thin $CuInS_2$ nanosheets.

After monitoring the one-pot synthesis of $CuInS_2$ by energy-dispersive X-ray spectroscopy (EDS), an ion-exchange method is developed as an improvement for the synthesis of $CuInS_2$ nanocrystals, to control the morphology and size. $CuInS_2$ nanocrystals are prepared by ion exchange with template $Cu_{2-x}S$ nanoplatelets and InX_3 [X = chloride, iodide, acetate (OAc), or acetylacetonate (acac)]. The morphologies of the resultant nanocrystals depend on the InX_3 precursor and the reaction temperature. Exchange with $InCl_3$ at 150 ℃ produces $CuInS_2$ nanoplatelets having central holes and thickness variations, whereas the exchange at 200 ℃ produces intact $CuInS_2$ nanoplatelets in which the initial morphology is preserved. Exchange with InI_3 at 150 ℃ produces $CuInS_2$ nanoplatelets in which the central hollowing is more extreme, whereas exchange with $In(OAc)_3$ or $In(acac)_3$ at 150 ℃ produces intact $CuInS_2$ nanoplatelets. The results establish that the ion exchange occurs through the thin nanoplatelet edge facets. The hollowing and hole formation are due to a nanoscale Kirkendall Effect

operating in the reaction-limited regime for displacement of X^- at the edges, to allow insertion of In^{3+} into the template nanoplatelets.

Additionally, nanosheets of $Cu_{2-x}S$ having discrete thicknesses of 5, 6, and 8 crystallographic monolayers (MLs) are prepared by adaptation of literature methods. These are converted to $CuInS_2$ nanosheets having the same, discrete, monolayer thicknesses by cation-exchange reactions. The 6- and 8-monolayer $CuInS_2$ nanosheets exhibit broad, nearly featureless extinction (absorption) spectra that are generally characteristic of $CuInS_2$ nanocrystals. However, the thinnest, 5-ML $CuInS_2$ nanosheets exhibit structured extinction spectra having a well-resolved doublet feature with peaks at 2.74 and 2.54 eV. An exciton-splitting (valence-band-splitting) model assigns the transitions to excitons derived from inequivalent A, B, and C holes from the bulk band structure of $CuInS_2$. This splitting is analogous to the heavy-hole, light-hole splitting observed in the absorption spectra of III-V quantum wells, and pseudo-2D II-VI nanocrystals. The model semi-quantitatively accounts for the magnitude of the observed splitting, which is largely due to quantum confinement and the differing A, B, and C hole effective masses. The model also accounts for the lack of resolved splitting in $CuInS_2$ nanocrystals having larger dimensions.

Chapter 1

Introduction

In this dissertation, preparation of two-dimensional (2D) $CuInS_2$ nanocrystals is reported, by both a direct one-pot method (Chapter 2) and an ion-exchange method with template $Cu_{2-x}S$ nanocrystals (Chapter 3 and 4). Monitoring the reaction process by energy-dispersive X-ray spectroscopy (EDS) during the direct one-pot synthesis of $CuInS_2$ nanoplatelets (NPs) indicated that binary $Cu_{2-x}S$ nanocrystals were formed first, followed by In^{3+} incorporation and conversion to $CuInS_2$ NPs. With previous reports about growth mechanisms of multinary nanocrystals[1-4] and our observations in the one-pot synthesis, an ion-exchange method was developed for $CuInS_2$ NPs.

The initial preparation of binary $Cu_{2-x}S$ NPs (13 nm mean thickness) to serve as the template was followed by purposeful ion exchange using indium precursors to afford the $CuInS_2$ composition (Chapter 3). The morphologies of $CuInS_2$ nanocrystals by the ion-exchange method were found to be remarkably dependent on the exchange temperature and the indium precursor used. Intact $CuInS_2$ NPs preserving the sizes and morphologies of the template $Cu_{2-x}S$ NPs were produced with higher exchange temperatures and/or more-ionic indium precursors, while hollow-centered $CuInS_2$ nanocrystals were produced otherwise as a result of the nanoscale Kirkendall Effect.

We further prepared thin $CuInS_2$ nanosheets by ion exchange with $Cu_{2-x}S$ nanosheets (≈2 nm thickness), to study one-dimensional (quantum-well-like) quantum confinement effects in $CuInS_2$ nanosheets (Chapter 4). Thin $Cu_{2-x}S$ nanosheets of three different thicknesses were prepared following a similar reaction as that noted above for thick $Cu_{2-x}S$ NPs (13 nm mean thickness), with $SnBr_4$ or HCl as the nanosheet-morphology-control additive. The extinction (absorption) spectra of $CuInS_2$ nanosheets prepared by ion exchange with these thin $Cu_{2-x}S$ nanosheets were collected. Blue shifting of extinction features was observed in all three spectra compared with bulk $CuInS_2$ and thick $CuInS_2$ NPs. Exciton splitting was clearly evident for the thinnest $CuInS_2$ nanosheets.

1.1 I-III-VI_2 Semiconductor Nanomaterials

Considerable interest has focused on I-III-VI_2 semiconductor nanomaterials with direct, size tunable bandgaps in the red to near-infrared region for applications in many aspects, especially in solar-energy conversion.[5-12] I-III-VI_2 semiconductor materials, including $CuInS_2$, $CuInSe_2$ and $CuIn_xGa_{1-x}Se_2$ (CIGS), have been regarded as promising effective light-absorbing materials for thin-film solar cells[13] because of the broad color window covered in the solar spectrum and high optical absorption coefficients ($\sim 10^5$ cm^{-1}).[6,14] Furthermore, I-III-VI_2 semiconductors mostly consist of earth-abundant and less/non-toxic elements, which lower the manufacturing costs and cause less environmental impact. As of September 2014, the CIGS solar cell has reached conversion efficiency record of 21.7%.[15] A new record of 22.3% efficiency was achieved by Solar Frontier in December 2015.[16]

The traditional fabrication processes of solar cells containing I-III-VI_2 semiconductors include a coevaporation process of all element sources, which result in high manufacturing costs.[17,18] An alternative approach has been proposed, which is to create a nanocrystal ink by dispersing pre-synthesized I-III-VI_2 nanocrystals with desired stoichiometry and crystal phase in solvents.[13,19] The nanocrystal inks may be easily deposited using a series of solution-based processing techniques, leading to the development of low-cost solar cells.[13]

$CuInS_2$ is an important and relatively simple representative of I-III-VI_2 semiconductor nanomaterials. It has a direct bandgap of 1.53 eV and exciton Bohr radius of 4 nm.[20] Although the ordered chalcopyrite structure is thermodynamically the most stable phase at room temperature for bulk $CuInS_2$,[21] wurtzite[11,22-24] and zinc blende[25,26] phases have also been identified and frequently observed for $CuInS_2$ nanocrystals, after the first report by Pan et al.[27] The zinc blende structure is closely related to chalcopyrite structure, forming a cubic close-packed S^{2-} sublattice in both. Above a critical temperature, the chalcopyrite structure transforms to the zinc blende structure in which Cu^+ and In^{3+} occupy the cation positions randomly.[11,21,27,28] The wurtzite structure is a hexagonal analog of zinc blende with disordered cations as well.[11,27] The $CuInS_2$ nanocrystals studied in this work possess the cation-disorderd wurtzite or closely related cation-ordered orthorhombic structure, which we show to be favored by the ion-exchange process.

We are particularly interested in pseudo-1D and pseudo-2D nanocrystals, such as nanowires,[29-31] nanobelts,[32,33] or nanosheets, for their potential to transport energy and charge without the requirement of interfacial hopping between nanocrystals. Therefore, 2D $CuInS_2$ nanocrystals attract our attention and are chosen as our research subject in this work.

1.2 Synthetic Methods for Copper(I) Indium Sulfide ($CuInS_2$) and related I-III-VI_2 Semiconductor Nanomaterials

Several solution-based, direct synthetic methods for I-III-VI_2 semiconductor nanomaterials have been reported, including the heat-up method[1,22,25] the hot-injection method,[13,19,34-37] hydro/solvothermal techniques,[11,38,39] and single-source precursor decomposition.[5,40,41] However, with limited understanding of and control over reaction kinetics, the size and morphology control of I-III-VI_2 nanocrystals synthesized by these direct methods are usually complicated by the unbalanced reactivities of the different precursors or the choice and preparation of a single-source precursor.[42,43] Furthermore, growth-mechanism studies indicated that in many cases, binary nanocrystals are formed first, which convert to the desired multinary compounds by the incorporation of other ions (Chapter 2).[1-4] Thus, a new approach has been studied extensively for more than one decade, involving the initial preparation of binary nanocrystals as template nanocrystals followed by purposeful ion exchange to afford the target multinary composition.

Cation exchange has attracted much more attention than anion exchange because their relatively large size makes anions less mobile and the exchange of anions more difficult.[43,44] Here we mainly discuss cation exchange and may refer to it as ion exchange hereinafter in this dissertation.

Cation exchange involves substitution of cations in a template crystal by other cations with the anion sublattice retained.[42,44] A cation exchange-process for nanocrystals was first reported in the 1990s for synthesizing core-shell nanostructures,[45,46] and has developed rapidly since the Alivisatos group demonstrated the size-dependent shape change throughout the exchange process.[47] In their study, a critical size was identified during the conversion of CdE → Ag_2E → CdE (E = S, Se, Te) by cation exchange, above which the morphologies of the nanocrystals are preserved during the cation-exchange process.[47] After that, cation-exchange reactions of various systems have been reported with conserved nanocrystal morphologies throughout the process, including CdS → CdS-Ag_2S → Ag_2S nanorods,[48] CdE → PdE (or PtE_2, E = S, Se, Te),[49] CdS → Cu_2S nanorods,[50] Cu_2S → CdS sphere particles,[51] Cu_2S → PbS sphere particles,[51] CdS → Cu_2S → PbS nanorods,[51] CdS-Ag_2S → CdS-PbS nanorods,[51] CdSe/CdS → Cu_2Se/Cu_2S → PbSe/PbS nanorods,[52] CdS → Cu_2S → ZnS (or PbS) NPs,[53] CdSe/CdS → Cu_2Se/Cu_2S → ZnSe/ZnS (or PbSe/PbS) core/shell NPs,[53] $Cu_{2-x}Se/Cu_{2-x}S$ → $HgSe/Cu_{2-x}S$(or $Ag_2Se/Cu_{2-x}S$) core/shell nanorods,[54] Cd_3As_2 → GaAs (or InAs) quantum dots,[55] Cd_3P_2 → GaP (or InP) quantum dots,[55] and $Cu_{3-x}P$ → InP NPs.[56] The thermodynamic driving force for the cation-exchange reaction was proposed to be different solvation energies of the exchanging cations in a specific coordinating solvent.[43,51] In most of the cases described above, when a soft metal ion (Cu^+, Ag^+, Hg^{2+}, Pd^{2+}, Pt^{4+}) is exchanged with a hard metal ion (Cd^{2+}, Pb^{2+}, Zn^{2+}, In^{3+}, Ga^{3+}), a soft base (tributylphosphine[47,51-53] or trioctylphosphine[53,55,56]) is used as the solvent, which preferentially binds with a soft acid (metal ion).[43,51] The case of Cd^{2+} exchanged with In^{3+} and Ga^{3+} also follows this trend because In^{3+} and Ga^{3+} are harder ions relative to Cd^{2+}.[55] In the reverse-direction exchange, a hard base (methanol[47-54] or water[49]) is employed as the solvent, to facilitate the out-diffusion of a hard metal ion.[43,51]

However, the cation-exchange processes involved in the cases above are all complete exchange between binary compounds, resulting in a different binary material or a segmented structure. More recently, partial ion exchange with binary compounds to afford multinary compositions has been reported by several research groups.[23,24,57] Donega and coworkers prepared $CuInS_2$ nanocrystals by partial indium-cation exchange into small $Cu_{2-x}S$ dot-like nanocrystals.[23] Lesnyak and coworkers reported similar observations at about the same time[24] and also a related partial zinc and tin cation-exchange process with anisotropic $Cu_{2-x}S_ySe_{1-y}$ NPs.[57]

In this work, our purpose is to prepare 2D $CuInS_2$ nanocrystals by ion exchange while the morphology is preserved from the template $Cu_{2-x}S$ nanocrystals (Chapters 3 and 4). Among the most common Cu_2S-related phases, hexagonal high chalcocite (Cu_2S), monoclinic low chalcocite (Cu_2S) and monoclinic djurleite ($Cu_{2-x}S$, $x \approx 0.03 – 0.07$) are most closely related to this work.[58] Sulfur atoms form hexagonal-close-packed sublattices in all of the three structures, as is in the wurtzite $CuInS_2$ structure.[59] Low chalcocite and djurleite structures are very similar and often found to be intermixed or intergrown.[59,60] Both of them transform to high chalcocite above 105

℃, in which Cu^+ ions are highly mobile.[59,61] Due to the same anion (S^{2-}) sublattice and closely related crystal structures of $Cu_{2-x}S$ and wurtzite $CuInS_2$, the high mobility of Cu^+ in $Cu_{2-x}S$ and the similar sizes of Cu^+ and In^{3+},[22] $Cu_{2-x}S$ readily undergoes cation exchange reactions and is chosen as the template to form $CuInS_2$, as in most of the previous reports.[23,24,57]

1.3 Optical Properties of Copper(I) Indium Sulfide ($CuInS_2$) Nanocrystals

To explore the applications of $CuInS_2$ nanocrystals for solar-energy conversion, it is important to understand their optical properties. Binary semiconductor nanomaterials, such as CdSe,[32,62-64] InP,[65,66] and PbS,[67] often display well-resolved absorption features. However, the extinction spectra of $CuInS_2$ nanocrystals typically consist of a rising absorption profile towards higher energy with a very broad peak.[34,68-70] The absorption feature shows a blue shift with decreased size of the nanocrystals as a result of stronger quantum confinement,[34,68,71] and becomes better defined upon zinc treatment.[71] The low resolution of these extinction spectra has been ascribed to nanocrystal size non-uniformity, morphological variations, and compositional inhomogeneities.[34,70,71]

Exciton splitting has been observed in bulk crystals of $CuGa_xIn_{1-x}S_2$ ($x = 0 – 1$),[72-75] but to our knowledge not previously in I-III-VI_2 nanocrystals. We now show resolved transitions in the extinction spectra of $CuInS_2$ nanosheets due to the energy splitting between closely spaced excitons from the bulk band structure (Chapter 4). The energy splitting between these excitons is enhanced in very thin $CuInS_2$ nanosheets by quantum-confinement effects, allowing the corresponding absorption features to be partially resolved.

$CuInS_2$ nanocrystals generally display a broad photoluminescence (PL) feature with a large Stokes shift and long decay times, and also show size dependence in the PL feature following the same trend as the extinction spectra.[70,76,77] In a recent review on copper chalcogenide nanocrystals, Donega and coworkers[70] sorted the proposed origins of the characteristic PL into four categories based on previous studies, including recombination of localized electrons and holes originated from native point defects;[78,79] recombination of delocalized electron with localized holes;[69,77] radiative recombination of delocalized holes with localized electrons;[80,81] and the 1S(e) → 1S(h) exciton transition involving delocalized holes and electrons.[82] Each pathway can explain some observations but not the other, or its assumptions have not yet been verified by experiments. Therefore, the mechanism is still under debate and requires further research.

1.4 References

1. Connor, S. T.; Hsu, C.-M.; Weil, B. D.; Aloni, S.; Cui, Y. *J. Am. Chem. Soc.* **2009**, *131*, 4962.

2. Tan, J. M. R.; Lee, Y. H.; Pedireddy, S.; Baikie, T.; Ling, X. Y.; Wong, L. H. *J. Am. Chem. Soc.* **2014**, *136*, 6684.

3. Ahmadi, M.; Pramana, S. S.; Xi, L.; Boothroyd, C.; Lam, Y. M.; Mhaisalkar, S. *J. Phys. Chem. C* **2012**, *116*, 8202.

4. Collord, A. D.; Hillhouse, H. W. *Chem. Mater.* **2015**, *27*, 1855.

5. Wooten, A. J.; Werder, D. J.; Williams, D. J.; Casson, J. L.; Hollingsworth, J. A. *J. Am. Chem. Soc.* **2009**, *131*, 16177.

6. Xu, J.; Lee, C.-S.; Tang, Y.-B.; Chen, X.; Chen, Z.-H.; Zhang, W.-J.; Lee, S.-T.; Zhang, W.; Yang, Z. *ACS Nano* **2010**, *4*, 1845.

7. Li, Q.; Zou, C.; Zhai, L.; Zhang, L.; Yang, Y.; Chen, X.; Huang, S. *CrystEngComm* **2013**, *15*, 1806.

8. Choi, Y.; Beak, M.; Yong, K. *Nanoscale* **2014**, *6*, 8914.

9. Wu, X.-J.; Huang, X.; Qi, X.; Li, H.; Li, B.; Zhang, H. *Angew. Chem., Int. Ed.* **2014**, *53*, 8929.

10. Li, Q.; Zhai, L.; Zou, C.; Huang, X.; Zhang, L.; Yang, Y.; Chen, X.; Huang, S. *Nanoscale* **2013**, *5*, 1638.

11. Qi, Y.; Liu, Q.; Tang, K.; Liang, Z.; Ren, Z.; Liu, X. *J. Phys. Chem. C* **2009**, *113*, 3939.

12. Sheng, X.; Wang, L.; Luo, Y.; Yang, D. *Nanoscale Res. Lett.* **2011**, *6*, 562.

13. Panthani, M. G.; Akhavan, V.; Goodfellow, B.; Schmidtke, J. P.; Dunn, L.; Dodabalapur, A.; Barbara, P. F.; Korgel, B. A. *J. Am. Chem. Soc.* **2008**, *130*, 16770.

14. Rockett, A.; Birkmire, R. W. *J. Appl. Phys.* **1991**, *70*, R81.

15. Jackson, P.; Hariskos, D.; Wuerz, R.; Kiowski, O.; Bauer, A.; Friedlmeier, T. M.; Powalla, M. *Phys. Status Solidi RRL* **2015**, *9*, 28.

16. Solar Frontier News Home Page. http://www.solar-frontier.com/eng/news/2015/C051171.html (Accessed Dec 8. 2015)

17. Contreras, M. A.; Egaas, B.; Ramanathan, K.; Hiltner, J.; Swartzlander, A.; Hasoon, F.; Noufi, R. *Prog. Photovoltaics* **1999**, *7*, 311.

18. Repins, I.; Contreras, M. A.; Egaas, B.; DeHart, C.; Scharf, J.; Perkins, C. L.; To, B.; Noufi, R. *Prog. Photovoltaics* **2008**, *16*, 235.

19. Guo, Q.; Kim, S. J.; Kar, M.; Shafarman, W. N.; Birkmire, R. W.; Stach, E. A.; Agrawal, R.; Hillhouse, H. W. *Nano Lett.* **2008**, *8*, 2982.

20. Czekelius, C.; Hilgendorff, M.; Spanhel, L.; Bedja, I.; Lerch, M.; Müller, G.; Bloeck, U.; Su, D.-S.; Giersig, M. *Adv. Mater.* **1999**, *11*, 643.

21. Binsma, J. J. M.; Giling, L. J.; Bloem, J. *J. Cryst. Growth* **1980**, *50*, 429.

22. Lu, X.; Zhuang, Z.; Peng, Q.; Li, Y. *CrystEngComm* **2011**, *13*, 4039.

23. van der Stam, W.; Berends, A. C.; Rabouw, F. T.; Willhammar, T.; Ke, X.; Meeldijk, J. D.; Bals, S.; de Mello Donega, C. *Chem. Mater.* **2015**, *27*, 621.

24. Akkerman, Q. A.; Genovese, A.; George, C.; Prato, M.; Moreels, I.; Casu, A.; Marras, S.; Curcio, A.; Scarpellini, A.; Pellegrino, T.; Manna, L.; Lesnyak, V. *ACS Nano* **2015**, *9*, 521.

25. Nose, K.; Soma, Y.; Omata, T.; Otsuka-Yao-Matsuo, S. *Chem. Mater.* **2009**, *21*, 2607.

26. Yue, W.; Han, S.; Peng, R.; Shen, W.; Geng, H.; Wu, F.; Tao, S.; Wang, M. *J. Mater. Chem.* **2010**, *20*, 7570.

27. Pan, D.; An, L.; Sun, Z.; Hou, W.; Yang, Y.; Yang, Z.; Lu, Y. *J. Am. Chem. Soc.* **2008**, *130*, 5620.

28. Binsma, J. J. M.; Giling, L. J.; Bloem, J. *Phys. Status Solidi A* **1981**, *63*, 595.

29. Glennon, J. J.; Tang, R.; Buhro, W. E.; Loomis, R. A. *Nano Lett.* **2007**, *7*, 3290.

30. Wayman, V. L.; Morrison, P. J.; Wang, F.; Tang, R.; Buhro, W. E.; Loomis, R. A. *J. Phys. Chem. Lett.* **2012**, *3*, 2627.

31. Liu, Y.-H.; Wang, F.; Hoy, J.; Wayman, V. L.; Steinberg, L. K.; Loomis, R. A.; Buhro, W. E. *J. Am. Chem. Soc.* **2012**, *134*, 18797.

32. Liu, Y.-H.; Wayman, V. L.; Gibbons, P. C.; Loomis, R. A.; Buhro, W. E. *Nano Lett.* **2010**, *10*, 352.

33. Liu, Y.-H.; Wang, F.; Wang, Y.; Gibbons, P. C.; Buhro, W. E. *J. Am. Chem. Soc.* **2011**, *133*, 17005.

34. Xie, R.; Rutherford, M.; Peng, X. *J. Am. Chem. Soc.* **2009**, *131*, 5691.

35. Koo, B.; Patel, R. N.; Korgel, B. A. *Chem. Mater.* **2009**, *21*, 1962.

36. Kruszynska, M.; Borchert, H.; Parisi, J.; Kolny-Olesiak, J. *J. Am. Chem. Soc.* **2010**, *132*, 15976.

37. Norako, M. E.; Franzman, M. A.; Brutchey, R. L. *Chem. Mater.* **2009**, *21*, 4299.

38. Du, W.; Qian, X.; Yin, J.; Gong, Q. *Chem. - Eur. J.* **2007**, *13*, 8840.

39. Wang, D.; Zheng, W.; Hao, C.; Peng, Q.; Li, Y. *Chem. Commun.* **2008**, 2556.

40. Castro, S. L.; Bailey, S. G.; Raffaelle, R. P.; Banger, K. K.; Hepp, A. F. *Chem. Mater.* **2003**, *15*, 3142.

41. Castro, S. L.; Bailey, S. G.; Raffaelle, R. P.; Banger, K. K.; Hepp, A. F. *J. Phys. Chem. B* **2004**, *108*, 12429.

42. Beberwyck, B. J.; Surendranath, Y.; Alivisatos, A. P. *J. Phys. Chem. C* **2013**, *117*, 19759.

43. De Trizio, L.; Manna, L. *Chem. Rev.* **2016**.

44. Rivest, J. B.; Jain, P. K. *Chem. Soc. Rev.* **2013**, *42*, 89.

45. Zhou, H. S.; Sasahara, H.; Honma, I.; Komiyama, H.; Haus, J. W. *Chem. Mater.* **1994**, *6*, 1534.

46. Mews, A.; Eychmueller, A.; Giersig, M.; Schooss, D.; Weller, H. *J. Phys. Chem.* **1994**, *98*, 934.

47. Son, D. H.; Hughes, S. M.; Yin, Y.; Paul Alivisatos, A. *Science* **2004**, *306*, 1009.

48. Robinson, R. D.; Sadtler, B.; Demchenko, D. O.; Erdonmez, C. K.; Wang, L.-W.; Alivisatos, A. P. *Science* **2007**, *317*, 355.

49. Wark, S. E.; Hsia, C.-H.; Son, D. H. *J. Am. Chem. Soc.* **2008**, *130*, 9550.

50. Sadtler, B.; Demchenko, D. O.; Zheng, H.; Hughes, S. M.; Merkle, M. G.; Dahmen, U.; Wang, L.-W.; Alivisatos, A. P. *J. Am. Chem. Soc.* **2009**, *131*, 5285.

51. Luther, J. M.; Zheng, H.; Sadtler, B.; Alivisatos, A. P. *J. Am. Chem. Soc.* **2009**, *131*, 16851.

52. Jain, P. K.; Amirav, L.; Aloni, S.; Alivisatos, A. P. *J. Am. Chem. Soc.* **2010**, *132*, 9997.

53. Bouet, C.; Laufer, D.; Mahler, B.; Nadal, B.; Heuclin, H.; Pedetti, S.; Patriarche, G.; Dubertret, B. *Chem. Mater.* **2014**, *26*, 3002.

54. Miszta, K.; Gariano, G.; Brescia, R.; Marras, S.; De Donato, F.; Ghosh, S.; De Trizio, L.; Manna, L. *J. Am. Chem. Soc.* **2015**, *137*, 12195.

55. Beberwyck, B. J.; Alivisatos, A. P. *J. Am. Chem. Soc.* **2012**, *134*, 19977.

56. De Trizio, L.; Gaspari, R.; Bertoni, G.; Kriegel, I.; Moretti, L.; Scotognella, F.; Maserati, L.; Zhang, Y.; Messina, G. C.; Prato, M.; Marras, S.; Cavalli, A.; Manna, L. *Chem. Mater.* **2015**, *27*, 1120.

57. Lesnyak, V.; George, C.; Genovese, A.; Prato, M.; Casu, A.; Ayyappan, S.; Scarpellini, A.; Manna, L. *ACS Nano* **2014**, *8*, 8407.

58. Potter, R. W. *Econ. Geol.* **1977**, *72*, 1524.

59. Evans, H. T., Jr. *Z. Kristallogr.* **1979**, *150*, 299.

60. Evans, H. T., Jr. *Science* **1979**, *203*, 356.

61. Buerger, M. J.; Wuensch, B. J. *Science* **1963**, *141*, 276.

62. Joo, J.; Son, J. S.; Kwon, S. G.; Yu, J. H.; Hyeon, T. *J. Am. Chem. Soc.* **2006**, *128*, 5632.

63. Ithurria, S.; Dubertret, B. *J. Am. Chem. Soc.* **2008**, *130*, 16504.

64. Wang, F.; Wang, Y.; Liu, Y.-H.; Morrison, P. J.; Loomis, R. A.; Buhro, W. E. *Acc. Chem. Res.* **2015**, *48*, 13.

65. Battaglia, D.; Peng, X. *Nano Lett.* **2002**, *2*, 1027.

66. Gary, D. C.; Terban, M. W.; Billinge, S. J. L.; Cossairt, B. M. *Chem. Mater.* **2015**, *27*, 1432.

67. Morrison, P. J.; Loomis, R. A.; Buhro, W. E. *Chem. Mater.* **2014**, *26*, 5012.

68. Zhong, H.; Lo, S. S.; Mirkovic, T.; Li, Y.; Ding, Y.; Li, Y.; Scholes, G. D. *ACS Nano* **2010**, *4*, 5253.

69. Li, L.; Pandey, A.; Werder, D. J.; Khanal, B. P.; Pietryga, J. M.; Klimov, V. I. *J. Am. Chem. Soc.* **2011**, *133*, 1176.

70. van der Stam, W.; Berends, A. C.; de Mello Donega, C. *ChemPhysChem* **2016**, *17*, 559.

71. So, D.; Konstantatos, G. *Chem. Mater.* **2015**, *27*, 8424.

72. Syrbu, N. N.; Tiginyanu, I. M.; Nemerenco, L. L.; Ursaki, V. V.; Tezlevan, V. E.; Zalamai, V. V. *J. Phys. Chem. Solids* **2005**, *66*, 1974.

73. Eberhardt, J.; Metzner, H.; Schulz, K.; Reislöhner, U.; Hahn, T.; Cieslak, J.; Witthuhn, W.; Goldhahn, R.; Hudert, F.; Kräußlich, J. *J. Appl. Phys.* **2007**, *102*, 033503.

74. Ho, C.-H.; Lo, S.-F.; Chi, P.-C. *J. Electrochem. Soc.* **2010**, *157*, H219.

75. Yakushev, M. V.; Mudryi, A. V.; Feofanov, Y.; Ivaniukovich, A. V.; Victorov, I. V. *Thin Solid Films* **2006**, *511–512*, 130.

76. Kolny-Olesiak, J.; Weller, H. *ACS Appl. Mater. Interfaces* **2013**, *5*, 12221.

77. Knowles, K. E.; Nelson, H. D.; Kilburn, T. B.; Gamelin, D. R. *J. Am. Chem. Soc.* **2015**, *137*, 13138.

78. Binsma, J. J. M.; Giling, L. J.; Bloem, J. *J. Lumin.* **1982**, *27*, 35.

79. Binsma, J. J. M.; Giling, L. J.; Bloem, J. *J. Lumin.* **1982**, *27*, 55.

80. Omata, T.; Nose, K.; Kurimoto, K.; Kita, M. *J. Mater. Chem. C* **2014**, *2*, 6867.

81. Kraatz, I. T.; Booth, M.; Whitaker, B. J.; Nix, M. G. D.; Critchley, K. *J. Phys. Chem. C* **2014**, *118*, 24102.

82. Shabaev, A.; Mehl, M. J.; Efros, A. L. *Phys. Rev. B* **2015**, *92*, 035431.

Chapter 2

Synthesis of Copper Indium Disulfide Nanoplatelets by a One-pot Method

2.1 Introduction

I-III-VI_2 semiconductor nanomaterials have attracted much attention due to their potential applications in solar-energy conversion, and are often known as “nanoinks”.[1-9] We are particularly interested in anisotropic nanocrystals, such as nanowires,[10-12] nanobelts,[13,14] or nanosheets, to minimize interfacial hopping between nanocrystals during energy and charge transport. $CuInS_2$, as an important representative for ternary I-III-VI_2 semiconductor materials, has been studied extensively recently. It has a direct bandgap of 1.53 eV and a bulk exciton Bohr radius of 4 nm.[15] Three phases, chalcopyrite,[16,17] zinc blende[18,19] and wurtzite[7,20-22] have been commonly reported for $CuInS_2$ nanocrystals at room temperature. Chalcopyrite is the cation-ordered phase among the three structures, and thermodynamically the most stable phase for bulk. In both zinc blende and wurtzite phases, Cu^+ and In^{3+} ions randomly share cation positions within a cubic-close-packed and hexagonal-close-packed S^{2-} sublattice, respectively.[7,23-25]

Although many synthetic approaches are available for $CuInS_2$, general control over morphology, crystal structure, and stoichiometry is still lacking due to inadequate understanding of the reaction kinetics. Specifically, there have been only very limited reports for 2D $CuInS_2$ nanocrystals, most of which require complicated reagents or reaction conditions.[7,8,26-29] In this chapter, we show a simple preparation of $CuInS_2$ NPs having the wurtzite crystal structure by a direct, one-pot synthetic method at relatively low temperature. The NPs display mostly hexagonal morphologies as observed from TEM images. The growth mechanism is studied by further slowing down the reaction at even lower temperature, indicating the formation of an intermediate binary phase.

2.2 Experimental Section

2.2.1 Materials and General Procedures

$In(OAc)_3$ (99.99%, metal basis), thiourea (99%), and hexadecylamine (technical grade, 90%) were obtained from Sigma-Aldrich. CuCl (97%) was obtained from Alfa Aesar. All were used as received and stored under N_2. Toluene (CHROMASOLV® for HPLC, 99.9%), and methanol (≥99.8%) were used as received from Sigma-Aldrich and stored under ambient conditions. Transmission electron microscopy (TEM) sample grids (Ni with holey carbon film) were obtained from Ted Pella, Inc. X-ray Diffraction (XRD) sample holders (zero-diffraction silicon plate, 24.6 mm diameter and 1.0 mm thickness, with cavity 10 mm diameter and 0.2 mm depth) were obtained from the MTI Corporation.

All synthetic procedures were conducted under dry N_2, except for the final purification steps, which were conducted in the ambient atmosphere.

2.2.2 Characterization Methods

Low-resolution TEM image and energy-dispersive X-ray spectroscopy (EDS) analysis data were collected using a JEOL 2000FX TEM operating at 200 kV. High-resolution TEM images were collected using a JEOL JEM-2100F field emission (FE) – scanning transmission electron microscope. Both low- and high-resolution TEM samples were prepared by dipping TEM grids into a toluene dispersion (5-6 mL) of a purified specimen, which were immediately removed to allow evaporation of the solvent. XRD patterns were collected and processed using a Bruker d8 Advance X-ray Diffractometer with Cu Kα radiation ($\lambda = 1.541845$ Å) and the Bruker Diffrac.Eva program. The XRD samples were prepared from toluene dispersions (0.5 mL) of purified specimens. Concentrated sample suspensions were drop cast onto a silicon sample holder, and dried in the fume hood. UV-visible spectra were collected using a Perkin Lambda

950 UV/Vis spectrometer. Spectral data were obtained from toluene dispersions of as-made $CuInS_2$ NPs, in quartz cuvettes.

2.2.3 Synthesis of Copper(I) Indium Sulfide Nanoplatelets ($CuInS_2$ NPs)

$CuInS_2$ NPs were synthesized using a direct, one-pot method. In a typical procedure, $In(OAc)_3$ (15 mg, 0.05 mmol), CuCl (5 mg, 0.05 mmol), thiourea (8 mg, 0.1 mmol), and hexadecylamine (3.3 g) were combined in a Schlenk tube, and heated in a 150 ℃ salt bath ($NaNO_3/KNO_3/Ca(NO_3)_2$, 21%:54%:25% by mol) for 2 h under N_2. $In(OAc)_3$, CuCl and thiourea dissolved in melting hexadecylamine rapidly after heating, with the reaction mixture turning brown. The color of reaction mixture became darker with extended reaction time, finally forming a dark brown-black suspension.

The same reaction was repeated at 95 ℃ for 4 h. Aliquots were removed during the reaction at 1 h and 2 h to study the growth process.

The as-made $CuInS_2$ NPs were dispersed in toluene for UV-visible spectroscopy.

2.2.4 Isolation of Copper(I) Indium Sulfide Nanoplatelets ($CuInS_2$ NPs)

The NPs synthesized following the method above were isolated and purified by the following procedure. The reaction mixture was allowed to cool to room temperature under N_2. $CuInS_2$ NPs were isolated by adding toluene and methanol (6 mL total, volume ratio 2:1), followed by centrifugation for 5 min at 1500 rpm and removal of the supernatant. This purification procedure was repeated twice, before the $CuInS_2$ NPs were redispersed in toluene for TEM or XRD characterization.

2.3 Results and Discussion

2.3.1 Preparation of $CuInS_2$ NPs

$CuInS_2$ NPs were prepared by a simple one-pot method in hexadecylamine using $In(OAc)_3$, CuCl and thiourea as the precursors. The reaction temperature (150 ℃) employed here was relatively low compared with most similar procedures reported for $CuInS_2$ NPs.[27-29]

TEM images of $CuInS_2$ NPs are provided in Figure 2.1. The nanocrystals exhibited hexagonal morphologies as observed previously.[7,8,27-29] Images were obtained displaying both face and edge views of the NPs. The mean NP width (point to point) and mean thickness were measured to be 33 ± 6 nm and 14 ± 2 nm, respectively.

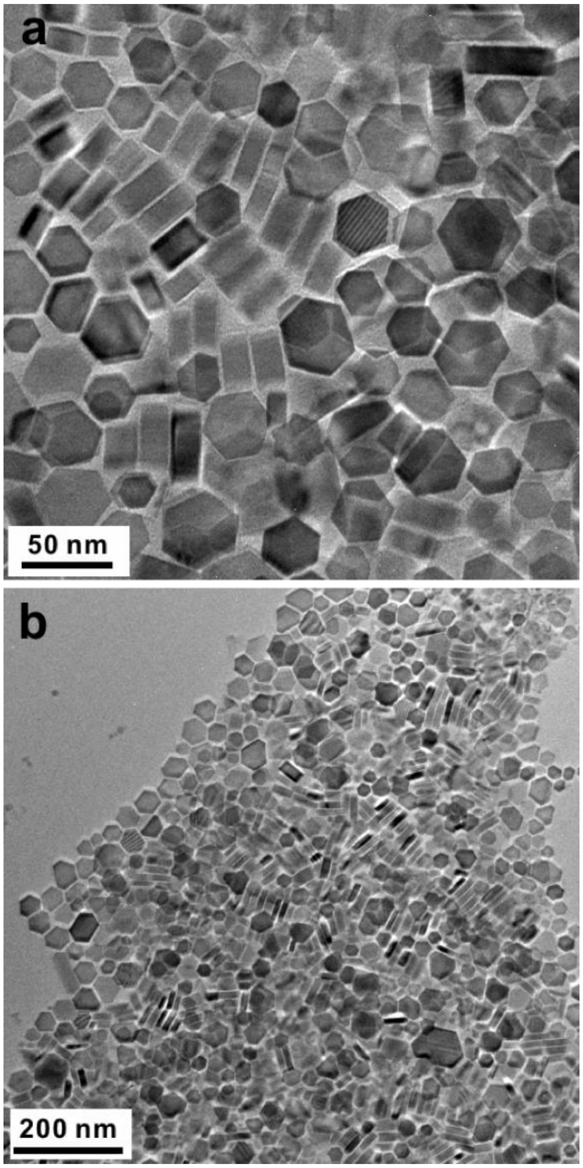

Figure 2.1. TEM images at two magnifications of $CuInS_2$ NPs prepared by the direct, one-pot method at 150 ℃.

An XRD pattern of $CuInS_2$ NPs is shown in Figure 2.2. The pattern corresponded well to the wurtzite $CuInS_2$ structure (red sticks), which has been frequently observed by other groups.[7,20-22,25] Korgel and coworkers reported synthesis of $CuInS_2$ nanodisks with wurtzite-chalcopyrite polytypism using a similar approach.[30] They noticed that intensities of the diffraction peaks in the XRD pattern did not agree exactly with those in standard wurtzite pattern, although the positions matched very well. Specifically, the intensities of the 002, 110, and 112 reflections in wurtzite were slightly higher, which could also be assigned to 112, 220, and 312 reflections in chalocopyrite, respectively. Along with further confirmation from HRTEM images, the authors attributed the intensity variance to the presence of chalcopyrite phase within the $CuInS_2$ NPs forming a wurtzite-chalcopyrite polytypism. However, in the XRD pattern shown in Figure 2.2, we found that only 002 reflection exhibited slightly higher intensity than the standard wurtzite pattern. We further noticed slight broadening of the 002 reflection, indicating that the wurtzite *z* axis was perpendicular to the NP as the thinnest dimension, as reported previously.[29,30] Thus, the higher intensity of 002 reflection could be ascribed to the preferred orientation of most NPs with the top and bottom facets aligning with the XRD substrate. Accordingly, the $CuInS_2$ NPs were assigned a pure wurtzite crystal structure.

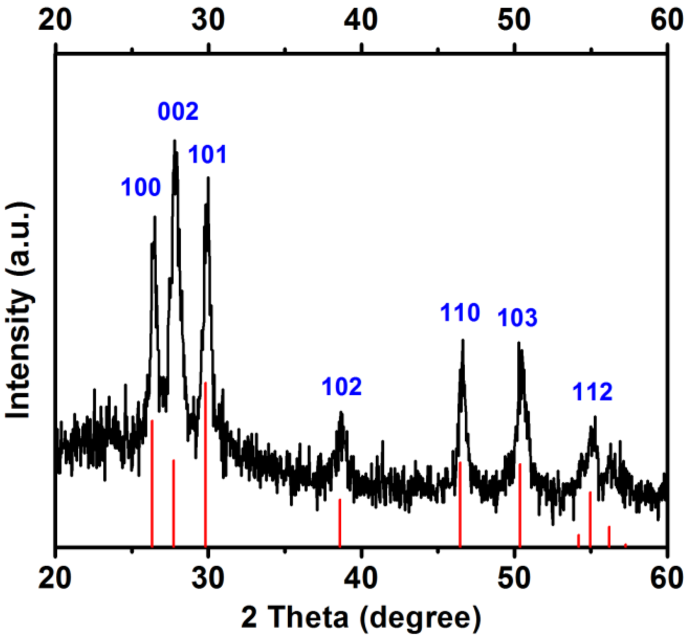

Figure 2.2. An XRD pattern of $CuInS_2$ NPs prepared by a one-pot method (black), compared to the reference pattern of wurtzite structure (ICDD-PDF 01-077-9459, red stick pattern).

The $CuInS_2$ NPs exhibited a broad exciton feature located at 746 nm (1.67 eV) in the extinction (absorption) spectrum (Figure 2.3), which was blue shifted by only 0.14 eV from the bulk bandgap (1.53 eV). The typical, nearly featureless extinction spectra of $CuInS_2$ nanocrystals have been attributed to nanocrystal size non-uniformity, morphological variations, and compositional inhomogeneities.[31-33] Furthermore, the mean thickness of these NPs (14 nm) was more than twice the bulk exciton Bohr radius in $CuInS_2$ of 4 nm,[15] resulting in only weak quantum-confinement effects in these NPs.

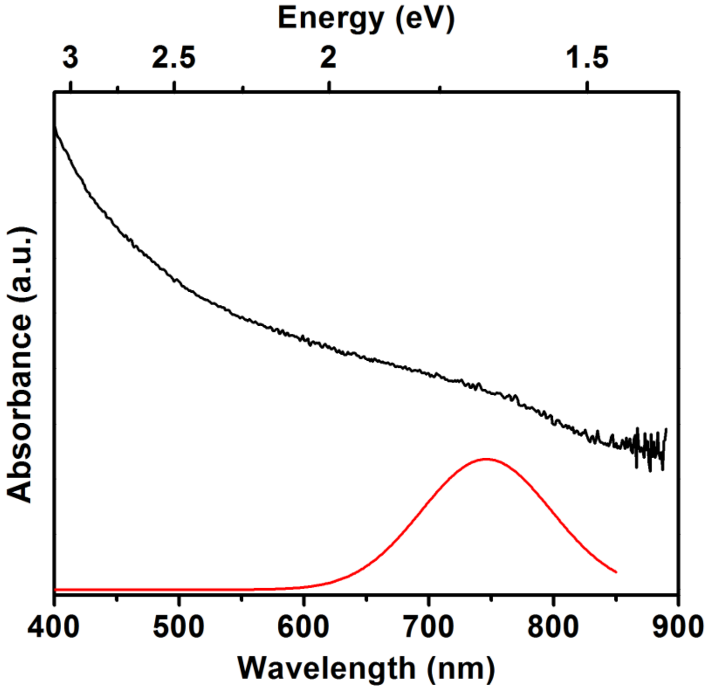

Figure 2.3. An extinction (absorption) spectrum of $CuInS_2$ NPs (black) prepared by a one-pot method, with a feature at 746 nm fit with Gaussian (intensity increased by 10 times, red).

2.3.2 Growth pathway of $CuInS_2$ NPs

The reaction was slowed down by lowering the reaction temperature to 95 °C, allowing observation of the intermediate stages during the process. Figure 2.4a, b, and c are TEM images obtained from reaction mixtures after 1 h, 2 h, and 4 h of reaction time, respectively. We found that the particle size increased as the reaction progressed, changing from near spherical (a) to hexagonal (c) morphology. The thickness of $CuInS_2$ was estimated to be 14 nm, which is similar as that of products from higher reaction temperature. EDS analysis showed that the In/Cu ratio also increased during the reaction. The mean molar percentages in the product NPs were 43.85% Cu, 10.65% In, and 45.50% S at 1 h; 28.39% Cu, 19.75% In, and 51.86% S at 2 h, and reaching near stoichiometry, 22.95% Cu, 22.37% In, and 54.68% S at 4 h (Table 2.1). The trend of the composition change indicated that Cu^+ and In^{3+} may not react with S^{2-} simultaneously. Instead, Cu^+ reacted with S^{2-} first, forming an intermediate which was likely Cu_2S. In^{3+} then incorporated into Cu_2S and exchanged with Cu^+ to produce the $CuInS_2$ nanoplatelets.

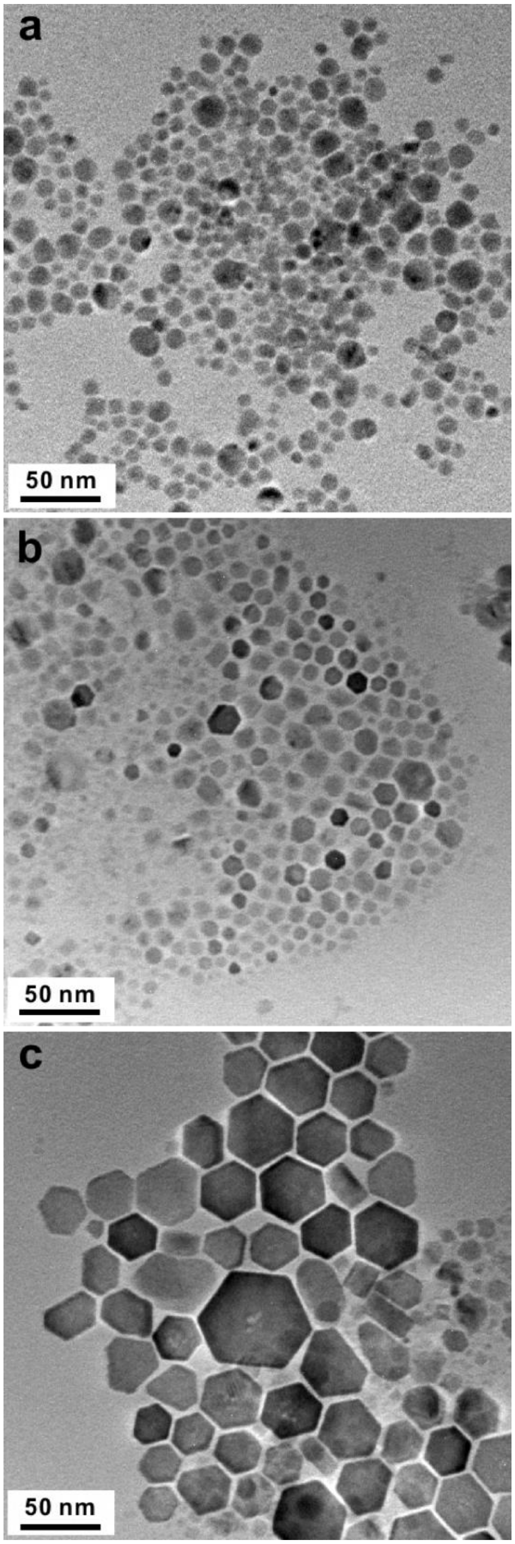

Figure 2.4. TEM images of $CuInS_2$ nanocrystals prepared at 95 ℃ at different reaction stages, with reaction time of (a) 1 h, (b) 2 h, and (c) 4 h.

Table 2.1. Composition of $CuInS_2$ nanocrystals prepared at 95 ℃ at different reaction stages determined by EDS.[a]

Length of reaction time	Cu : In : S molar ratio	
	At different spots	**Mean**
1 h	39.65% : 13.78% : 46.57% 44.27% : 11.00% : 44.73% 47.62% : 7.19% : 45.19%	43.85% : 10.65% : 45.50%
2 h	25.82% : 20.41% : 53.77% 29.51% : 20.69% : 49.80% 29.84% : 18.14% : 52.02%	28.39% : 19.75% In : 51.86%
4 h	24.44% : 21.16% : 54.40% 21.46%: 23.58% : 54.96%	22.95% : 22.37% : 54.68%

[a] The spot size for the EDS analyses is sufficiently large to include many nanocrystals. Thus the measurements at different spots within each specimen include different collections of many nanocrystals.

A similar pathway has been proposed in previous studies.[34-37] Cui and coworkers divided the reaction process into three steps: formation of Cu_2S nanocrystals, growth of $CuInS_2$ phase initiated from one spot of Cu_2S through In^{3+} insertion, and complete conversion to $CuInS_2$ nanocrystals.[34] This pathway was made possible by the closely related crystal structures between the hexagonal Cu_2S and wurtzite $CuInS_2$ phases, and the high mobility of Cu^+ in Cu_2S.[34]

From TEM images in Figures 2.1 and 2.4, we did not observe significant thickness change with either reaction temperature or length of reaction time. The mechanism of selective facet growth is not clear yet. Although the experiments conducted here are limited and do not represent all possible reaction conditions, it is well known that with limited understanding of and control over reaction kinetics, the size and morphology control of $CuInS_2$ nanocrystals synthesized by the direct methods is complicated by unbalanced reactivities of the different precursors.[38,39] In order to tune the morphology and thickness of the $CuInS_2$ NPs and to study the optical properties with better resolved exciton feature than that in Figure 2.3, we need to either understand the morphology-control mechanism or develop a more straightforward synthetic strategy. Given our observations from the experiments and mechanism proposed,[34] a reasonable alternative approach is the initial preparation of binary Cu_2S nanocrystals as the template followed by purposeful ion exchange to afford the $CuInS_2$ composition. If the ion exchange occurs in a topographic way, morphology tunability of multinary nanocrystals is enhanced via a binary precursor phase. We discuss this method in the next two chapters.

2.4 Conclusions

Hexagonal $CuInS_2$ NPs having the wurtzite structure are prepared using a low-temperature, one-pot synthetic method. But it remains challenging to tune the morphology and size of the nanocrystals, due to the lack of general control over the ternary system. Monitoring the reaction process by EDS at an even lower temperature implies that Cu_2S is likely formed as a binary intermediate, followed by an insertion of In^{3+} ions to afford $CuInS_2$ composition. This possible pathway suggests an ion-exchange synthetic approach through binary, template nanocrystals for multinary nanocrystals like $CuInS_2$.

2.5 References

1. Wooten, A. J.; Werder, D. J.; Williams, D. J.; Casson, J. L.; Hollingsworth, J. A. *J. Am. Chem. Soc.* **2009**, *131*, 16177.

2. Xu, J.; Lee, C.-S.; Tang, Y.-B.; Chen, X.; Chen, Z.-H.; Zhang, W.-J.; Lee, S.-T.; Zhang, W.; Yang, Z. *ACS Nano* **2010**, *4*, 1845.

3. Li, Q.; Zou, C.; Zhai, L.; Zhang, L.; Yang, Y.; Chen, X.; Huang, S. *CrystEngComm* **2013**, *15*, 1806.

4. Choi, Y.; Beak, M.; Yong, K. *Nanoscale* **2014**, *6*, 8914.

5. Wu, X.-J.; Huang, X.; Qi, X.; Li, H.; Li, B.; Zhang, H. *Angew. Chem., Int. Ed.* **2014**, *53*, 8929.

6. Li, Q.; Zhai, L.; Zou, C.; Huang, X.; Zhang, L.; Yang, Y.; Chen, X.; Huang, S. *Nanoscale* **2013**, *5*, 1638.

7. Qi, Y.; Liu, Q.; Tang, K.; Liang, Z.; Ren, Z.; Liu, X. *J. Phys. Chem. C* **2009**, *113*, 3939.

8. Sheng, X.; Wang, L.; Luo, Y.; Yang, D. *Nanoscale Res. Lett.* **2011**, *6*, 562.

9. Panthani, M. G.; Akhavan, V.; Goodfellow, B.; Schmidtke, J. P.; Dunn, L.; Dodabalapur, A.; Barbara, P. F.; Korgel, B. A. *J. Am. Chem. Soc.* **2008**, *130*, 16770.

10. Glennon, J. J.; Tang, R.; Buhro, W. E.; Loomis, R. A. *Nano Lett.* **2007**, *7*, 3290.

11. Wayman, V. L.; Morrison, P. J.; Wang, F.; Tang, R.; Buhro, W. E.; Loomis, R. A. *J. Phys. Chem. Lett.* **2012**, *3*, 2627.

12. Liu, Y.-H.; Wang, F.; Hoy, J.; Wayman, V. L.; Steinberg, L. K.; Loomis, R. A.; Buhro, W. E. *J. Am. Chem. Soc.* **2012**, *134*, 18797.

13. Liu, Y.-H.; Wayman, V. L.; Gibbons, P. C.; Loomis, R. A.; Buhro, W. E. *Nano Lett.* **2010**, *10*, 352.

14. Liu, Y.-H.; Wang, F.; Wang, Y.; Gibbons, P. C.; Buhro, W. E. *J. Am. Chem. Soc.* **2011**, *133*, 17005.

15. Czekelius, C.; Hilgendorff, M.; Spanhel, L.; Bedja, I.; Lerch, M.; Müller, G.; Bloeck, U.; Su, D.-S.; Giersig, M. *Adv. Mater.* **1999**, *11*, 643.

16. Li, L.; Pandey, A.; Werder, D. J.; Khanal, B. P.; Pietryga, J. M.; Klimov, V. I. *J. Am. Chem. Soc.* **2011**, *133*, 1176.

17. Chen, B.; Zhong, H.; Zhang, W.; Tan, Z. a.; Li, Y.; Yu, C.; Zhai, T.; Bando, Y.; Yang, S.; Zou, B. *Adv. Funct. Mater.* **2012**, *22*, 2081.

18. Nose, K.; Soma, Y.; Omata, T.; Otsuka-Yao-Matsuo, S. *Chem. Mater.* **2009**, *21*, 2607.

19. Yue, W.; Han, S.; Peng, R.; Shen, W.; Geng, H.; Wu, F.; Tao, S.; Wang, M. *J. Mater. Chem.* **2010**, *20*, 7570.

20. Lu, X.; Zhuang, Z.; Peng, Q.; Li, Y. *CrystEngComm* **2011**, *13*, 4039.

21. van der Stam, W.; Berends, A. C.; Rabouw, F. T.; Willhammar, T.; Ke, X.; Meeldijk, J. D.; Bals, S.; de Mello Donega, C. *Chem. Mater.* **2015**, *27*, 621.

22. Akkerman, Q. A.; Genovese, A.; George, C.; Prato, M.; Moreels, I.; Casu, A.; Marras, S.; Curcio, A.; Scarpellini, A.; Pellegrino, T.; Manna, L.; Lesnyak, V. *ACS Nano* **2015**, *9*, 521.

23. Binsma, J. J. M.; Giling, L. J.; Bloem, J. *J. Cryst. Growth* **1980**, *50*, 429.

24. Binsma, J. J. M.; Giling, L. J.; Bloem, J. *Phys. Status Solidi A* **1981**, *63*, 595.

25. Pan, D.; An, L.; Sun, Z.; Hou, W.; Yang, Y.; Yang, Z.; Lu, Y. *J. Am. Chem. Soc.* **2008**, *130*, 5620.

26. Batabyal, S. K.; Tian, L.; Venkatram, N.; Ji, W.; Vittal, J. J. *J. Phys. Chem. C* **2009**, *113*, 15037.

27. Kruszynska, M.; Borchert, H.; Parisi, J.; Kolny-Olesiak, J. *J. Am. Chem. Soc.* **2010**, *132*, 15976.

28. Abdelhady, A. L.; Malik, M. A.; O'Brien, P. *J. Mater. Chem.* **2012**, *22*, 3781.

29. Chang, J.; Waclawik, E. R. *CrystEngComm* **2013**, *15*, 5612.

30. Koo, B.; Patel, R. N.; Korgel, B. A. *Chem. Mater.* **2009**, *21*, 1962.

31. Xie, R.; Rutherford, M.; Peng, X. *J. Am. Chem. Soc.* **2009**, *131*, 5691.

32. van der Stam, W.; Berends, A. C.; de Mello Donega, C. *ChemPhysChem* **2016**, *17*, 559.

33. So, D.; Konstantatos, G. *Chem. Mater.* **2015**, *27*, 8424.

34. Connor, S. T.; Hsu, C.-M.; Weil, B. D.; Aloni, S.; Cui, Y. *J. Am. Chem. Soc.* **2009**, *131*, 4962.

35. Ahmadi, M.; Pramana, S. S.; Xi, L.; Boothroyd, C.; Lam, Y. M.; Mhaisalkar, S. *J. Phys. Chem. C* **2012**, *116*, 8202.

36. Tan, J. M. R.; Lee, Y. H.; Pedireddy, S.; Baikie, T.; Ling, X. Y.; Wong, L. H. *J. Am. Chem. Soc.* **2014**, *136*, 6684.

37. Collord, A. D.; Hillhouse, H. W. *Chem. Mater.* **2015**, *27*, 1855.

38. Beberwyck, B. J.; Surendranath, Y.; Alivisatos, A. P. *J. Phys. Chem. C* **2013**, *117*, 19759.

39. De Trizio, L.; Manna, L. *Chem. Rev.* **2016**.

Chapter 3

Influence of the Nanoscale Kirkendall Effect on the Morphology of Copper Indium Disulfide Nanoplatelets Synthesized by Ion Exchange*

*****Reprinted with permission from Mu, L.; Wang, F.; Sadtler, B.; Loomis, R. A.; Buhro, W. E. *ACS Nano* **2015**, *9*, 7419. Copyright 2015 American Chemical Society.

3.1 Introduction

In this chapter, the synthesis of $CuInS_2$ nanoplatelets (NPs) using an ion-exchange method and the reaction mechanism are reported. The morphologies of $CuInS_2$ nanocrystals prepared by ion exchange with $Cu_{2-x}S$ NPs depend markedly on the indium precursor employed and the reaction temperature. More-ionic InX_3 precursors and/or higher exchange temperatures produce single-crystalline $CuInS_2$ NPs with preservation of the sizes and morphologies of the starting $Cu_{2-x}S$ NPs. More-covalent InX_3 precursors and/or lower exchange temperatures afford hollow-centered, ring-like nanocrystals as a result of the nanoscale Kirkendall Effect. The varying morphologies are attributed to the reaction barriers for In^{3+} insertion at the thin edges of the $Cu_{2-x}S$ NPs.

We are interested in pseudo-1D[1-3] and pseudo-2D[4,5] nanocrystals for their potential to transport energy and charge with mininal interfacial hopping between nanocrystals.[6] Considerable interest has focused on $CuInS_2$ and related I-III-VI_2 nanostructures for applications in solar-energy conversion,[7-14] which attracted our attention to anisotropic nanocrystals of $CuInS_2$ and $CuInSe_2$.

The direct, solution-based syntheses of ternary and quaternary nanocrystals are complicated by the typically varying reactivities of the multiple precursors required.[15-18] In many cases, binary nanocrystals are first formed, which convert to the multinary target nanocrystals upon subsequent reaction, including by ion exchange.[18-21] Thus, a logical approach to the synthesis of anisotropic $CuInS_2$ and related nanocrystals is the initial preparation of binary nanocrystals to serve as the anisotropic template, followed by purposeful ion exchange to afford the desired ternary or multinary composition.[8]

Cu_2S and $Cu_{2-x}S$ readily undergo cation-exchange reactions.[22,23] Indeed, Donega and coworkers recently prepared $CuInS_2$ nanocrystals by partial indium-cation exchange into small $Cu_{2-x}S$ dot-like nanocrystals according to eq 3.1.[23] Lesnyak and coworkers reported similar observations at about the same time.[24] In these cases cation exchange was aided by the small sizes and therefore short ion-diffusion distances within the pseudo-spherical nanocrystals. Lesnyak and coworkers also reported a related partial zinc and tin cation-exchange process with anisotropic $Cu_{2-x}S_ySe_{1-y}$ NPs.[25] However, the NP dimensions in that study were comparatively small (mean width = 18 nm; mean thickness = 4 nm). We show here that cation exchange into anisotropic template nanocrystals having longer diffusion distances is more complex. We determine how the eq-3.1 exchange process may be conducted using larger $Cu_{2-x}S$ NPs, with preservation of the initial platelet morphology.

$$2Cu_2S + In^{3+} \longrightarrow CuInS_2 + 3Cu^{+} \quad (3.1)$$

We now report that the $CuInS_2$ nanocrystal morphologies obtained by cation exchange using $Cu_{2-x}S$ NPs having a mean width of 46 nm and a mean thickness of 13 nm depend on the In^{3+} source and the exchange temperature. Exchange reactions conducted with $InCl_3$ at 150 ℃ produce single-crystal hollow-centered nanoparticles, whereas those conducted with $InCl_3$ at 200 ℃ produce single-crystal NPs having the same mean dimensions as the initial template nanocrystals. Exchange reactions conducted with InI_3 at 150 ℃ produce nanorings with even larger center openings, whereas those conducted with $In(OAc)_3$ or $In(acac)_3$ at 150 ℃ produce NPs retaining the initial morphology. A mechanistic model is proposed to account for these experimental findings.

3.2 Experimental Section

3.2.1 Materials and General Procedures

n-Dodecylamine (98%), tri-*n*-octylphosphine (TOP) (97%), In(OAc)$_3$ (99.99%, metal basis), In(acac)$_3$ (99.99%+) were obtained from Sigma-Aldrich. InCl$_3$ (anhydrous, 99.999%-In), InI$_3$ (99.999%-In) were obtained from Strem Chemicals. All were used as received and stored under N$_2$. Toluene (CHROMASOLV® for HPLC, 99.9%) from Sigma-Aldrich, methanol (≥99.8%) from Sigma-Aldrich, carbon tetrachloride (CHROMASOLV® for HPLC, ≥99.9%), *n*-dodecanethiol (98%) from Sigma-Aldrich, $Cu(NO_3)_2$ 3H_2O (99.5%) from Strem Chemicals, and ethyl alcohol (100%) from Pharmco-Aaper were used as received and stored under ambient conditions. Copper(I) dodecanethiolate ($CuSC_{12}H_{25}$) was prepared by a literature method[26] and stored under dry N$_2$. Transmission electron microscopy (TEM) sample grids (Ni with holey carbon film) were obtained from Ted Pella, Inc. X-ray Diffraction (XRD) sample holders (zero-diffraction silicon plate, 24.6 mm diameter and 1.0 mm thickness, with cavity 10 mm diameter and 0.2 mm depth) were obtained from the MTI Corporation.

All synthetic procedures were conducted under dry N$_2$, except for the final purification steps, which were conducted in the ambient atmosphere.

3.2.2 Characterization Methods

Low-resolution TEM images and energy-dispersive X-ray spectroscopy (EDS) analysis data were collected using a JEOL 2000FX TEM operating at 200 kV. High-resolution TEM (HRTEM) images were collected using a JEOL JEM-2100F field emission (FE) – scanning transmission electron microscope. Both low- and high-resolution TEM samples were prepared by dipping TEM grids into a toluene dispersion (5-6 mL) of a purified specimen, which were immediately removed to allow evaporation of the solvent. XRD patterns were collected and processed using a Bruker d8 Advance X-ray Diffractometer with Cu Kα radiation ($\lambda = 1.541845$ Å) and the Bruker Diffrac.Eva program. The XRD samples were prepared from toluene dispersions (0.5 mL) of purified specimens. The concentrated suspension was drop casted onto a silicon sample holder, and dried in the fume hood. UV-visible, near-infrared spectra were collected using a Perkin Lambda 950 UV/Vis spectrometer. Spectral data were obtained from CCl_4 dispersions of purified $Cu_{2-x}S$ nanoplatelets, and toluene dispersions of as-made $CuInS_2$ nanocrystals, in quartz cuvettes.

3.2.3 Synthesis of Copper(I) Sulfide Nanoplatelets ($Cu_{2-x}S$ NPs)

$Cu_{2-x}S$ NPs were synthesized by adapting a literature method.[26] In a typical procedure, $CuSC_{12}H_{25}$ (0.026 g, 0.10 mmol) and *n*-dodecylamine (0.370 g, 2.00 mmol) were combined in a Schlenk tube, and heated in a 200 °C salt bath ($NaNO_3/KNO_3/Ca(NO_3)_2$, 21%:54%:25% by mol) for 8 h. The $CuSC_{12}H_{25}$ dissolved in melting *n*-dodecylamine rapidly upon heating, forming a light yellow solution. The reaction mixture turned brown within 20 min, and darker with extended reaction time, finally forming a dark brown-black suspension after 8 h.

The mixture was allowed to cool to room temperature under N_2. The as-made product mixture was used for cation exchange. For characterization, $Cu_{2-x}S$ NPs were isolated by adding toluene and methanol (6 mL total, volume ratio 2:1), followed by centrifuging for 5 min at 1500 rpm and discarding the supernatant. This purification procedure was repeated twice, before the $Cu_{2-x}S$ NPs were redispersed in toluene for TEM and XRD characterization, and in CCl_4 for UV-visible/near-IR spectroscopy.

3.2.4 Synthesis of Copper(I) Indium Sulfide Nanoplatelets ($CuInS_2$ NPs) by Cation Exchange

In a typical procedure, $InCl_3$ (0.006 g, 0.03 mmol) was added to TOP (2 g), which dissolved after sonication for 10 min at room temperature. The as-made $Cu_{2-x}S$ NPs product mixture in a Schlenk tube was heated in salt bath (at 150, 180, or 200 ℃) forming a black suspension, and into which the $InCl_3$ solution was swiftly injected *via* syringe. The Schlenk tube was held at a constant temperature (150, 180, or 200 ℃) for 2 h, and aliquots were removed for analysis during the reaction.

$CuInS_2$ NPs were isolated by adding toluene and methanol (6 mL total, volume ratio 2:1), followed by centrifuging for 5 min at 1500 rpm and discarding the supernatant. This purification procedure was repeated twice, and then the $CuInS_2$ NPs were redispersed in toluene for TEM and XRD characterization. The as-made $CuInS_2$ NPs was dispersed in toluene for UV-Visible spectroscopy.

The same general procedure was employed with InI_3, $In(OAc)_3$ or $In(acac)_3$ as the indium precursor, except for the initial dissolution step. The precursor InI_3 (0.013 g, 0.03 mmol) was dissolved in TOP after sonication for 5 min at room temperature. The precursor $In(OAc)_3$ (0.008 g, 0.03 mmol) was dispersed in TOP after sonication for 30 min at room temperature; in some procedures *n*-dodecylamine (0.051 g, 0.3 mmol) was added, and the mixture warmed to 150 ℃ (10 min) to aid in dissolution. The precursor $In(acac)_3$ (0.011 g, 0.03 mmol) was dispersed in TOP after sonication for 20 min at room temperature, and the mixture was warmed to 150 ℃ (10 min) to aid in dissolution.

3.3 Results

3.3.1 Preparation of $Cu_{2-x}S$ Template NPs

The starting $Cu_{2-x}S$ NPs were prepared by thermolysis of copper(I) dodecanethiolate ($CuSC_{12}H_{25}$) according to a procedure initially reported by Korgel and coworkers,[27,28] and later adapted by Tao and coworkers,[26,29,30] and Wu and coworkers.[31] We found that the thermolysis process was conveniently accelerated in the presence of *n*-dodecylamine, and so employed *n*-dodecylamine as an additive.

TEM images of the $Cu_{2-x}S$ NPs are provided in Figure 3.1. The nanocrystals exhibited the pseudo-hexagonal habit observed in the prior studies.[26-31] Statistical analysis of the images gave a mean NP (point-to-point) width of 46 ± 10 nm and a mean thickness of 13 ± 1 nm (Figure 3.2). The clean NP images and the platelet-wide Moiré fringes observed for some overlapping NPs suggested them to be single crystalline, as previously reported.[28] The $Cu_{2-x}S$ NPs exhibited the expected, broad localized surface plasmon resonance, centered near 1970 nm, in a visible-near-IR extinction (absorption) spectrum (Figure 3.3).[26,30]

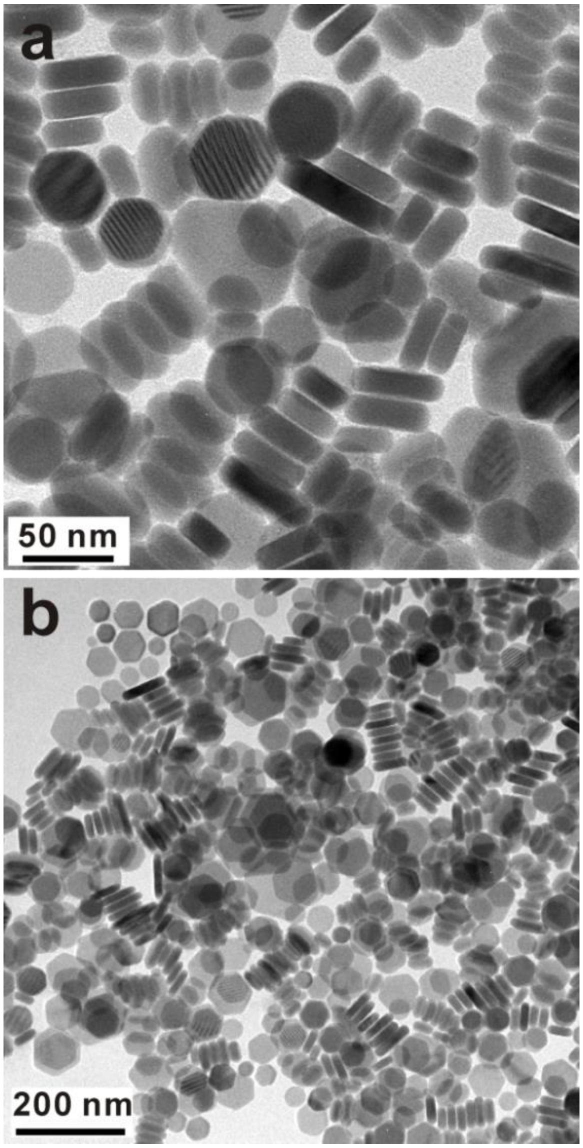

Figure 3.1. TEM images at two magnifications of the template $Cu_{2-x}S$ NPs prepared by adaptation of literature methods.[26]

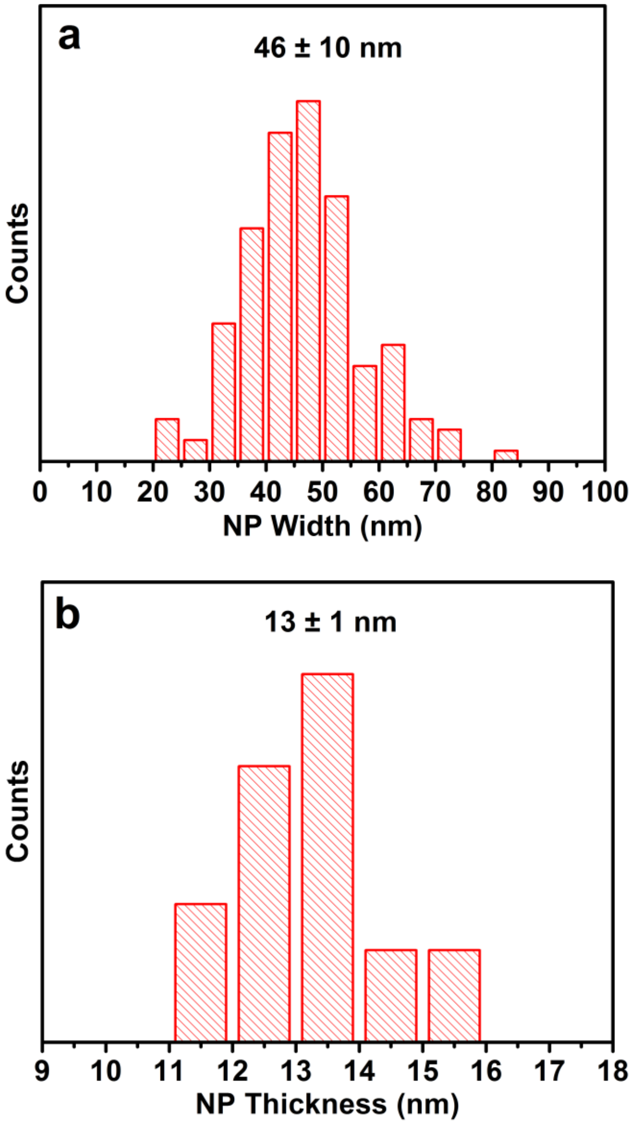

Figure 3.2. Size distributions of $Cu_{2-x}S$ NPs. (a) NP width distribution. (b) NP thickness distribution. The distributions yielded the mean size ± one standard deviation for each.

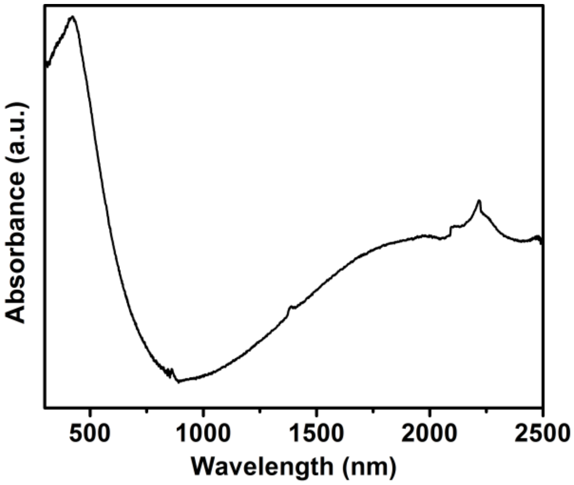

Figure 3.3. A visible-near-IR extinction (absorption) spectrum of the $Cu_{2-x}S$ NPs.

XRD pattern of the $Cu_{2-x}S$ NPs is given in Figure 3.4. The Cu_2S-related phases exhibit structural polymorphism, with hexagonal high chalcocite (Cu_2S), monoclinic low chalcocite (Cu_2S), and monoclinic djurleite ($Cu_{2-x}S$, $x \approx 0.03$-0.07)[32] being among the most commonly observed polymorphs.[32] The pattern in Figure 3.4 corresponds most closely to djurleite, and clearly indicates a phase of lower symmetry than hexagonal high chalcocite. There is apparent disagreement in the literature concerning the structures of $Cu_{2-x}S$ NPs made by variations of the method employed here.[26-31] However, the structural differences between the phases are fairly small,[33] and both djurleite and low chalcocite transform to high chalcocite above about 105 °C.[34] As the substitution reactions described here were conducted at temperatures above 105 °C, the structure of the $Cu_{2-x}S$ NPs under reaction conditions was presumed to be hexagonal high chalcocite.

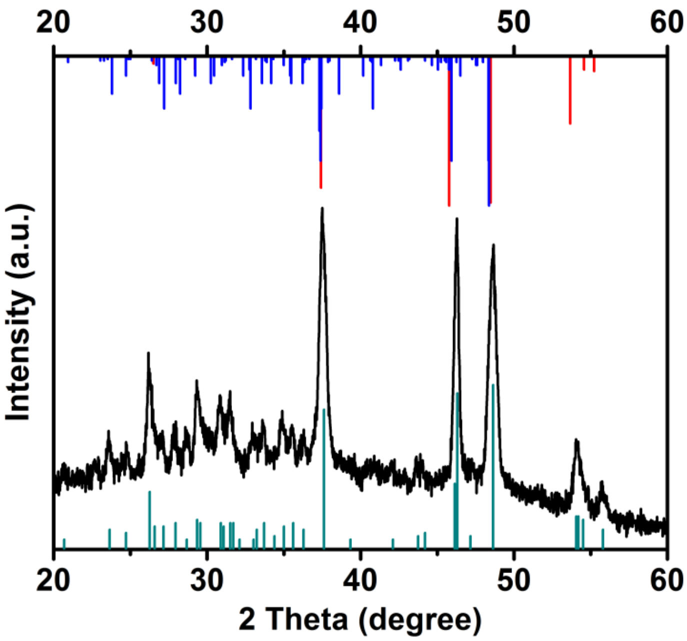

Figure 3.4. An XRD pattern of the $Cu_{2-x}S$ NPs (black), compared to the reference patterns of djurleite ($Cu_{2-x}S$, ICDD-PDF 00-023-0959, cyan), low chalcocite (Cu_2S, ICDD-PDF 00-033-0490, blue), and high chalcocite (Cu_2S, ICDD-PDF 00-026-1116, red).

3.3.2 Cation-Exchange Reactions Affording $CuInS_2$ Nanocrystals

An as-prepared *n*-dodecylamine dispersion of $Cu_{2-x}S$ NPs was heated to 150 ℃, and a tri-*n*-octylphosphine (TOP) solution of $InCl_3$ (in the stoichiometric amount to prepare $CuInS_2$) was added. TOP was employed as the reaction solvent, in accord with Alivisatos and coworkers,[22] for its soft basicity and ability to complex the soft acid Cu^+. Reaction monitoring by XRD established that the ion-exchange process affording $CuInS_2$ was complete within 2 min. The XRD pattern of the resulting nanocrystals corresponded to $CuInS_2$ in the wurtzite structure (Figure 3.5). Thus, the hexagonal-close-packed anion sublattice of high chalcocite was retained, and the Cu and In ions adopted random positions within the cation sublattice, as is frequently observed in $CuInS_2$ nanocrystals.[13,23,24,35,36]

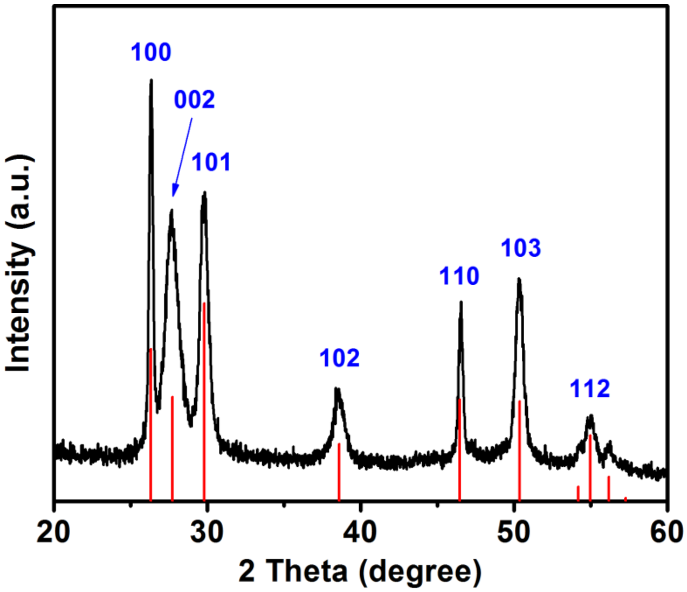

Figure 3.5. An XRD pattern of $CuInS_2$ nanocrystals resulting from ion exchange between $Cu_{2-x}S$ NPs and $InCl_3$ (150 ℃, 2 min), compared to the reference pattern of $CuInS_2$ in the wurtzite structure (ICDD-PDF 01-077-9459). The crystalline coherence lengths in the lateral and thickness dimensions from the Scherrer equation were found to be 28 and 8.2 nm, respectively, using the 100, 002, and 110 reflections (see Table 3.1).

Table 3.1. The crystalline coherence lengths of $CuInS_2$ nanocrystals in the lateral and thickness dimensions from the Scherrer equation.[a]

InX_3, ion exchange temperature	**Coherence length (nm)**		
	[100][a]	[110][a]	[002][a]
$InCl_3$, 150 ℃	28.1	27.9	8.2
$In(OAc)_3$, 150 ℃	31.4	27.0	11.4

[a] The [100] and [110] directions lie in the nanoplatelet plane, whereas the [002] direction is perpendicular to the nanoplatelet plane. Thus the [100] and [110] coherence lengths are in the nanoplatelet width dimension, whereas the [002] coherence length is in the thickness dimension.

TEM images of these nanocrystals revealed that the NP morphology of the starting $Cu_{2-x}S$ nanocrystals was largely retained; however, most of them contained variously shaped holes through the large facets and near the platelet centers, sometimes with thinning or additional perforations elsewhere within the interiors of the nanocrystals (Figure 3.6). Edge views of the nanocrystals showed them to have irregularities in the thickness dimension, consistent with partial erosion of the initially dense $Cu_{2-x}S$ NPs. Analysis of mean NP composition by energy-dispersive x-ray spectroscopy (EDS) in the TEM gave the molar percentages 24.3% Cu, 24.1% In, and 51.6% S, close to the ideal phase composition (EDS data for all product specimens are listed in Table 3.2).

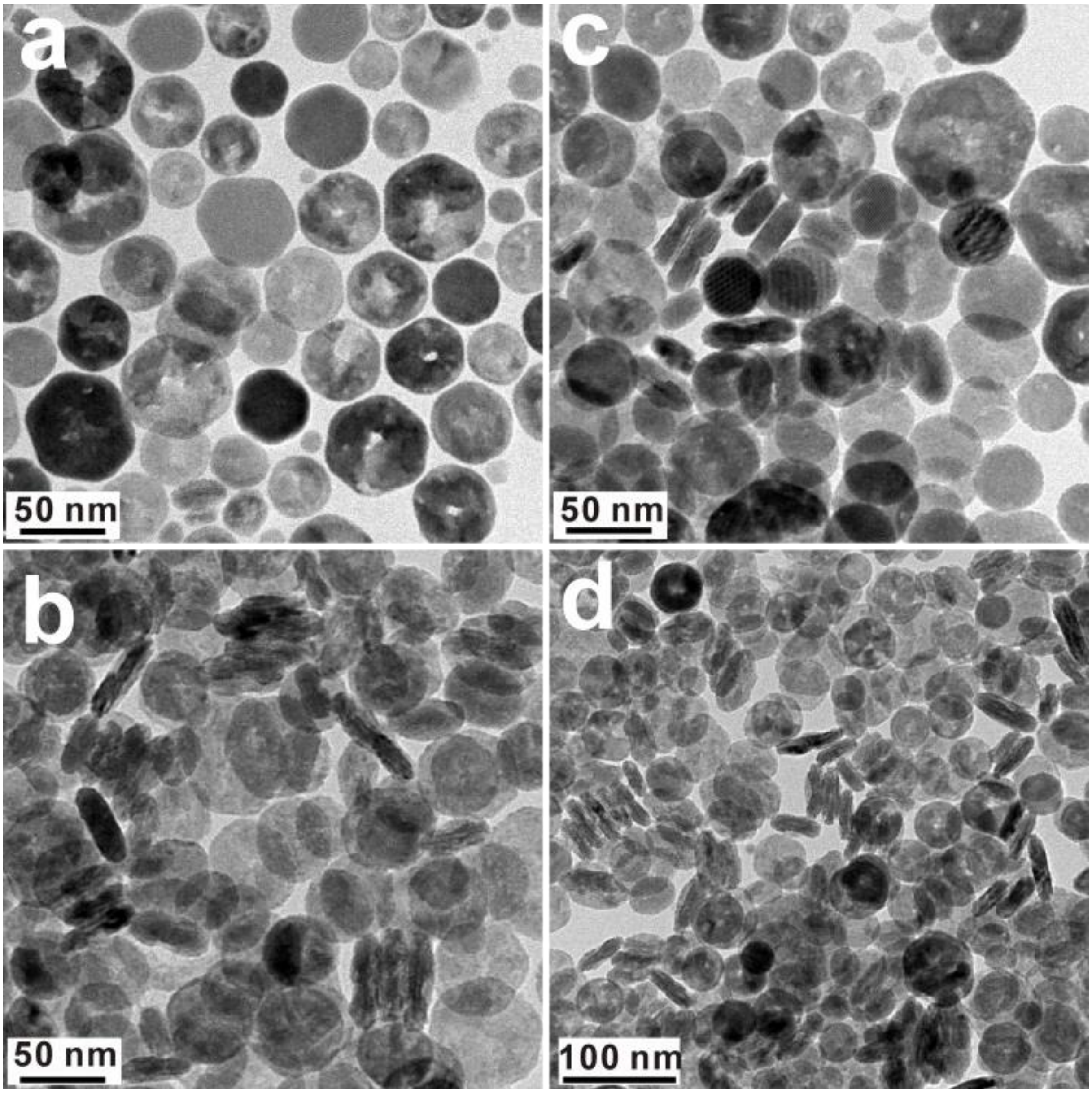

Figure 3.6. TEM images of $CuInS_2$ nanocrystals resulting from ion exchange between $Cu_{2-x}S$ NPs and $InCl_3$ (150 ℃), revealing central holes and other thickness variations. All images were collected from the same synthetic sample.

Table 3.2. Composition of $CuInS_2$ nanocrystals in final products after complete ion exchange under different reaction conditions determined by EDS.[a]

InX_3, ion exchange temperature	**Cu : In : S molar ratio**	
	At different spots	**Mean**
$InCl_3$, 150 ℃	23.82% : 25.04% : 51.14% 25.38% : 22.90% : 51.72% 23.61% : 24.49% : 51.90%	24.27% : 24.14% : 51.59%
$InCl_3$, 200 ℃	23.51% : 24.49% : 52.00% 22.56% : 25.71% : 51.73% 26.38% : 22.69% : 50.93%	24.15% : 24.30% : 51.55%
InI_3, 150 ℃	29.33% : 29.13% : 41.54% 26.04% : 29.40% : 44.56% 28.86% : 28.45% : 42.69%	28.08% : 28.99% : 42.93%
$In(OAc)_3$, 150 ℃	23.80% : 25.74% : 50.46% 25.20% : 21.59% : 53.21% 24.81% : 24.04% : 51.15%	24.60% : 23.79% : 51.61%
$In(acac)_3$, 150 ℃	24.04% : 27.01% : 48.95% 21.73% : 25.31% : 52.96%	22.88% : 26.16% : 50.96%

[a] The spot size for the EDS analyses is sufficiently large to include many nanocrystals. Thus the measurements at different spots within each specimen include different collections of many nanocrystals.

Figure 3.7a is a HRTEM image of a $CuInS_2$ nanocrystal in which the center was substantially eroded during the exchange process, leaving an irregular, ring morphology. The fast Fourier transform (FFT) of this image (Figure 3.7b) exhibited nearly clean hexagonal symmetry, indicating the single-crystal character of the nanoring, and consistent with its wurtzite structure in the [001] orientation. The $CuInS_2$ nanocrystal on the right of Figure 3.7c is more typical of the results at the 150 ℃ reaction temperature. An irregular hole slightly off center was apparent, and other thickness variations were evident. Even so, the FFT was consistent with a single crystal (Figure 3.7d). The results suggested that the $CuInS_2$ nanoring derived from a precursor single-crystal $Cu_{2-x}S$ NP, which, in the course of cation exchange, underwent a process that removed material from near the center of the NP.

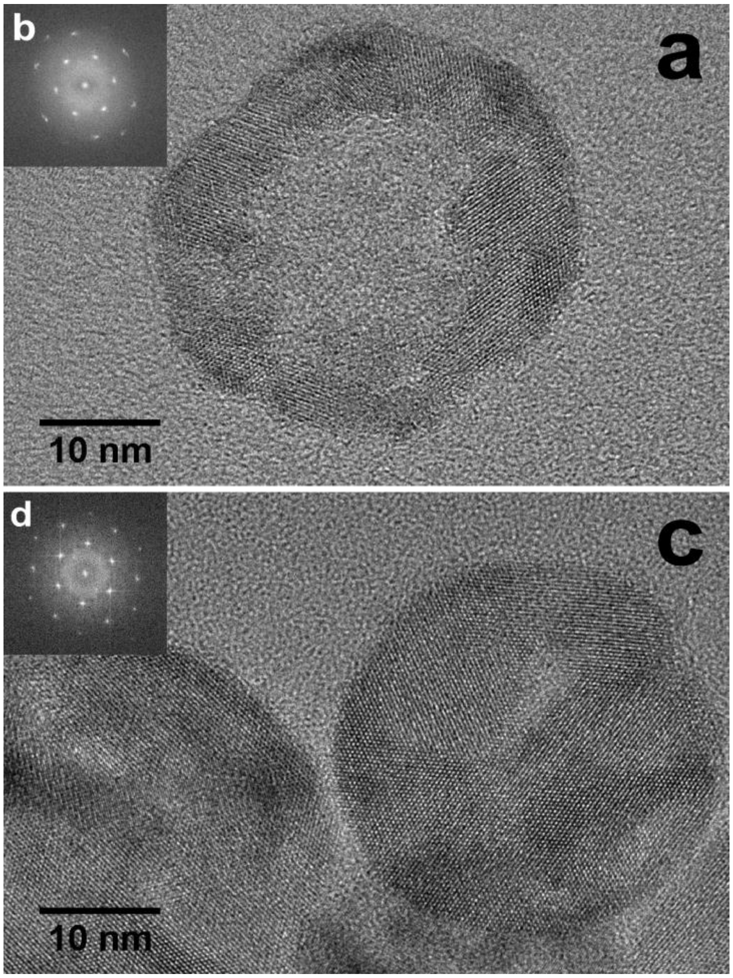

Figure 3.7. HRTEM images of $CuInS_2$ nanocrystals resulting from ion exchange between $Cu_{2-x}S$ NPs and $InCl_3$ (150 ℃). The fast Fourier transforms in b and d correspond to the images in a and c (viewed in the wurtzite (001) zone axis), respectively.

The cation-exchange experiment was repeated with $Cu_{2-x}S$ NPs and $InCl_3$ as described above, except at a higher temperature of 180 ℃. The product nanocrystals consisted of a high proportion of intact, fully dense $CuInS_2$ NPs, with the fewer eroded nanocrystals having comparatively smaller central holes (Figure 3.8). The TEM images in Figure 3.9 show the $CuInS_2$ nanocrystal morphologies from a cation-exchange experiment conducted at 200 ℃. In this case the product consisted almost entirely of intact $CuInS_2$ NPs. These NPs occasionally possessed surface blemishes consistent with erosion, but only rarely contained complete perforations through the NPs. Thus, the erosion process evident in Figures 3.6 and 3.7 was inhibited at higher cation-exchange temperatures.

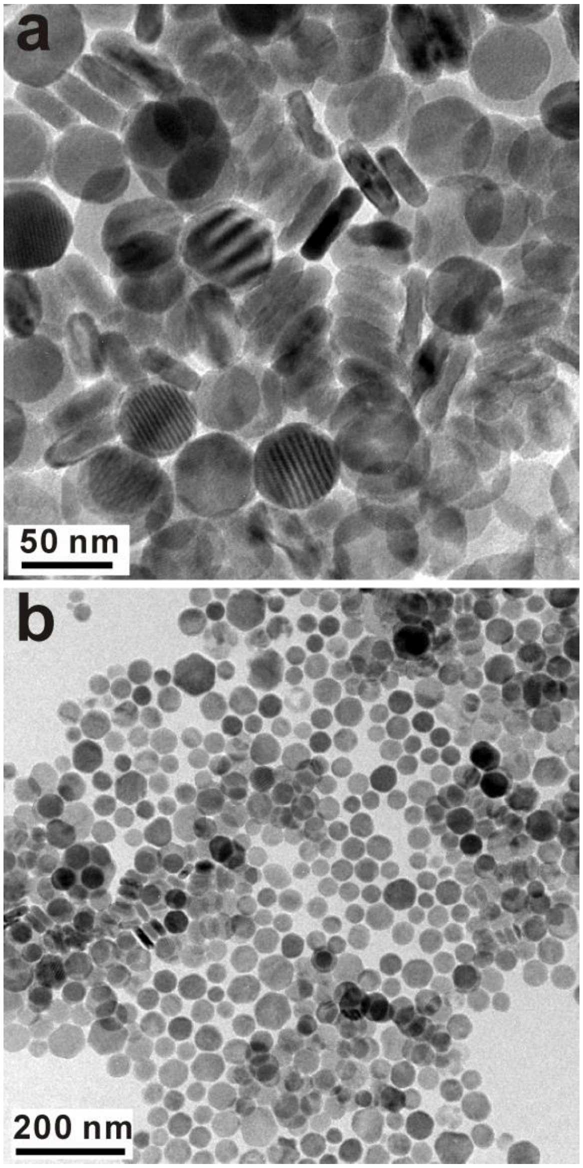

Figure 3.8. TEM images at two magnifications of $CuInS_2$ nanocrystals resulting from ion exchange between $Cu_{2-x}S$ NPs and $InCl_3$ (180 ℃). Fewer of the NPs are eroded, with comparatively smaller central holes, compared to the results obtained at a reaction temperature of 150 ℃.

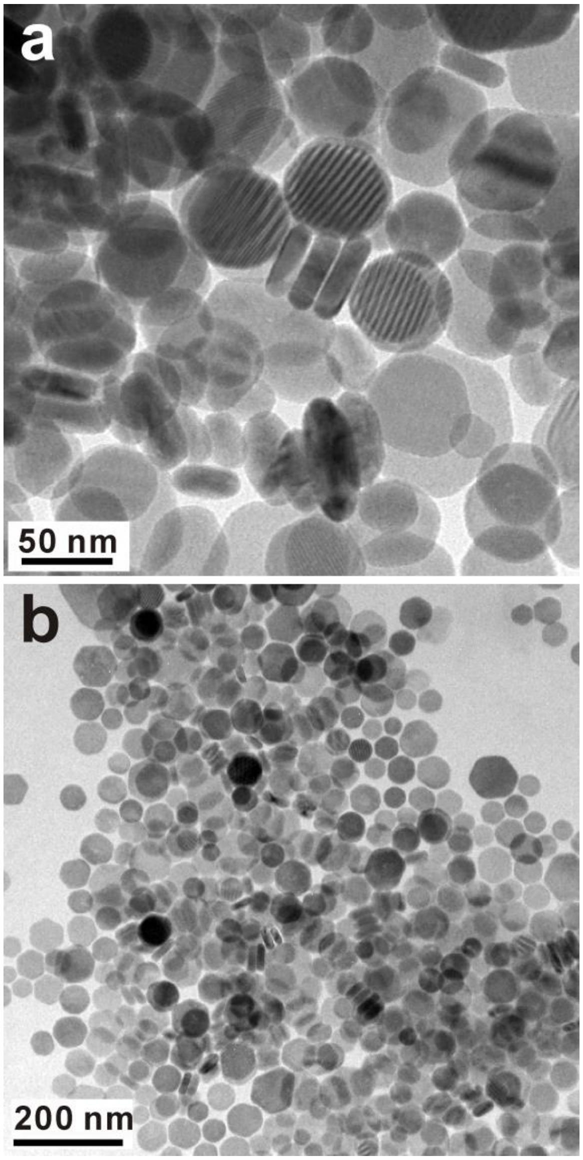

Figure 3.9. TEM images at two magnifications of $CuInS_2$ nanocrystals resulting from ion exchange between $Cu_{2-x}S$ NPs and $InCl_3$ (200 ℃). The NPs are nearly free of central holes and other thickness variations.

The extinction spectra of $CuInS_2$ nanocrystals prepared using $Cu_{2-x}S$ NPs and $InCl_3$ at 200 ℃ (a) and 150 ℃ (b) are exhibited in Figure 3.10. Both intact and hollow-centered NPs displayed a broad feature at around 730 nm in extinction spectra with a small blue shift from bulk bandgap. The quantum-confinement effect was not evident here because the 13-nm mean thickness of these NPs was more than twice the bulk exciton Bohr radius in $CuInS_2$ of 4 nm.[37]

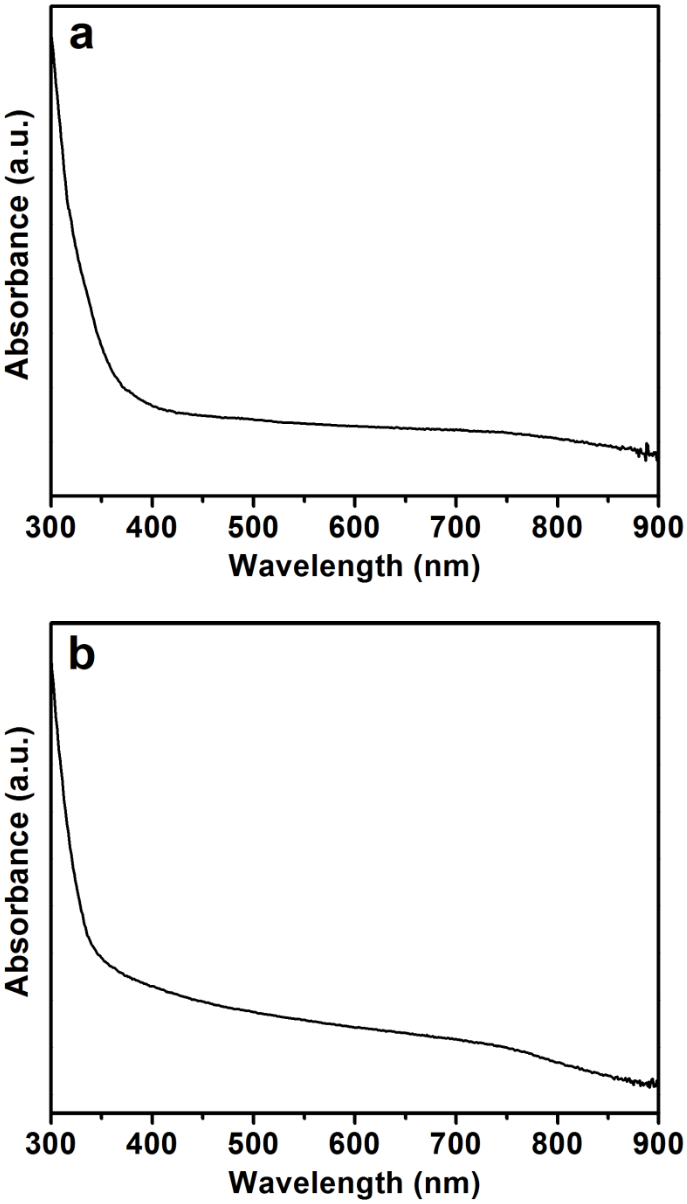

Figure 3.10. UV-visible extinction spectra of $CuInS_2$ nanocrystals with different morphologies resulting from ion exchange between $Cu_{2-x}S$ NPs and $InCl_3$. (a) Intact NPs (200 °C) and (b) Nanocrystals with central holes and other thickness variations (150 °C).

To determine the possible role of the In^{3+}-precursor identity in the cation-exchange and erosion processes, cation exchange was conducted with $Cu_{2-x}S$ NPs and InI_3, as previously described and at the lower temperature of 150 °C. An XRD pattern collected after 2 min of reaction time established the cation exchange to $CuInS_2$ to be complete (Figure 3.11). Figure

3.12 shows that the center-erosion process was enhanced with this precursor, resulting in nanorings having larger hollow centers in comparison to the cation exchange conducted with $InCl_3$. Close examination of several images like Figure 3.12a indicated that 61% of the NPs contained holes passing through the entire NP thickness, whereas 39% were thinned without complete perforations. The holes were distinguished by the clear observation of the holey-carbon-film background within them.

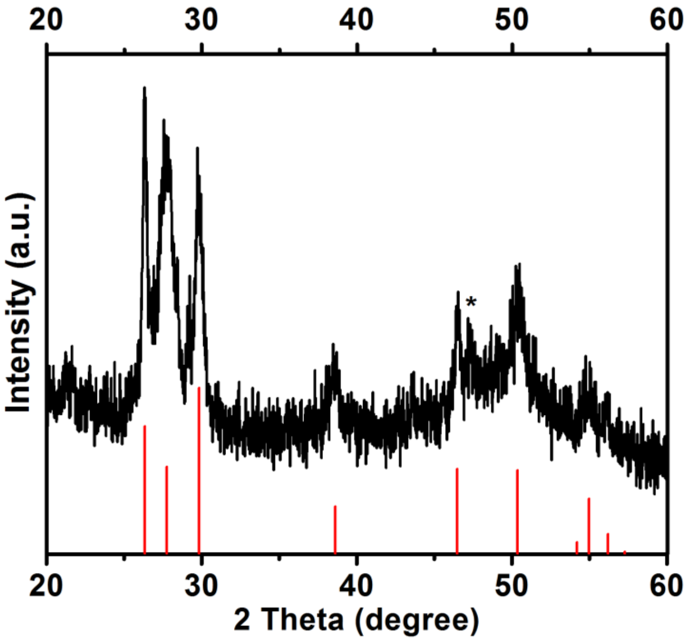

Figure 3.11. An XRD pattern of $CuInS_2$ nanocrystals resulting from ion exchange between $Cu_{2-x}S$ NPs and InI_3, compared to the reference pattern of $CuInS_2$ in the wurtzite structure. The asterisk identifies a peak arising from the silicon sample holder ($2\theta = 47.3°$).

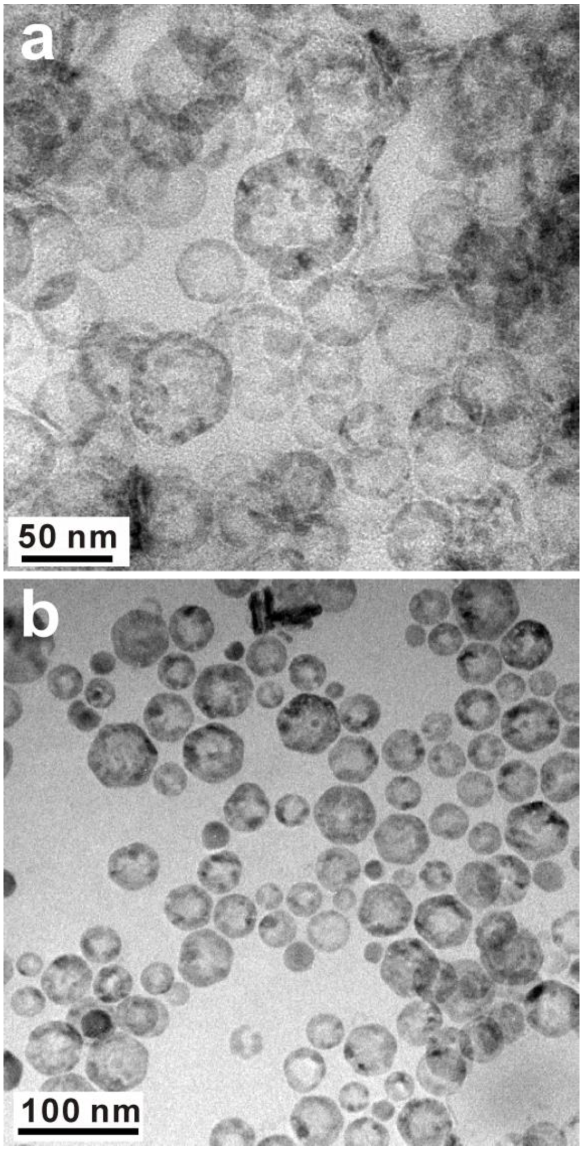

Figure 3.12. TEM images at two magnifications of $CuInS_2$ nanocrystals resulting from ion exchange between $Cu_{2-x}S$ NPs and InI_3 (150 °C), revealing large central holes and related thickness variations.

Statistical analysis of TEM images of the starting $Cu_{2-x}S$ NPs used in this synthesis gave mean widths of 44 ± 9 nm (Figure 3.13a). Similarly, the mean width of the resulting $CuInS_2$ nanorings and NPs was found to be 45 ± 9 nm (Figure 3.13b), whereas the mean width of the central openings was 12 ± 11 nm. (To construct the mean central-opening width, those NPs with thinning but incomplete perforations were assigned a hole size of zero.) These results will be analyzed in the Discussion. EDS analysis established these nanorings and thinned NPs to be slightly S deficient (28.1% Cu, 29.0% In, and 42.9% S).

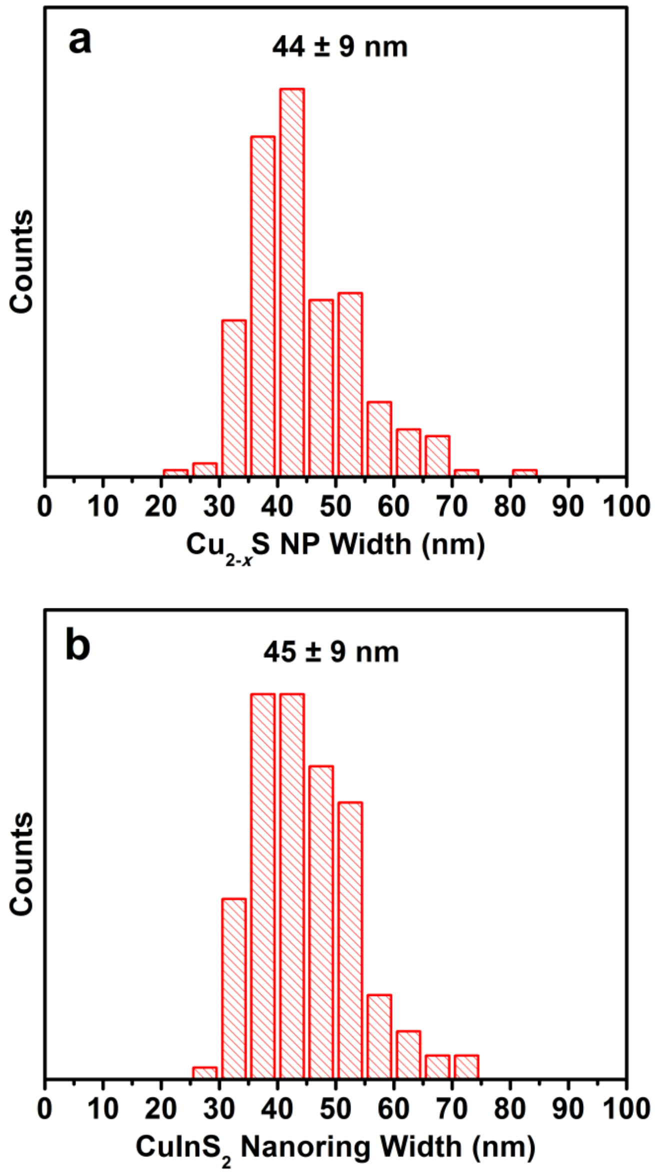

Figure 3.13. NP width distributions before and after ion exchange. (a) $Cu_{2-x}S$ NP width distribution. (b) $CuInS_2$ nanocrystal width distribution, resulting from ion exchange between $Cu_{2-x}S$ NPs and InI_3. The distributions yielded the mean size ± one standard deviation for each.

For comparison, cation exchange was also conducted with $Cu_{2-x}S$ NPs and $In(OAc)_3$ (in the stoichiometric amount to prepare $CuInS_2$) at 150 ℃. XRD patterns collected after 2 and 4 min revealed mixtures of djurleite and (wurtzitic) $CuInS_2$, indicating incomplete ion exchange at those times. An XRD pattern collected after 10 min confirmed complete exchange to $CuInS_2$ (Figure 3.14). The use of this In precursor resulted in fully dense, nearly blemish-free NPs, consistent with the elimination of the erosion process observed to some degree in most of the other cation-exchange reactions (Figure 3.15). Evidently, some characteristic of $In(OAc)_3$ allowed erosion-less exchange at the lowest reaction temperature investigated (150 °C), in contrast with the other precursors.

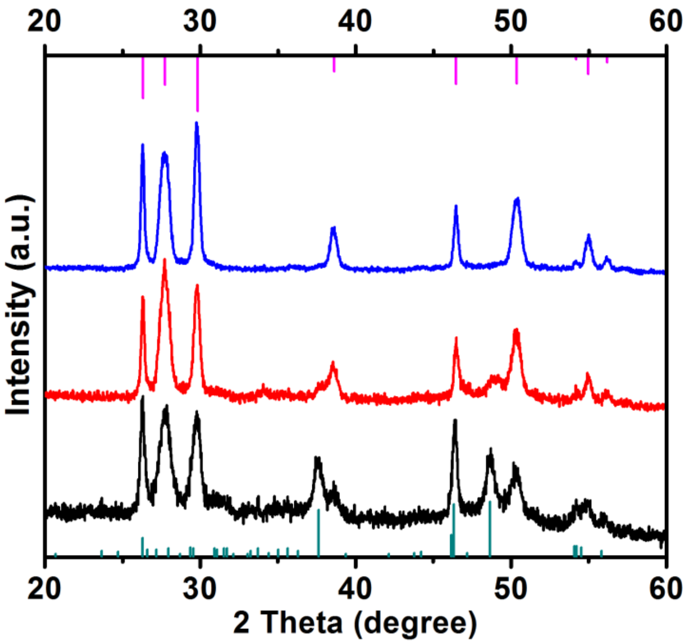

Figure 3.14. XRD patterns of $CuInS_2$ nanocrystals resulting from ion exchange between $Cu_{2-x}S$ NPs and $In(OAc)_3$ after 2 min (black), 4 min (red), and 10 min (blue), respectively, compared to the reference patterns of $CuInS_2$ in the wurtzite structure (ICDD-PDF 01-077-9459, magenta, top) and $Cu_{2-x}S$ in the djurleite structure (ICDD-PDF 00-023-0959, cyan, bottom).

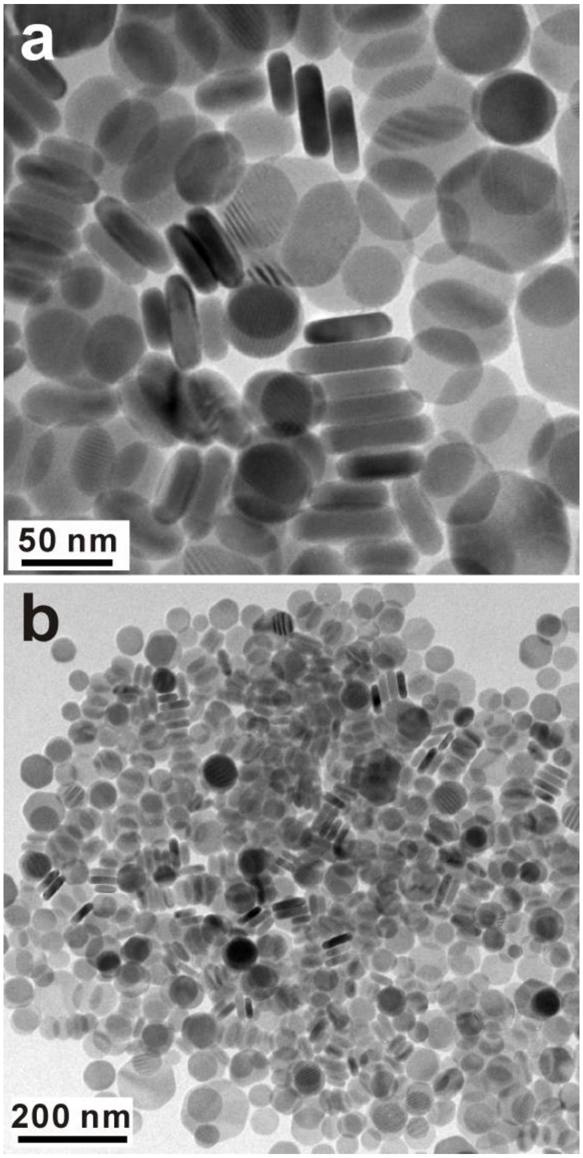

Figure 3.15. TEM images at two magnifications of $CuInS_2$ nanocrystals resulting from ion exchange between $Cu_{2-x}S$ NPs and $In(OAc)_3$ (150 ℃). The NPs are free of central holes and other thickness variations.

As stated above, the exchange process employing $In(OAc)_3$ at 150 ℃ gave intact $CuInS_2$ NPs, but required a longer reaction time to reach completion than the exchange reactions employing the In-halide precursors (10 min vs. 2 min). To assist in elucidating the mechanism of the cation exchange, a related exchange reaction was conducted with $In(acac)_3$ (in the stoichiometric amount to prepare $CuInS_2$) at 150 ℃. This process also afforded nearly fully intact, blemish-free $CuInS_2$ NPs (Figure 3.16). Reaction monitoring by XRD (Figure 3.17) established this exchange process to be even slower, requiring 30 minutes to achieve complete exchange.

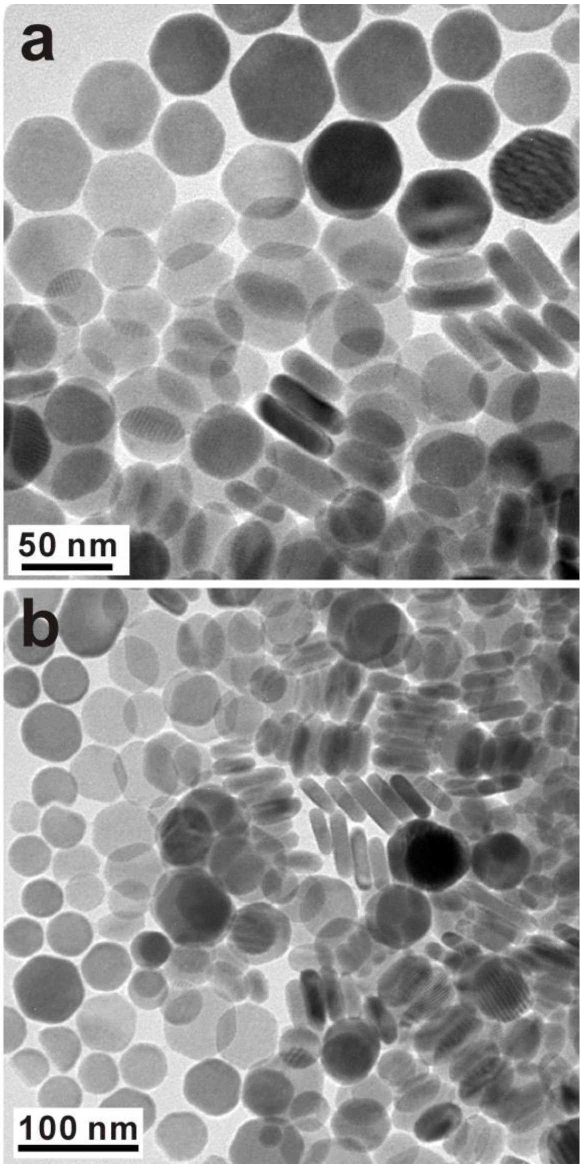

Figure 3.16. TEM images at two magnifications of $CuInS_2$ nanocrystals resulting from ion exchange between $Cu_{2-x}S$ NPs and $In(acac)_3$ (150 °C). The NPs are free of central holes and other thickness variations.

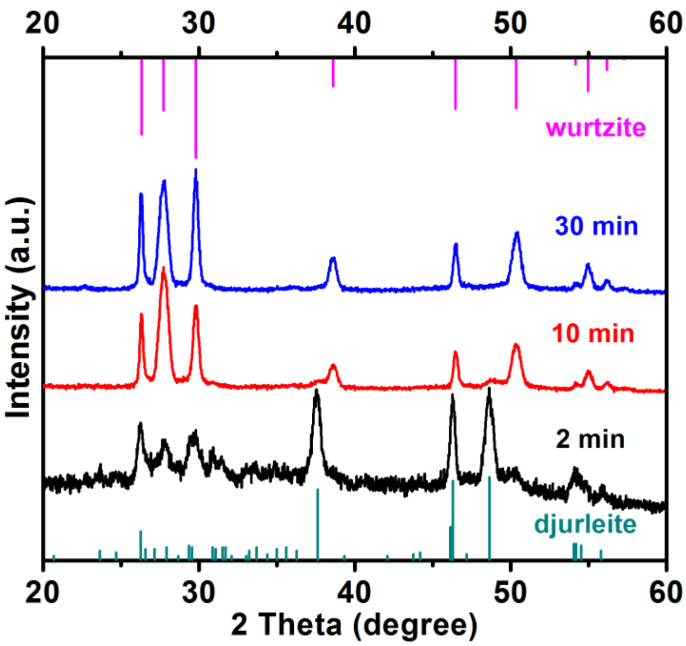

Figure 3.17. XRD patterns of $CuInS_2$ nanocrystals resulting from ion exchange between $Cu_{2-x}S$ NPs and $In(acac)_3$ after 2 min (black), 10 min (red), and 30 min (blue), respectively, compared to the reference patterns of $CuInS_2$ in the wurtzite structure (ICDD-PDF 01-077-9459, magenta, top) and $Cu_{2-x}S$ in the djurleite structure (ICDD-PDF 00-023-0959, cyan, bottom).

The relative slowness of the exchange processes with the $In(OAc)_3$ and $In(acac)_3$ precursors allowed NPs to be analyzed at an intermediate stage in the conversion of $Cu_{2-x}S$ to $CuInS_2$. Figure 3.18a and b are HRTEM images of the faces and edges of the starting $Cu_{2-x}S$ NPs (an FFT of the face image is inset in Fig. 3.18a). Figure 3.18e and f provide corresponding images of the fully exchanged product $CuInS_2$ NPs, including an FFT inset. The images in Figure 3.18c and d were obtained after 2 min into the 10-min exchange process using the precursor $In(OAc)_3$.

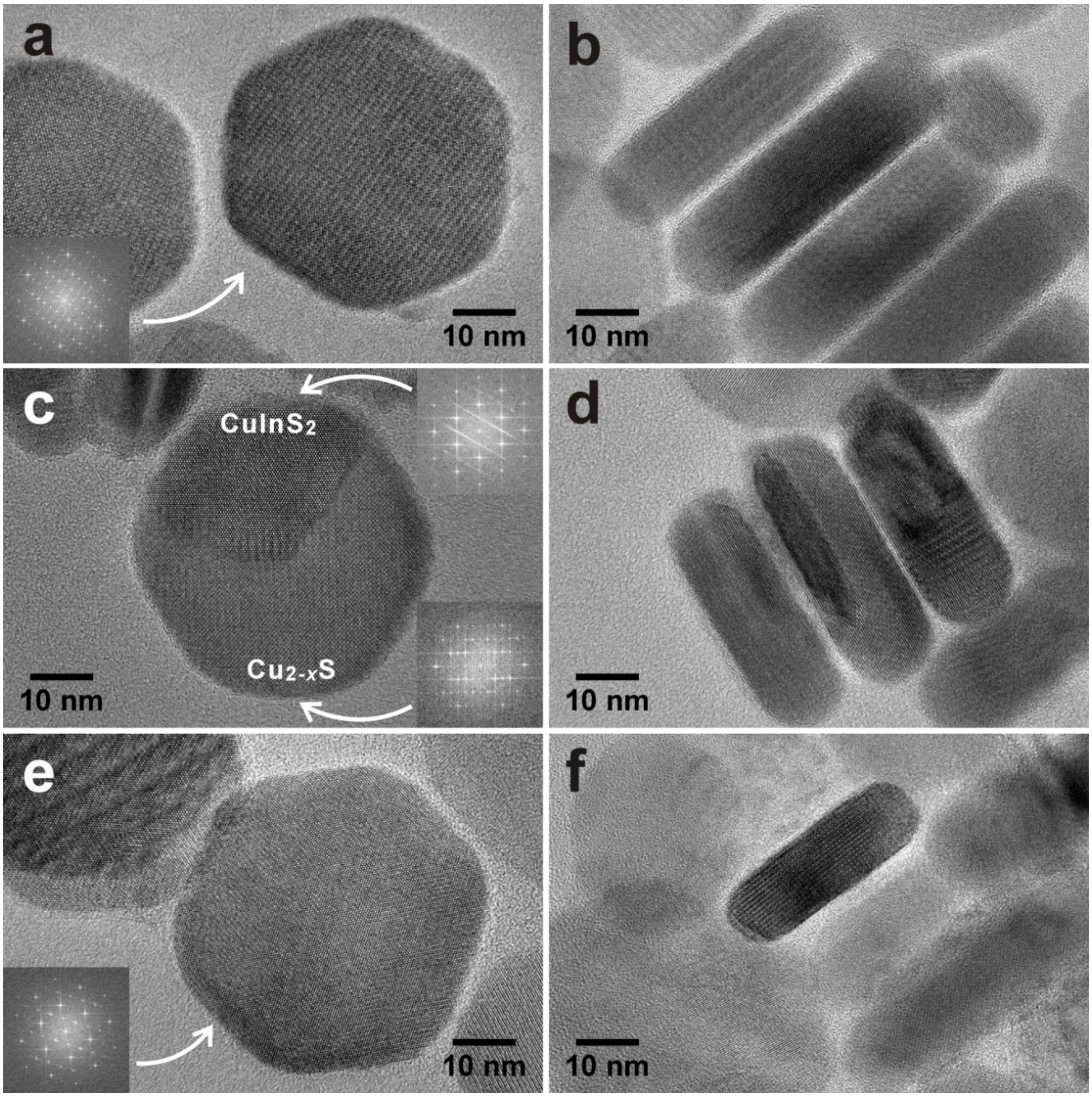

Figure 3.18. HRTEM images of NPs at different reaction stages during ion exchange between $Cu_{2-x}S$ NPs and $In(OAc)_3$ (150 ℃). (a) and (b) Initial $Cu_{2-x}S$ NPs. (c) and (d) Partially exchanged NPs at an intermediate stage (2 min). (e) and (f) $CuInS_2$ NPs after complete ion exchange.

Partial cation exchange was clearly evident in Figure 3.18c and d. Figure 3.18c contained a pie-like slice of $CuInS_2$ within a partially converted $Cu_{2-x}S$ NP. FFT images (inset) confirmed the structural assignments of these components. Figure 3.18d established that the substitution process could also propagate in time throughout the thickness dimension of the NP. Most of the NPs examined in this specimen were found to be partially converted (a few were unreacted).

Several additional HRTEM images of partially exchanged NPs are provided in Figure 3.19. These images are closely comparable to those reported by Manna and coworkers for partially cation-exchanged $Cu_{3-x}P$ NPs,[38] and consistent with cation exchange occurring through the NP edges (see below).

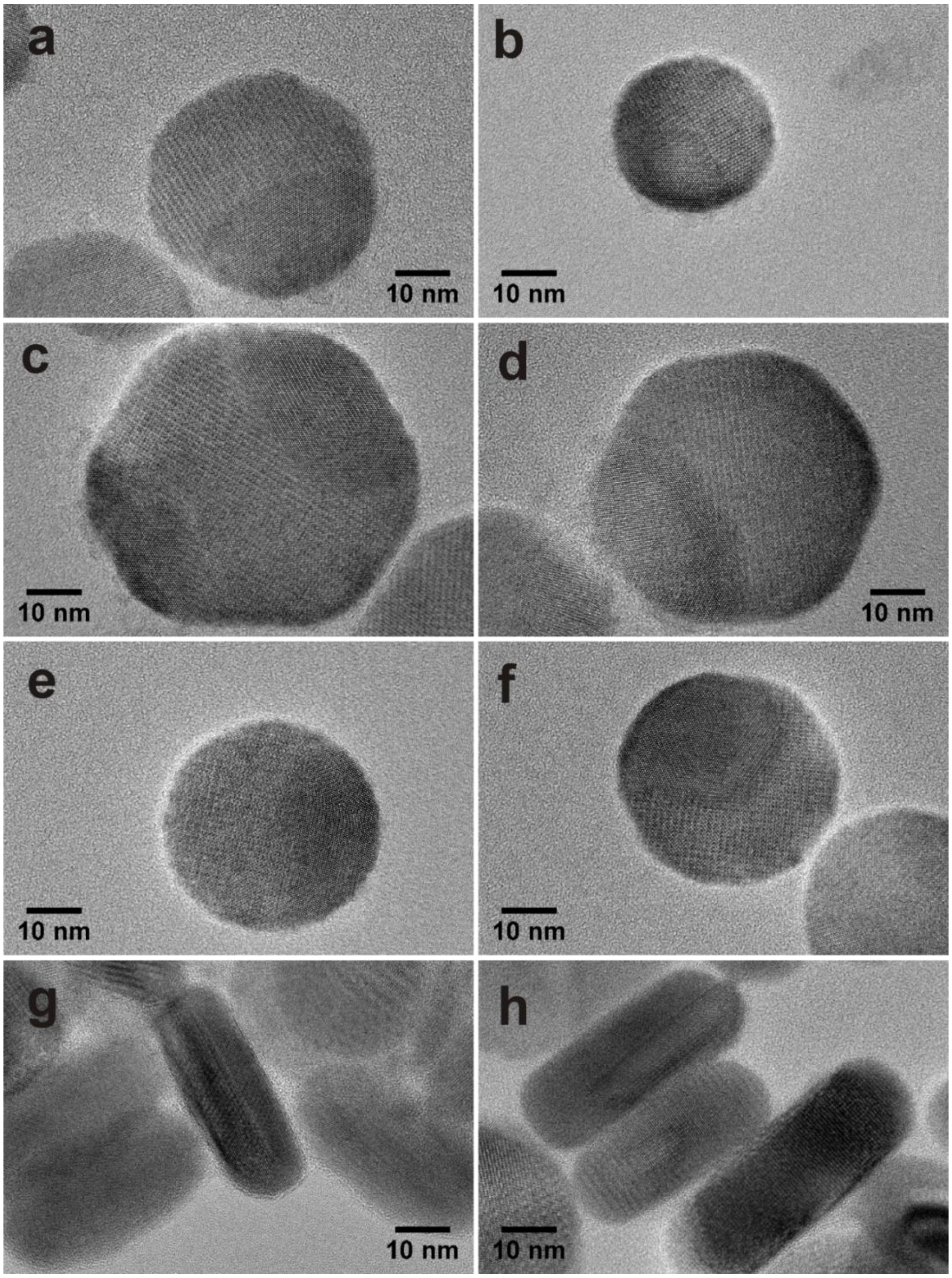

Figure 3.19. Additional HRTEM images of partially transformed NPs resulting from ion exchange between $Cu_{2-x}S$ NPs and $In(OAc)_3$ (150 ℃) after 2 min.

3.4 Discussion

3.4.1 Nanoscale Kirkendall Effect

The operative process in forming the holey $CuInS_2$ NPs and hollow-centered $CuInS_2$ nanorings is the nanoscale Kirkendall Effect, first reported by Alivisatos and coworkers.[39] The Kirkendall Effect is a diffusion-related phenomenon occurring between reactive phases sharing an interface. If a phase A consists of spherical nanoparticles and a shell of phase B is deposited upon the phase-A nanoparticles, then the morphology of the resultant AB product nanoparticles may depend upon the relative diffusion rates of A and B through the AB product phase forming at the core-shell interface. In the initial Alivisatos study, Co nanoparticles were allowed to react with elemental S. The out-diffusion of Co was faster than the in-diffusion of S, resulting in hollowed Co_3S_4 nanoparticles, by the nanoscale Kirkendall Effect.

The nanoscale Kirkendall Effect is a general phenomenon.[40,41] This research field has recently been reviewed.[42] Significantly, the Effect has been shown to operate during ion-exchange processes, which is of particular relevance to the present study.[43]

Several studies have shown that ion-exchange reactions with NPs are initiated at the thin platelet edges rather than indiscriminately upon the broad top and bottom facets.[38,44-47] For example, Manna and coworkers studied the conversion of $Cu_{3-x}P$ NPs to InP NPs by ion exchange with $InBr_3$.[38] Their results show clearly that InP first nucleates at the corners of the hexagonal $Cu_{3-x}P$ NPs, and that growth of the InP phase then propagates inward towards the centers of the NPs, until the entire NPs become transformed.

Cheon and coworkers have demonstrated that this basic mechanism is capable of converting NPs to nanotoroids or nanorings.[44-46] As shown in Figure 3.20, if ion-exchange occurs exclusively through the thin platelet edges, and if the out-diffusion of phase A is faster than the in-diffusion of B, then material is eroded from the center of the platelet and ultimately deposited near the edges, resulting in a ring or toroidal morphology. These morphologies form by the operation of the nanoscale Kirkendall Effect on NPs under the condition of exclusive edge diffusion.

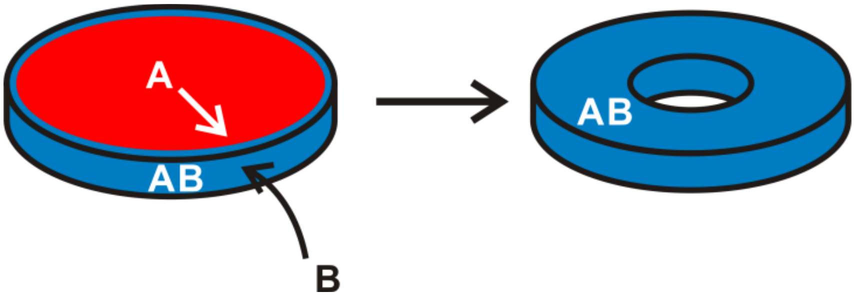

Figure 3.20. Schematic diagram depicting the operation of the Kirkendall Effect on NPs with out-diffusion of phase A and in-diffusion of phase B occurring only through the thin platelet edge.

An alternative pathway of indiscriminate ion exchange through the broad top and bottom facets, in which out-diffusion of A is faster than in-diffusion of B, would likely lead to the complete erosion of the NP, leaving no intact remnant behind. The top and bottom facets of NPs tend to be crystallographically flat, and well protected by self-assembled monolayers of ligand passivation, inhibiting ion exchange through those interfaces.[38] In contrast, thin NP edges generally tend to be ragged and defective, and less-well protected by ligation. Thus ion exchange through the thin edges apparently has a lower barrier.

If cation exchange indeed occurs through the NP edges and with the operation of the nanoscale Kirkendall Effect, but without Ostwald ripening or material loss, then the product $CuInS_2$ NPs may reasonably be expected to have larger mean widths than the starting $Cu_{2-x}S$ NPs. We used the results of the InI_3 substitution, which produced the largest central holes, to assess this expectation. The mean width of the resulting $CuInS_2$ nanorings may be predicted by adding the mean volume of the central holes to the perimeter of the initial $Cu_{2-x}S$ NP mean dimensions.

We calculated the expected final widths by approximating the NPs and resulting nanorings as circular disks (see below), using eq 3.2 and the mean NP and hole widths determined in the Results (Figure 3.13). In eq 3.2, *A* is the area of the NP lateral surface, *d* is the mean width of the NP.

$$A = \frac{1}{4}\pi d^2 \quad (3.2)$$

Before ion exchange, the mean area of $Cu_{2-x}S$ NPs with mean width d = 44.4 ± 9.1 nm was A = 1548 ± 635 nm^2. After ion exchange, $CuInS_2$ nanorings had a mean inner hole width d_i = 11.9 ± 11.2 nm and a mean outer width d_o = 44.9 ± 8.7 nm. The area of the hollow center was A_i = 111 ± 209 nm^2. If the total amount of the material remains the same after ion exchange, with the central part diffusing out to the surface of the $CuInS_2$ nanoring, the area of the ring A_r should be the same as that of the original $Cu_{2-x}S$ NP surface A. Then the calculated outer area of the ring is $A_c = A_r + A_i = A + A_i = 1659 \pm 844$ nm^2.

The final mean $CuInS_2$ NP width so approximated was d_c = 46 ± 12 nm, which is indistinguishable from the final mean width determined experimentally, d_o = 45 ± 9 nm. However, the final mean width determined experimentally was also indistinguishable from the mean width of the starting $Cu_{2-x}S$ NPs, d = 44 ± 9 nm. This analysis is complicated by the 39% of the product NPs lacking complete central holes. The expected mean NP width increase resulting from the operation of the nanoscale Kirkendall Effect is quite small, and our data are not able to show it.

3.4.2 Reaction Regimes for the Kirkendall Effect

Alivisatos and coworkers proposed four regimes for the reactions of phase-A particles with a phase B delivered to the particle surfaces by solution or gaseous deposition.[40] These regimes distinguish which reactions will result in solid AB particles with no hollowing, and which reactions will afford hollowed AB shells by the nanoscale Kirkendall Effect. Two of these reaction regimes are relevant to the results of the present study.

In the self-diffusion-limited regime,[40] the product nanostructure depends on the relative diffusion rates of A and B through the AB product phase. Hollowed particles form when the diffusion rate of A exceeds that of B. This scenario was presented above to introduce the nanoscale Kirkendall Effect. The high chalcocite phase of $Cu_{2-x}S$ exhibits high ionic conductivity associated with the high mobility of its constituent Cu^+ ions.[48] Thus, a more-rapid out-diffusion of Cu^+ and S^{2-} ions from phase A than in-diffusion of In^{3+} ions from phase B during ion exchange of the $Cu_{2-x}S$ NPs is readily imagined.

However, Cu^+ and S^{2-} should retain their diffusion-rate advantage at all temperatures studied, producing hollowed nanorings at all temperatures. Furthermore, the varying results obtained with the $InCl_3$, InI_3, $In(OAc)_3$, and $In(acac)_3$ precursors are not accounted for by the relative diffusion rates of Cu^+, S^{2-}, and In^{3+} ions within the NP crystal lattice, which should be the same, irrespective of precursor. Consequently, the ion-exchange processes investigated here do not appear to be operating within the self-diffusion-limited regime.

Another reaction regime identified by Alivisatos and coworkers is the collision-limited regime,[40] which we are adapting and renaming as the reaction-limited regime for the present discussion. The in-diffusion of In^{3+} into the $Cu_{2-x}S$ NPs is preceded by the adsorption of the InX_3 precursor on the NP edge facet (Figure 3.21). The X^- ligands from the precursor must be displaced to allow entry of the In^{3+} into the crystal lattice. Figure 3.21 suggests that such displacement occurs by nucleophilic attack of lattice S^{2-} ions on the adsorbed InX_3 precursor.

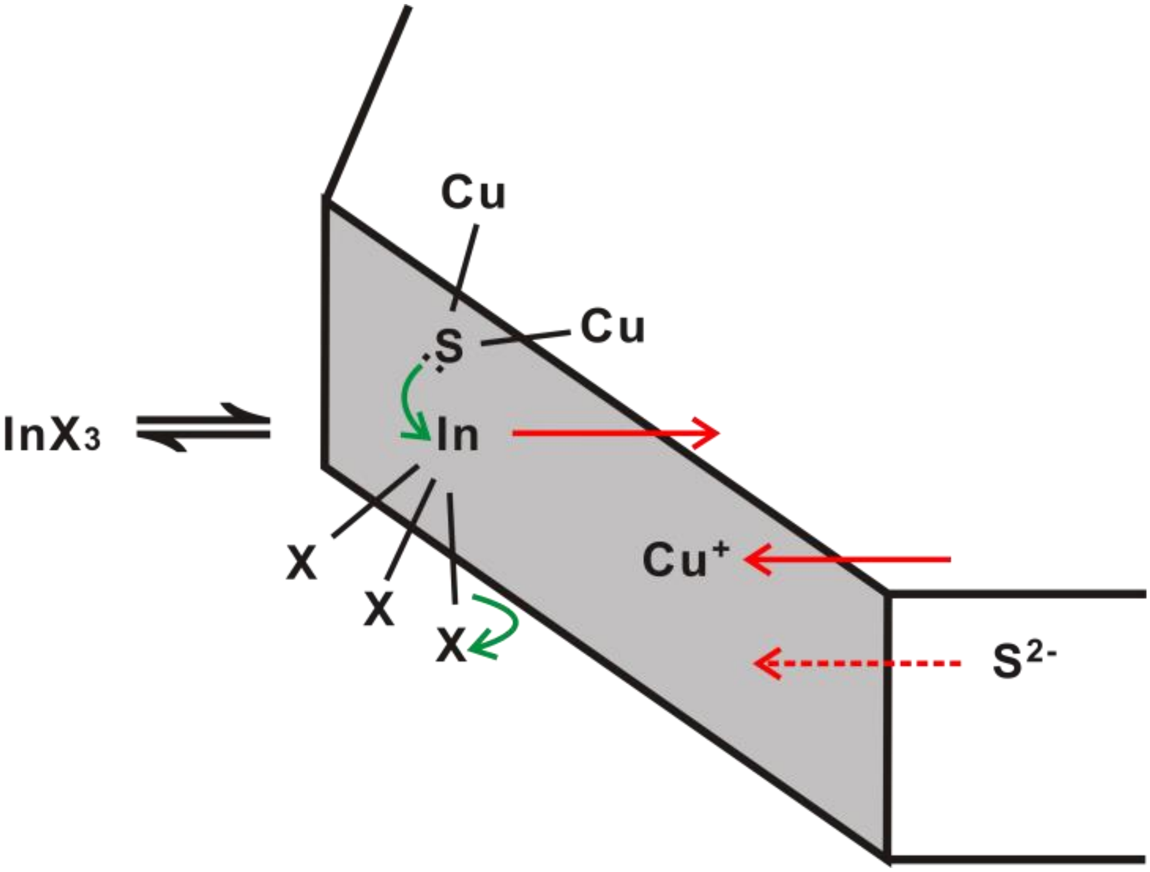

Figure 3.21. Schematic diagram depicting the edge adsorption of the InX_3 precursor, the nucleophilic displacement of X^- by a lattice S^{2-} ion, the in-diffusion of In^{3+}, and the out-diffusion of Cu^+ and S^{2-}.

Consequently, a reaction barrier or barriers must be overcome in this nucleophilic displacement process to insert In^{3+} ions into the $Cu_{2-x}S$ NPs. We propose the height of the reaction barrier to be determined by the leaving-group ability of the X^- ligands, in the sequence $I^- < Cl^- < {}^-OAc \approx CH_3C(O)CH_2C(CH_3)O^-$ ($acac^-$).[49] Thus the X^- displacement barriers scale with the ionicity of the InX_3 precursor, with the highest reaction barriers for InI_3, and the lowest for $In(OAc)_3$ and $In(acac)_3$.

High reaction barriers for In^{3+} entry at the NP edges decreases the effective rate of In^{3+} incorporation, and thus limits the availability of In^{3+} for in-diffusion, allowing the out-diffusion of $Cu_{2-x}S$ to outcompete the in-diffusion of In^{3+}. Hollow-centered $CuInS_2$ nanorings form under these conditions. In contrast, low reaction barriers for In^{3+} entry at the NP edges provide a higher rate of lattice In^{3+} incorporation, supporting balanced stoichiometries of In^{3+} in-diffusion and Cu^+ out-diffusion, given that the ion-exchange process is not diffusion limited (see above).

In the reaction-limited regime with low barriers for In^{3+} incorporation, ion exchange occurs to leave the fully dense NP morphology intact. The lower reaction barriers may be obtained either at higher temperature (as in for $InCl_3$), or with a better X^- leaving group (^-OAc or $acac^-$). Thus, the InX_3 precursor and reaction temperature determine the presence or absence of the nanoscale Kirkendall Effect, and therefore the final nanocrystal morphology resulting from the ion exchange. The Kirkendall Effect operates in the reaction-limited regime when the barriers for ion incorporation are high.

We note that the longer reaction times (10 and 30 min, respectively) required for ion exchange using $In(OAc)_3$ and $In(acac)_3$ than for $InCl_3$ or InI_3 (< 2 min) may seem in contradiction of the faster lattice incorporation of In^{3+} from $In(OAc)_3$ and $In(acac)_3$. However, adsorption of the InX_3 precursor onto the NP edge facet must precede In^{3+} incorporation, and we surmise that the adsorption pre-equilibrium lies further to the left in Figure 3.21 for the sterically encumbered $In(OAc)_3$ and $In(acac)_3$ precursors relative to the sterically smaller $InCl_3$ or InI_3 precursors. Because the acac ligand is larger than OAc, and because $In(acac)_3$ has a sterically saturated, 6-coordinate, pseudo-octahedral structure,[50] its adsorption pre-equilibrium lies even further leftward than that of $In(OAc)_3$, and consequently the overall exchange kinetics are the slowest for $In(acac)_3$. We further note that no driving force exists for the nanoscale Kirkendall

Effect *until* the InX_3 precursor is actually adsorbed onto the $Cu_{2-x}S$ NP. Thus we propose that the slower overall exchange kinetics for $In(OAc)_3$ and $In(acac)_3$ reflect slower effective adsorption kinetics due to the position of the adsorption pre-equilibrium.

The tendency of the nanoscale Kirkendall Effect to accompany ion-exchange processes in nanocrystals appears to be greater for nanocrystals having larger size dimensions. Thus, there is no hint of the Effect in small (2-8 nm), pseudospherical $Cu_{2-x}S$ nanocrystals undergoing ion exchange with In^{3+}.[23,24] Nor is hollowing or hole formation observed upon ion exchange in smaller $Cu_{2-x}S$ NPs having widths of 18 nm.[25] Interestingly, however, Hillhouse and coworkers published[51] strikingly beautiful hexagonal nanorings of $CuInSe_2$ having widths of 30-35 nm (see Figure 3 in ref 51). We surmise that these nanocrystals resulted from In^{3+} ion exchange into initially formed $Cu_{2-x}Se$ NPs, under the operation of the nanoscale Kirkendall Effect. The Kirkendall Effect is exacerbated in nanocrystals of larger dimension because of the lower *effective* rates of ion in-diffusion over the longer diffusion distances.

3.5 Conclusions

Ion exchange provides a means of preparing nanocrystals of complex ternary or quaternary phases from binary template nanocrystals. However, the nanoscale Kirkendall Effect must remain inactive to preserve the original morphology of the template nanocrystals. The use of molecular precursors to provide the exchange ions may cause the exchange process to occur in the reaction-limited regime, resulting in low relative rates of incorporation of the exchange ion, which triggers the nanoscale Kirkendall Effect and the consequent hollowing of the product nanocrystals. This effect is deactivated by the use of higher reaction temperatures, precursors of higher ionicity, or template nanocrystals of smaller dimension. The work in this chapter has been published on ACS Nano.[52]

3.6 References

1. Glennon, J. J.; Tang, R.; Buhro, W. E.; Loomis, R. A. *Nano Lett.* **2007**, *7*, 3290.

2. Wayman, V. L.; Morrison, P. J.; Wang, F.; Tang, R.; Buhro, W. E.; Loomis, R. A. *J. Phys. Chem. Lett.* **2012**, *3*, 2627.

3. Liu, Y.-H.; Wang, F.; Hoy, J.; Wayman, V. L.; Steinberg, L. K.; Loomis, R. A.; Buhro, W. E. *J. Am. Chem. Soc.* **2012**, *134*, 18797.

4. Liu, Y.-H.; Wang, F.; Wang, Y.; Gibbons, P. C.; Buhro, W. E. *J. Am. Chem. Soc.* **2011**, *133*, 17005.

5. Liu, Y.-H.; Wayman, V. L.; Gibbons, P. C.; Loomis, R. A.; Buhro, W. E. *Nano Lett.* **2010**, *10*, 352.

6. Wang, F.; Wang, Y.; Liu, Y.-H.; Morrison, P. J.; Loomis, R. A.; Buhro, W. E. *Acc. Chem. Res.* **2015**, *48*, 13.

7. Wooten, A. J.; Werder, D. J.; Williams, D. J.; Casson, J. L.; Hollingsworth, J. A. *J. Am. Chem. Soc.* **2009**, *131*, 16177.

8. Xu, J.; Lee, C.-S.; Tang, Y.-B.; Chen, X.; Chen, Z.-H.; Zhang, W.-J.; Lee, S.-T.; Zhang, W.; Yang, Z. *ACS Nano* **2010**, *4*, 1845.

9. Li, Q.; Zou, C.; Zhai, L.; Zhang, L.; Yang, Y.; Chen, X.; Huang, S. *CrystEngComm* **2013**, *15*, 1806.

10. Choi, Y.; Beak, M.; Yong, K. *Nanoscale* **2014**, *6*, 8914.

11. Wu, X.-J.; Huang, X.; Qi, X.; Li, H.; Li, B.; Zhang, H. *Angew. Chem., Int. Ed.* **2014**, *53*, 8929.

12. Li, Q.; Zhai, L.; Zou, C.; Huang, X.; Zhang, L.; Yang, Y.; Chen, X.; Huang, S. *Nanoscale* **2013**, *5*, 1638.

13. Qi, Y.; Liu, Q.; Tang, K.; Liang, Z.; Ren, Z.; Liu, X. *J. Phys. Chem. C* **2009**, *113*, 3939.

14. Sheng, X.; Wang, L.; Luo, Y.; Yang, D. *Nanoscale Res. Lett.* **2011**, *6*, 562.

15. Liu, X.; Wang, X.; Swihart, M. T. *Chem. Mater.* **2015**, *27*, 1342.

16. Koo, B.; Patel, R. N.; Korgel, B. A. *Chem. Mater.* **2009**, *21*, 1962.

17. Choi, S.-H.; Kim, E.-G.; Hyeon, T. *J. Am. Chem. Soc.* **2006**, *128*, 2520.

18. Connor, S. T.; Hsu, C.-M.; Weil, B. D.; Aloni, S.; Cui, Y. *J. Am. Chem. Soc.* **2009**, *131*, 4962.

19. Tomić, S.; Bernasconi, L.; Searle, B. G.; Harrison, N. M. *J. Phys. Chem. C* **2014**, *118*, 14478.

20. Ahmadi, M.; Pramana, S. S.; Xi, L.; Boothroyd, C.; Lam, Y. M.; Mhaisalkar, S. *J. Phys. Chem. C* **2012**, *116*, 8202.

21. Collord, A. D.; Hillhouse, H. W. *Chem. Mater.* **2015**, *27*, 1855.

22. Luther, J. M.; Zheng, H.; Sadtler, B.; Alivisatos, A. P. *J. Am. Chem. Soc.* **2009**, *131*, 16851.

23. van der Stam, W.; Berends, A. C.; Rabouw, F. T.; Willhammar, T.; Ke, X.; Meeldijk, J. D.; Bals, S.; de Mello Donega, C. *Chem. Mater.* **2015**, *27*, 621.

24. Akkerman, Q. A.; Genovese, A.; George, C.; Prato, M.; Moreels, I.; Casu, A.; Marras, S.; Curcio, A.; Scarpellini, A.; Pellegrino, T.; Manna, L.; Lesnyak, V. *ACS Nano* **2015**, *9*, 521.

25. Lesnyak, V.; George, C.; Genovese, A.; Prato, M.; Casu, A.; Ayyappan, S.; Scarpellini, A.; Manna, L. *ACS Nano* **2014**, *8*, 8407.

26. Hsu, S.-W.; On, K.; Tao, A. R. *J. Am. Chem. Soc.* **2011**, *133*, 19072.

27. Larsen, T. H.; Sigman, M.; Ghezelbash, A.; Doty, R. C.; Korgel, B. A. *J. Am. Chem. Soc.* **2003**, *125*, 5638.

28. Sigman, M. B.; Ghezelbash, A.; Hanrath, T.; Saunders, A. E.; Lee, F.; Korgel, B. A. *J. Am. Chem. Soc.* **2003**, *125*, 16050.

29. Bryks, W.; Wette, M.; Velez, N.; Hsu, S.-W.; Tao, A. R. *J. Am. Chem. Soc.* **2014**, *136*, 6175.

30. Hsu, S.-W.; Bryks, W.; Tao, A. R. *Chem. Mater.* **2012**, *24*, 3765.

31. Chen, Y.-B.; Chen, L.; Wu, L.-M. *Chem. - Eur. J.* **2008**, *14*, 11069.

32. Potter, R. W. *Econ. Geol.* **1977**, *72*, 1524.

33. Evans, H. T., Jr. *Science* **1979**, *203*, 356.

34. Buerger, M. J.; Wuensch, B. J. *Science* **1963**, *141*, 276.

35. Pan, D.; An, L.; Sun, Z.; Hou, W.; Yang, Y.; Yang, Z.; Lu, Y. *J. Am. Chem. Soc.* **2008**, *130*, 5620.

36. Lu, X.; Zhuang, Z.; Peng, Q.; Li, Y. *CrystEngComm* **2011**, *13*, 4039.

37. Czekelius, C.; Hilgendorff, M.; Spanhel, L.; Bedja, I.; Lerch, M.; Müller, G.; Bloeck, U.; Su, D.-S.; Giersig, M. *Adv. Mater.* **1999**, *11*, 643.

38. De Trizio, L.; Gaspari, R.; Bertoni, G.; Kriegel, I.; Moretti, L.; Scotognella, F.; Maserati, L.; Zhang, Y.; Messina, G. C.; Prato, M.; Marras, S.; Cavalli, A.; Manna, L. *Chem. Mater.* **2015**, *27*, 1120.

39. Yin, Y.; Rioux, R. M.; Erdonmez, C. K.; Hughes, S.; Somorjai, G. A.; Alivisatos, A. P. *Science* **2004**, *304*, 711.

40. Cabot, A.; Ibáñez, M.; Guardia, P.; Alivisatos, A. P. *J. Am. Chem. Soc.* **2009**, *131*, 11326.

41. Niu, K.-Y.; Park, J.; Zheng, H.; Alivisatos, A. P. *Nano Lett.* **2013**, *13*, 5715.

42. Wang, W.; Dahl, M.; Yin, Y. *Chem. Mater.* **2013**, *25*, 1179.

43. Liang, X.; Wang, X.; Zhuang, Y.; Xu, B.; Kuang, S.; Li, Y. *J. Am. Chem. Soc.* **2008**, *130*, 2736.

44. Jeong, S.; Han, J. H.; Jang, J.-t.; Seo, J.-w.; Kim, J.-G.; Cheon, J. *J. Am. Chem. Soc.* **2011**, *133*, 14500.

45. Han, J. H.; Lee, S.; Yoo, D.; Lee, J.-H.; Jeong, S.; Kim, J.-G.; Cheon, J. *J. Am. Chem. Soc.* **2013**, *135*, 3736.

46. Han, J. H.; Lee, S.; Cheon, J. *Chem. Soc. Rev.* **2013**, *42*, 2581.

47. Sines, I. T.; Vaughn, D. D.; Biacchi, A. J.; Kingsley, C. E.; Popczun, E. J.; Schaak, R. E. *Chem. Mater.* **2012**, *24*, 3088.

48. Hirahara, E. *J. Phys. Soc. Jpn.* **1951**, *6*, 428.

49. Lowry, T. H.; Richardson, K. S. *Mechanism and Theory in Organic Chemistry*; Harper & Row: New York, 1976.

50. Palenik, G. J.; Dymock, K. R. *Acta Crystallogr., Sect. B: Struct. Crystallogr. Cryst. Chem.* **1980**, *36*, 2059.

51. Guo, Q.; Kim, S. J.; Kar, M.; Shafarman, W. N.; Birkmire, R. W.; Stach, E. A.; Agrawal, R.; Hillhouse, H. W. *Nano Lett.* **2008**, *8*, 2982.

52. Mu, L.; Wang, F.; Sadtler, B.; Loomis, R. A.; Buhro, W. E. *ACS Nano* **2015**, *9*, 7419.

Chapter 4

Exciton Splitting in Thin Copper Indium Disulfide Nanosheets

4.1 Introduction

We report herein that thin (~ 2 nm) $CuInS_2$ nanosheets exhibit structured absorption (extinction) spectra having well-resolved absorption features, as is commonly observed for other semiconductor nanocrystals,[1] such as CdSe,[2-10] InP,[11,12] and PbS[13] nanocrystals. In contrast, the extinction spectra of other $CuInS_2$ nanocrystals are typically featureless, or nearly so, generally consisting of a rising absorption profile towards higher energy, with in some cases a very broad, and often minimally discernible peak.[14-18] The low resolution of these extinction spectra has been ascribed to nanocrystal size non-uniformity, morphological variations, and compositional inhomogeneities.[14-16]

We now show that resolved transitions in the extinction spectra of $CuInS_2$ nanosheets are due to partial resolution of the energy splitting between closely spaced A, B, and C excitons from the bulk band structure. This exciton splitting (valence-band splitting) has been observed in bulk crystals of $CuGa_xIn_{1-x}S_2$ ($x = 0 – 1$),[19-22] but to our knowledge not previously in I-III-VI_2 nanocrystals. We argue here that the energy splitting between these inequivalent excitons is enhanced in very thin $CuInS_2$ nanosheets by quantum-confinement effects, allowing the corresponding absorption features to be partially resolved.

We recently reported the preparation of (thick) $CuInS_2$ nanoplatelets by ion exchange from $Cu_{2-x}S$.[23] The nanoscale Kirkendall Effect was observed to operate under some reaction conditions, hollowing the nanocrystals, but not under other conditions, in which the morphology of the original $Cu_{2-x}S$ template nanocrystals was preserved. Our investigation led to increased mechanistic understanding and control of the Effect. However, because the 13-nm mean thickness of these nanoplatelets was more than twice the bulk exciton Bohr radius in $CuInS_2$ of 4 nm,[24] only very small quantum-confinement effects were discernible in the extinction spectra of these nanocrystals. The motivation for the present study was to look for evidence of one-dimensional (quantum-well-like) quantum confinement in much thinner $CuInS_2$ nanosheets. The exciton splitting reported here was observed in the course of this work. The synthesis of the thin $CuInS_2$ nanosheets, and the electronic-structure origin of the exciton splitting are detailed herein.

4.2 Experimental Section

4.2.1 Materials and General Procedures

$SnBr_4$ (99%), *n*-dodecylamine (98%), tri-*n*-octylphosphine (TOP, 97%), and $In(OAc)_3$ (99.99%, metal basis) were obtained from Sigma-Aldrich. Cu(OAc) (99%) was obtained from Strem Chemicals. All were used as received and stored under N_2. Tri-*n*-octylphosphine oxide (TOPO, 99%) from Sigma-Aldrich was purified by recrystallization and stored under N_2. 1-Octadecene (technical grade, 90%), hydrochloric acid (HCl, 37%), toluene (CHROMASOLV® for HPLC, 99.9%), methanol (≥99.8%), and 1-dodecanethiol (98%) were used as received from Sigma-Aldrich and stored under ambient conditions. Transmission electron microscopy (TEM) sample grids (Ni with holey carbon film) were obtained from Ted Pella, Inc. X-ray Diffraction (XRD) sample holders (zero-diffraction silicon plate, 24.6 mm diameter and 1.0 mm thickness, with cavity 10 mm diameter and 0.2 mm depth) were obtained from the MTI Corporation.

All synthetic procedures were conducted under dry N_2, except for the final purification steps, which were conducted in the ambient atmosphere.

4.2.2 Characterization Methods

Low-resolution TEM images and energy-dispersive X-ray spectroscopy (EDS) analysis data were collected using a JEOL 2000FX TEM operating at 200 kV. High-resolution TEM images were collected using a JEOL JEM-2100F field emission (FE) – scanning transmission electron microscope. Both low- and high-resolution TEM samples were prepared by dipping TEM grids into a toluene dispersion (5-6 mL) of a purified specimen, which were immediately removed to allow evaporation of the solvent. XRD patterns were collected and processed using a Bruker d8 Advance X-ray Diffractometer with Cu Kα radiation (λ = 1.541845 Å) and the Bruker Diffrac.Eva program. The XRD samples were prepared from toluene dispersions (0.5 mL) of purified specimens. Concentrated sample suspensions were drop cast onto a silicon sample holder, and dried in the fume hood. UV-visible spectra were collected using a Perkin Lambda 950 UV/Vis spectrometer. Spectral data were obtained from toluene dispersions of as-made $CuInS_2$ nanosheets, in quartz cuvettes.

4.2.3 Synthesis of Copper(I) Sulfide ($Cu_{2-x}S$) Nanosheets using $SnBr_4$ as the additive

$Cu_{2-x}S$ nanosheets were synthesized using $SnBr_4$ as the additive by adapting a literature method.[25] In a typical procedure, Cu(OAc) (0.024 g, 0.20 mmol), $SnBr_4$ (0.030 g, 0.068 mmol or 0.015 g, 0.034 mmol), TOPO (0.500g, 1.29 mmol) and 1-octadecene (9 g) were combined in a Schlenk tube, which was heated in a 100 ℃ oil bath for 30 min under evacuation (10^{-3} torr). The mixture was then placed under a dry N_2 atmosphere and transferred to a 160 ℃ salt bath ($NaNO_3/KNO_3/Ca(NO_3)_2$, 21%:54%:25% by mol). After the mixture was heated at 160 ℃ for 10 min, 1-dodecanethiol (0.400g, 2.00 mmol) was swiftly injected *via* syringe. The temperature of the reaction mixture was raised to 220 ℃ within 45 min, and then maintained at 220 ℃ for 1h. The reaction mixture after injection of 1-dodecanethiol was initially a light yellow solution, turned brown at 200 ℃, and darker with extended reaction time, finally forming a dark brown-black suspension.

4.2.4 Synthesis of Copper(I) Sulfide ($Cu_{2-x}S$) Nanosheets using HCl as the additive

$Cu_{2-x}S$ nanosheets were synthesized using HCl by adapting a literature method.[26] In a typical procedure, the experimental procedures were the same as those using $SnBr_4$ as the additive, except that 37% HCl (0.014 g, 0.14 mmol) was used instead of $SnBr_4$, which was added after the evacuation period, and the final heating temperature was 210 ℃ instead of 220 ℃.

4.2.5 Isolation of Copper(I) Sulfide ($Cu_{2-x}S$) Nanosheets

The nanosheets synthesized by the two methods above were isolated and purified by the following procedure. The reaction mixture was allowed to cool to room temperature under N_2. $Cu_{2-x}S$ nanosheets were isolated by adding toluene and methanol (6 mL total, volume ratio 2:1), followed by centrifugation for 5 min at 1500 rpm and removal of the supernatant. This purification procedure was repeated twice, before the $Cu_{2-x}S$ nanosheets were redispersed in toluene for cation exchange, and TEM or XRD characterization.

4.2.6 Synthesis of Copper(I) Indium Sulfide ($CuInS_2$) Nanosheets by Cation Exchange

In a typical procedure, $In(OAc)_3$ (0.004 g, 0.01 mmol) was dissolved in TOP (1 g) with *n*-dodecylamine (0.030 g, 0.16 mmol) after sonication for 20 min at room temperature and subsequent heating at 160 ℃ for 10 min. As-made $Cu_{2-x}S$ nanosheets (0.05 mmol) were purified following the procedure above and dispersed in toluene (1 mL). The $Cu_{2-x}S$ dispersion was then injected into a Schlenk tube loaded with dodecylamine (0.185g, 1 mmol), and evacuated (10^{-3} torr) to remove the toluene. The resulting dodecylamine dispersion was heated in a salt bath (at 120 ℃) for 5 min, and the $In(OAc)_3$ solution was swiftly injected *via* syringe into the black $Cu_{2-x}S$ suspension. The reaction mixture was held at 120 ℃ for 45 min, forming a red-brown, brown, or black suspension (depending on the thickness of the initial $Cu_{2-x}S$ nanosheets).

The reaction mixture was allowed to cool to room temperature, and the product $CuInS_2$ nanosheets were isolated by addition of toluene and methanol (6 mL total, volume ratio 2:1), followed by centrifugation for 5 min at 1500 rpm, and removal of the supernatant. This purification procedure was repeated twice, and then the $CuInS_2$ nanosheets were redispersed in toluene for TEM and XRD characterization. The as-made $CuInS_2$ nanosheets were dispersed in toluene for UV-visible spectroscopy.

4.3 Results

4.3.1 Preparation of $CuInS_2$ nanosheets

The target nanosheets were prepared by the ion-exchange process represented in eq 4.1.[23] The method of de Mello Donega and coworkers was employed to synthesize the starting, template $Cu_{2-x}S$ ($x \approx 0.03$-0.07)[27] nanosheets.[25] As a brief historical perspective, nanoplatelets of $Cu_{2-x}S$ are produced by thermolysis of Cu(I) dodecanethiolate.[28,29] In more recent work, the introduction of tin halides or hydrogen halides as synthetic additives during thermolysis was found to increase selectivity for sheet-like nanocrystal morphologies,[30,31] and to promote the formation of very thin (≈ 2 nm) $Cu_{2-x}S$ nanosheets.[25,26] We employed $SnBr_4$ as the morphology-control additive according to the conditions outlined by de Mello Donega and coworkers.[25]

$$2Cu_2S + In(OAc)_3 \longrightarrow CuInS_2 + 3Cu(OAc) \quad (4.1)$$

Face views from TEM images of the $Cu_{2-x}S$ nanosheets prepared in this manner are given in Figure 4.1a and b. Roughly hexagonal and triangular morphologies were observed, as previously reported.[25,31] The mean lateral dimensions of the hexagons (149 ± 10 nm) and triangles (66 ± 9 nm) were also comparable to the prior report.[25]

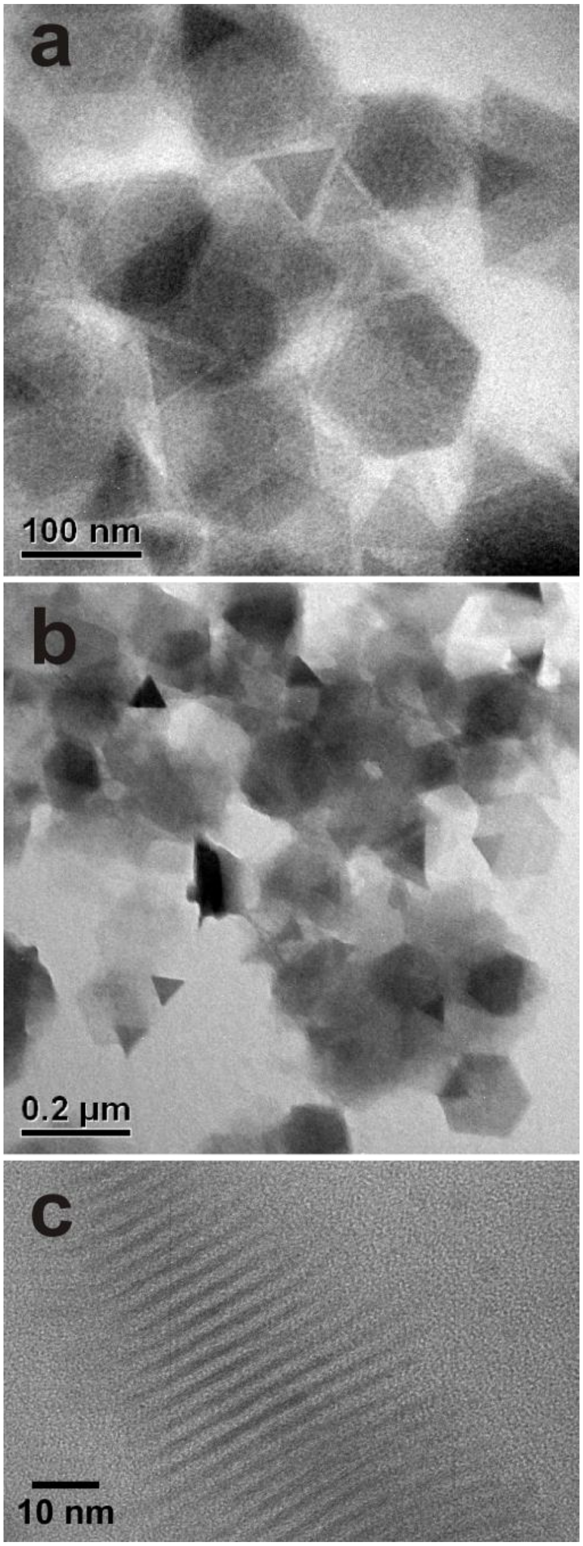

Figure 4.1. TEM images of $Cu_{2-x}S$ nanosheets. (a, b) face views; (c) edge view of a bundled stack.

The mean thickness of the $Cu_{2-x}S$ nanosheets was estimated in two ways. A high-resolution TEM image of a bundled stack of $Cu_{2-x}S$ nanosheets is shown in Figure 4.1c. The mean thickness of the nanosheets measured from such images was 1.73 ± 0.09 nm. Figure 4.2a is a low-angle XRD pattern collected from $Cu_{2-x}S$ nanosheet bundles, which exhibited a series of 00ℓ reflections characteristic of a periodic lamellar mesophase. A lamellar spacing of $d = 3.36 \pm 0.04$ nm was extracted from the peak positions. Following the prior analysis of de Mello Donega and coworkers,[25] subtraction of the length of a dodecanethiolate monolayer (1.77 nm) from d gave a mean $Cu_{2-x}S$ nanosheet thickness of 1.59 ± 0.04 nm. These values were in good agreement with the mean thickness of 2.0 nm reported in the original study.[25]

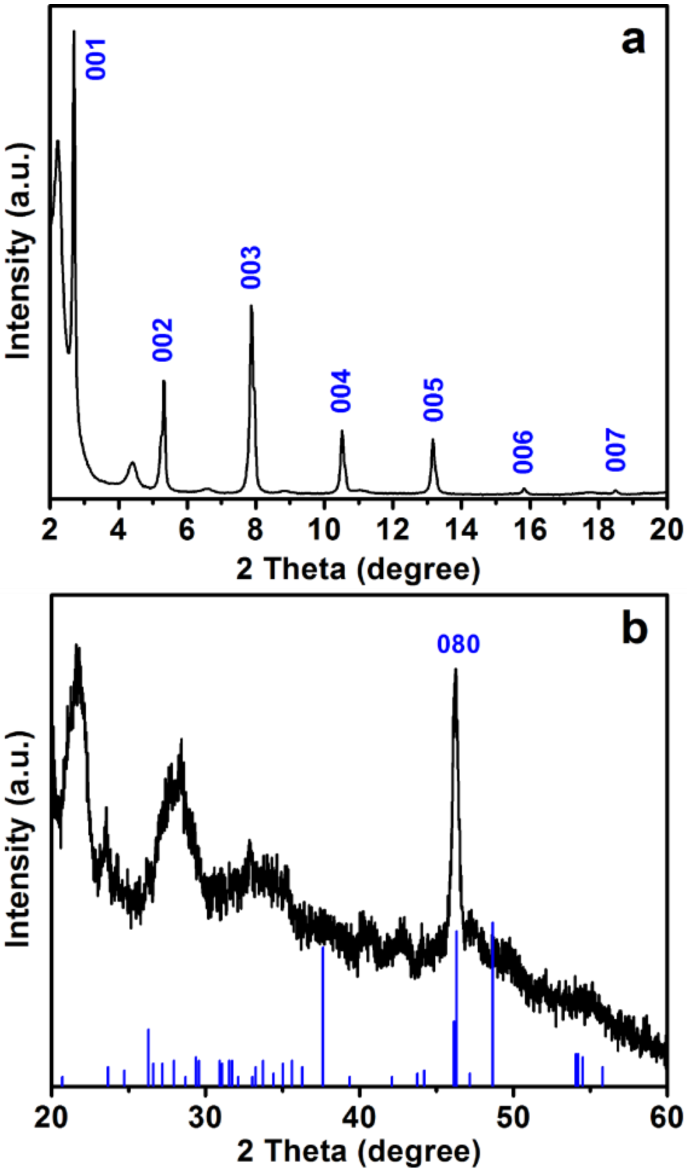

Figure 4.2. XRD patterns of $Cu_{2-x}S$ nanosheet bundles. (a) low-angle pattern; (b) higher-angle pattern in the region of the normal lattice reflections. The (blue) stick pattern in b corresponds to djurleite.

A standard (higher-angle) XRD pattern obtained from the $Cu_{2-x}S$ nanosheets contained only a single sharp reflection, at 46.25° 2θ (Figure 4.2b). The pattern resembled those previously collected from $Cu_{2-x}S$ nanosheets prepared similarly.[25,31,32] A crystal structure may not be confidently assigned on the basis of a single reflection from an XRD pattern, and various structures have been suggested for $Cu_{2-x}S$ nanosheets.[25,32] However, we note that the sharp peak in Figure 4.2b indexes to the 080 reflection of (monoclinic) djurleite, which is the structure we previously assigned to thicker $Cu_{2-x}S$ nanoplatelets prepared by a related method.[23] Solid specimens of $Cu_{2-x}S$ nanosheets consisted of individual and variously sized bundled stacks of nanosheets having random orientations (Figure 4.1). Thus, the sharpness of the 080 reflection indicated that the y axis of the assumed djurleite structure lay in the plane of the nanosheets.

Yi and Gao previously characterized the crystallographic orientation of djurleite nanosheets similarly prepared by thermolysis of Cu(I) dodecanethiolate, in the presence of $SnCl_4$.[31] They demonstrated that the large top and bottom nanosheet facets indexed to (100) planes from the monoclinic djurleite crystal structure of $Cu_{2-x}S$. Thus, the *normal* to the pseudo close-packed S^{2-} planes in the djurleite structure, which is near parallel to the x axis ($\beta = 90.13°$),[33] was near perpendicular to the plane of the nanosheets.[34] We argue below that this orientation of the anion sublattice was retained in the ion-exchanged $CuInS_2$ nanosheets (eq 4.1).

Nanosheets having two additional thicknesses were prepared by modifications of the method above. A reduction in the amount of the $SnBr_4$ additive produced $Cu_{2-x}S$ nanosheets having an increased thickness. A mean thickness of 2.61 ± 0.22 nm was determined by measurement from TEM images of nanosheet bundles oriented to provide edge views (Figure 4.3a). In a second synthetic modification, HCl was employed as the morphology-control additive.[26] The mean nanosheet thickness produced by this synthesis and determined similarly (Figure 4.3b) was 1.97 ± 0.13 nm. We also measured the lamellar d spacings in the nanosheet bundles by low-angle XRD for these specimens (Figure 4.4), but because of uncertainty in the true thicknesses of the ligand-passivation layers separating the $Cu_{2-x}S$ nanosheets in the bundles, the nanosheet thicknesses determined from the TEM images were considered to be more reliable.

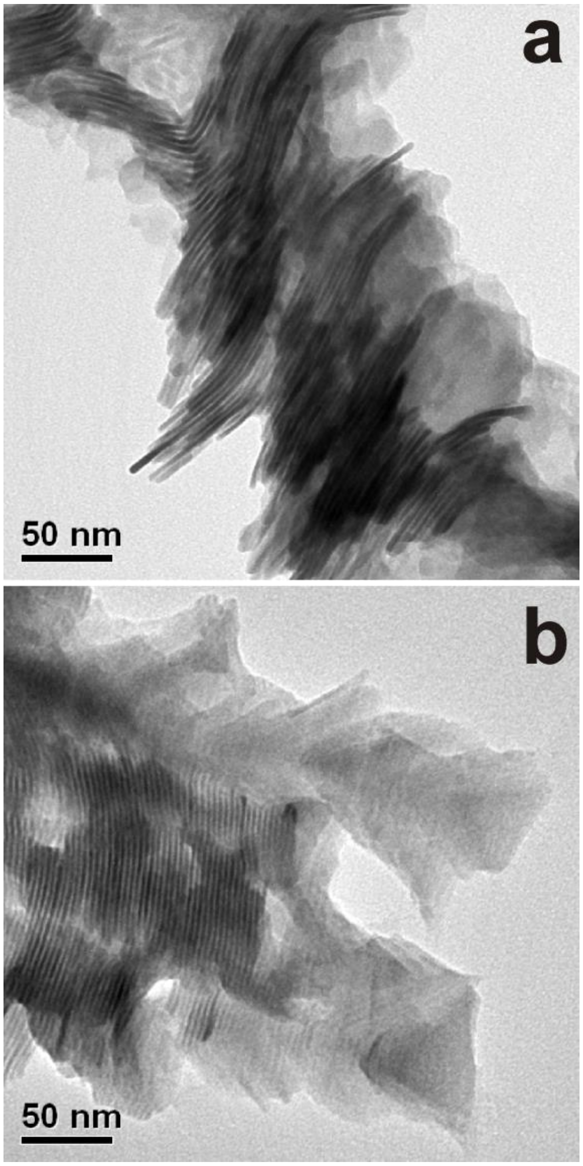

Figure 4.3. TEM images providing edge views of $Cu_{2-x}S$ nanosheets having two additional thicknesses. (a) $Cu_{2-x}S$ nanosheets with a thickness of 2.61 ± 0.22 nm. (b) $Cu_{2-x}S$ nanosheets with a thickness of 1.97 ± 0.13 nm.

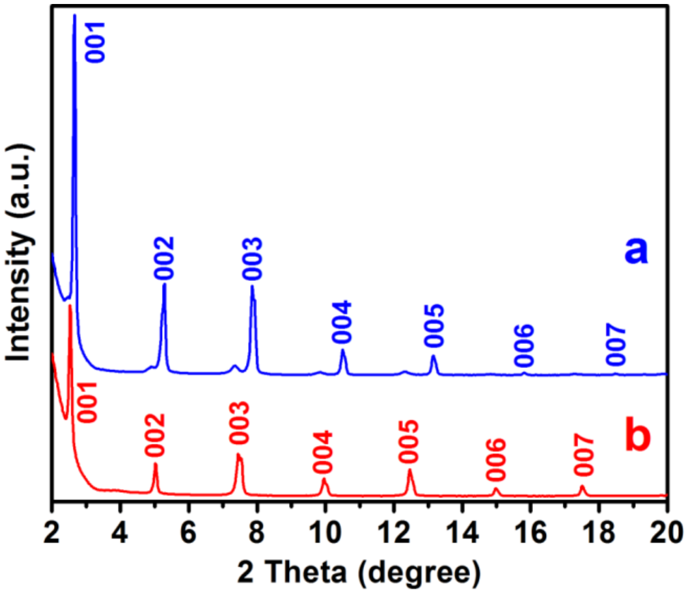

Figure 4.4. Low-angle XRD patterns of $Cu_{2-x}S$ nanosheets having two additional thicknesses. (a) $Cu_{2-x}S$ nanosheets with a thickness of 2.61 ± 0.22 nm. (b) $Cu_{2-x}S$ nanosheets with a thickness of 1.97 ± 0.13 nm.

Assumption of the djurleite crystal structure with the x axis normal to the sheets (see above), which has 8 near-perpendicular pseudo-close-packed monolayers (MLs) of anion (S^{2-}) sublattice per lattice parameter a,[34] allowed calculation of the discrete ML thicknesses of the three $Cu_{2-x}S$ nanosheet specimens described above ($a/8 = 0.3362$ nm). The thickest nanosheets (2.61 nm) corresponded to 8 MLs, the thinner (1.97 nm) to 6 MLs, and the thinnest (1.73 nm) to 5 MLs. The thicknesses were also characterized spectroscopically after ion exchange to $CuInS_2$ (see below). Although in principle we should have been able to prepare specimens having 7-ML (and likely other discrete ML) thicknesses, variations of reaction conditions afforded only those corresponding to 5, 6, and 8 ML discrete thicknesses. We return to this point later.

Ion-exchange of the $Cu_{2-x}S$ nanosheets having the three discrete thicknesses was conducted according to eq 4.1 at 120 ℃, affording $CuInS_2$ nanosheets. After ion exchange, the nanosheets were aggregated into irregular bundles. Face views of such nanosheet assemblies are shown in

Figure 4.5. TEM images of edges of the stacked bundles are given in Figure 4.6. Images of the nanosheet faces (Figure 4.5) had dappled appearances, which may have indicated thickness variations or perforations in the nanosheets.[23] However, we observed that such contrast variations increased with the time of exposure under the electron beam in the TEM (Figure 4.7), and so beam damage may have been responsible for the dappling of these very thin nanosheets.

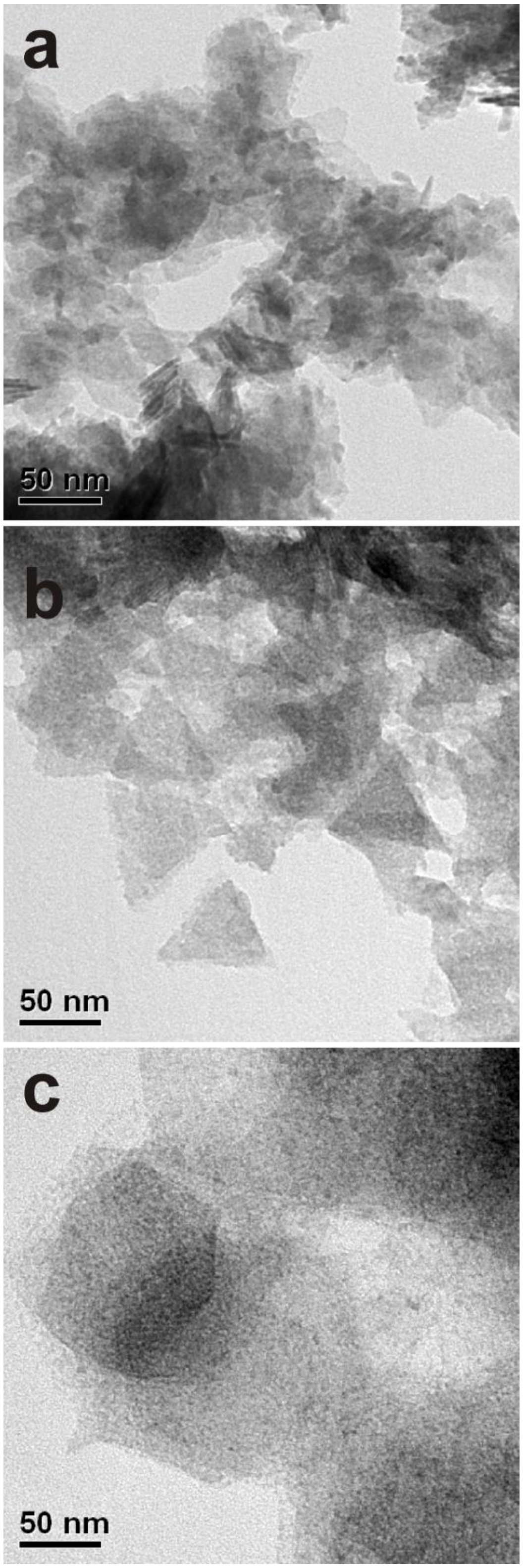

Figure 4.5. TEM images of $CuInS_2$ nanosheets of various thicknesses. (a) thickest nanosheets (8-ML); (b) thinner nanosheets (6-ML); (c) thinnest nanosheets (5-ML).

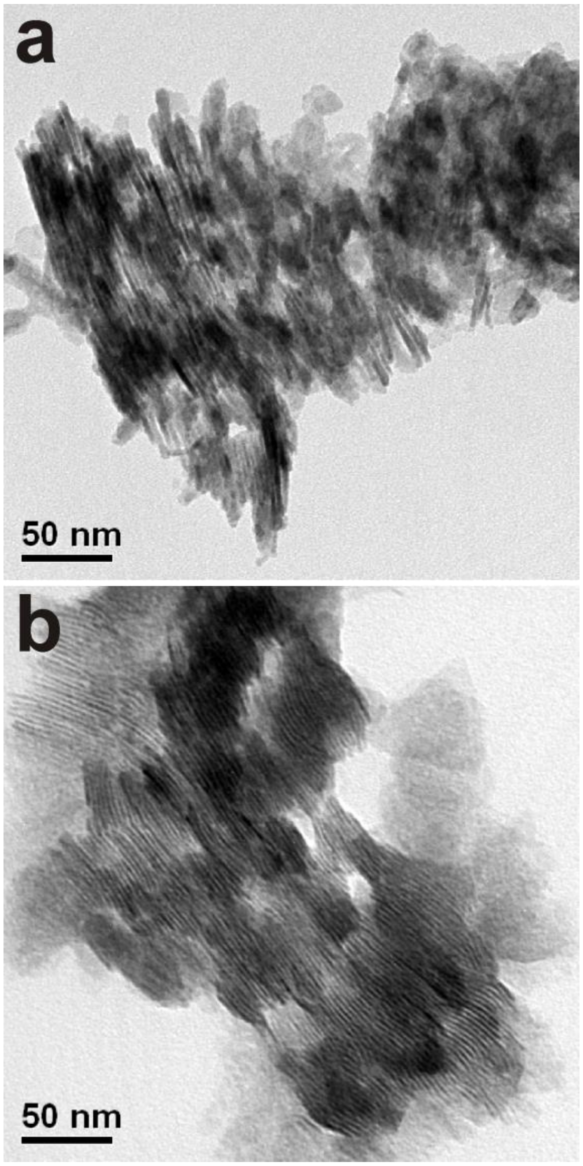

Figure 4.6. TEM images of irregular bundles of CuInS$_2$ nanosheets after ion exchange from (a) Cu$_{2-x}$S nanosheets with a thickness of 2.61 ± 0.22 nm (8 MLs). (b) Cu$_{2-x}$S nanosheets with a thickness of 1.97 ± 0.13 nm (6 MLs).

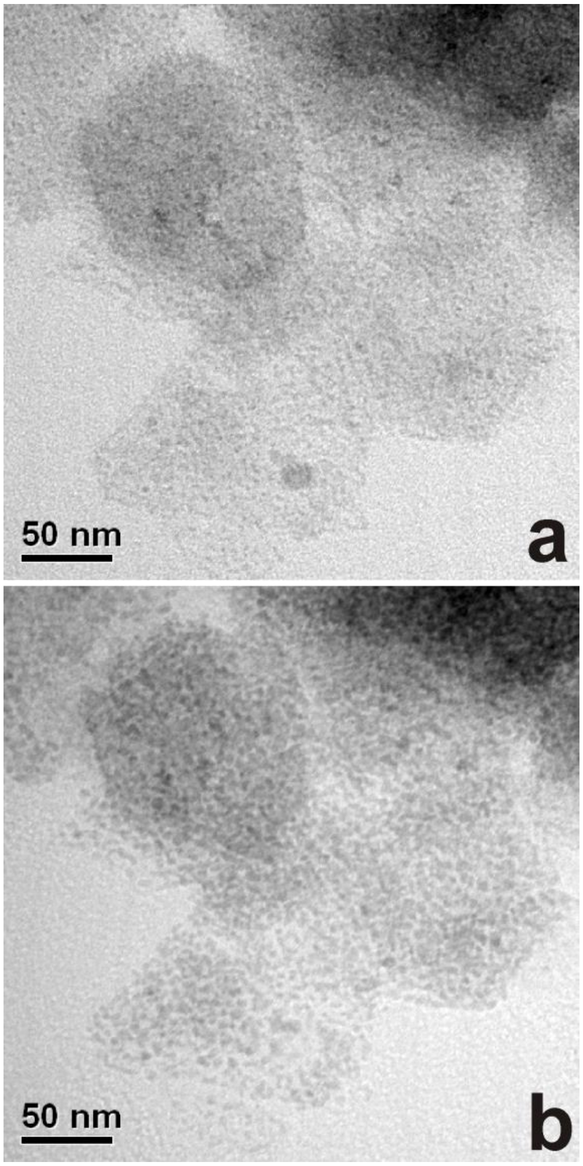

Figure 4.7. TEM images of the thinnest $CuInS_2$ nanosheets (5 MLs). Comparison between (a) before and (b) after exposure under the electron beam for 10 min shows increased variations in nanosheet thickness.

The compositions of the exchanged $CuInS_2$ nanosheets were determined by energy-dispersive x-ray spectroscopy (EDS) in the TEM. The values given here were averages of measurements taken from various positions in multiple samples (Table 4.1). The thinnest (5 ML) $CuInS_2$ nanosheets possessed the molar percentages of 26.1 ± 1.9 Cu, 26.3 ± 1.7 In, and 47.6 ± 2.0 S. The thinner (6 ML) and thin (8 ML) specimens were 27.0 ± 0.9 Cu, 29.0 ± 2.0 In, and 44.0 ±1.7 S, and 25.7 ±0.9 Cu, 28.6 ±1.2 In, and 45.7 ±0.5 S, respectively. These average values were close to the ideal values, and possibly reflected slight S deficiencies, which may have also resulted from beam damage to the very thin specimens.

Table 4.1. Composition of $CuInS_2$ nanosheets after complete ion exchange from $Cu_{2-x}S$ nanosheets with three different thicknesses, determined by EDS.[a]

Thickness of template $Cu_{2-x}S$ nanosheets (nm)	**Cu : In : S molar ratio**	
	At different spots	**Mean**
1.73 ±0.09	25.82% : 29.85% : 44.33% 30.12% : 23.92% : 45.96% 25.01% : 25.39% : 49.60% 23.44% : 25.95% : 50.62%	(26.1 ±1.9)% : (26.3 ±1.7)% : (47.6 ±2.0)%
1.97 ±0.13	26.99% : 25.65% : 47.36% 27.69% : 26.58% : 45.73% 28.63% : 29.40% : 41.97% 25.27% : 33.17% : 41.56% 26.36% : 30.14% : 43.50%	(27.0 ±0.9)% : (29.0 ±2.0)% : (44.0 ±1.7)%
2.61 ±0.22	26.64% : 26.86% : 46.50% 26.84% : 27.10% : 46.06% 24.36% : 30.06% : 45.58% 24.81% : 30.34% : 44.84%	(25.7 ±0.9)% : (28.6 ±1.3)% : (45.7 ±0.5)%

[a] The spot size for the EDS analyses is sufficiently large to include many nanocrystals. Thus the measurements at different spots within each specimen include different collections of many nanocrystals.

XRD patterns of the exchanged $CuInS_2$ nanosheets are given in Figure 4.8. The data were most consistent with the wurtzite structure of $CuInS_2$, as in the thicker $CuInS_2$ nanoplatelets we reported previously,[23] and as has been often observed in $CuInS_2$ nanocrystals.[35-39] In this wurtzite structure, the Cu and In ions are randomly positioned on the sites in the cation sublattice.[35,36] Because of the crystallographic orientation of the starting (template) $Cu_{2-x}S$ nanosheets (see above), the wurtzite *z* axis was oriented perpendicular to the plane of the $CuInS_2$ nanosheets. As this was the thinnest dimension in the specimens of all three thicknesses, the 002 reflection remained broadened and obscured in all three patterns (Figure 4.8). Because the crystallographic *x* and *y* axes lay in the plane of the nanosheets (the largest nanosheet dimensions), the intensity of the 100 reflection increased significantly, and the intensity and sharpness of the 101 reflection to lesser degrees, as expected, with increasing nanosheet thickness. As is discussed below, an ordered, orthorhombic variant of the wurtzite structure of $CuInS_2$ exists,[40] in which the Cu and In ions are ordered into specific, alternating lattice positions. These disordered wurtzite and ordered orthorhombic structures are very difficult to distinguish on the basis of XRD patterns (see Figure 4.9), and impossible to distinguish in patterns as broad as those in Figure 4.8.

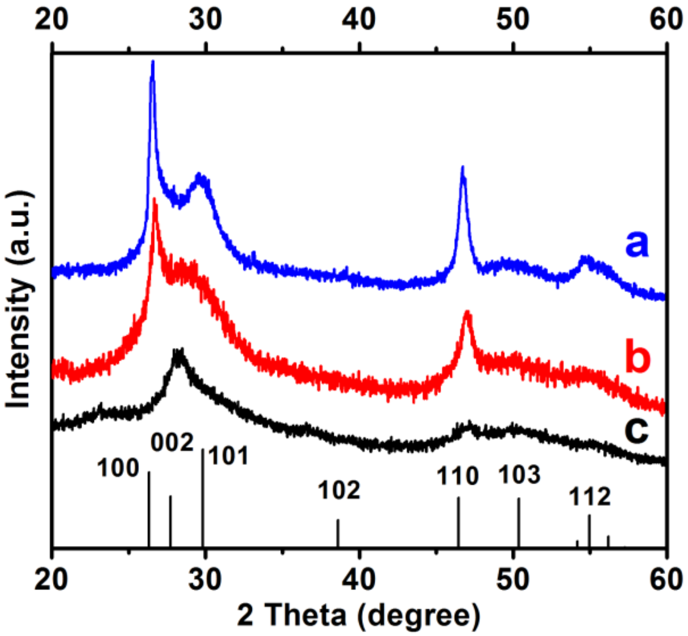

Figure 4.8. XRD patterns of $CuInS_2$ nanosheets of various thicknesses. (a) thickest nanosheets (8 MLs); (b) thinner nanosheets (6 MLs); (c) thinnest nanosheets (5 MLs).

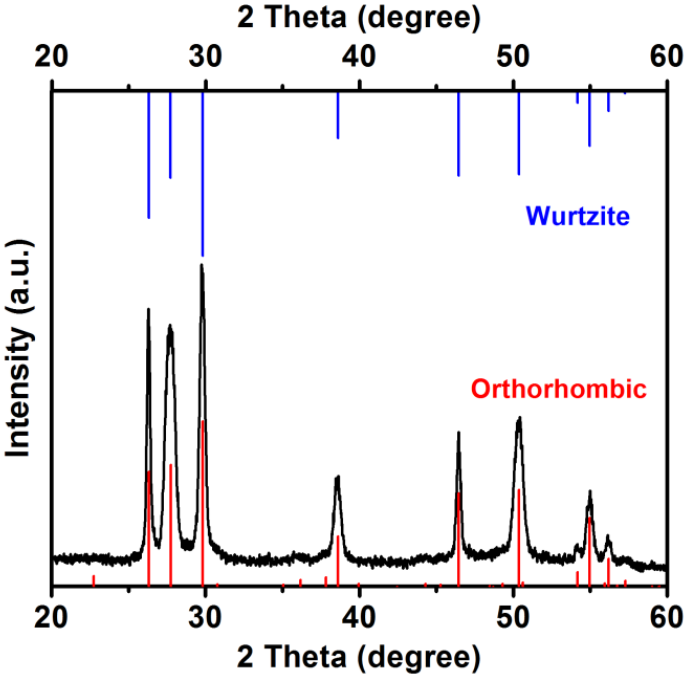

Figure 4.9. An XRD pattern of thick $CuInS_2$ (thickness 13 nm),[40] compared to the reference pattern of $CuInS_2$ in the wurtzite (blue) and orthorhombic (red) structures.

4.3.2 Extinction Spectra of $CuInS_2$ Nanosheets

Figure 4.10 provides representative extinction spectra collected from the $CuInS_2$ nanosheets of the various thicknesses. The spectra of the two thicker 6 and 8-ML specimens contained single broad features, at 612 and 721 nm, respectively, superposed on rising backgrounds. As such, these spectra resembled the absorption spectra generally obtained from $CuInS_2$ nanocrystals.[14-18]

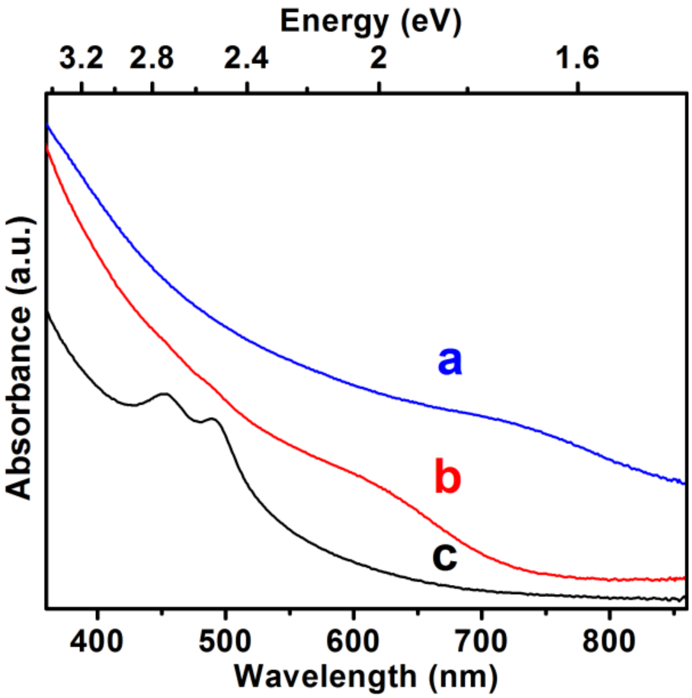

Figure 4.10. Extinction (absorption) spectra of $CuInS_2$ nanosheets of various thicknesses. (a) thickest nanosheets (8 MLs); (b) thinner nanosheets (6 MLs); (c) thinnest nanosheets (5 MLs).

However, the extinction spectra collected from the thinnest 5-ML $CuInS_2$ nanosheets always contained two readily discernible peaks, at 453 and 490 nm (Figure 4.10c). The spectra obtained from several different synthetic procedures, in which ion exchange was conducted at the standard temperature of 120 ℃, were nearly indistinguishable from Figure 4.10c (see Figure 4.11). However, the Figure-4.10c absorption features were shifted when ion exchange was conducted at other reaction temperatures. Ion exchange at the lower temperature of 60 ℃ resulted in a broadening of the spectrum and a shift of the features to higher energy (by about 80 meV, Figure 4.12). Ion exchange conducted at the higher temperature of 150 ℃ resulted in a shift of the features to lower energy (by about 20 meV, Figure 4.12), which was accompanied by the emergence of a broad peak at about 610 nm assignable to 6-ML $CuInS_2$ nanosheets (Figure

4.10b). Apparently, the 5-ML $CuInS_2$ nanosheets began to thicken at the higher ion-exchange temperature.

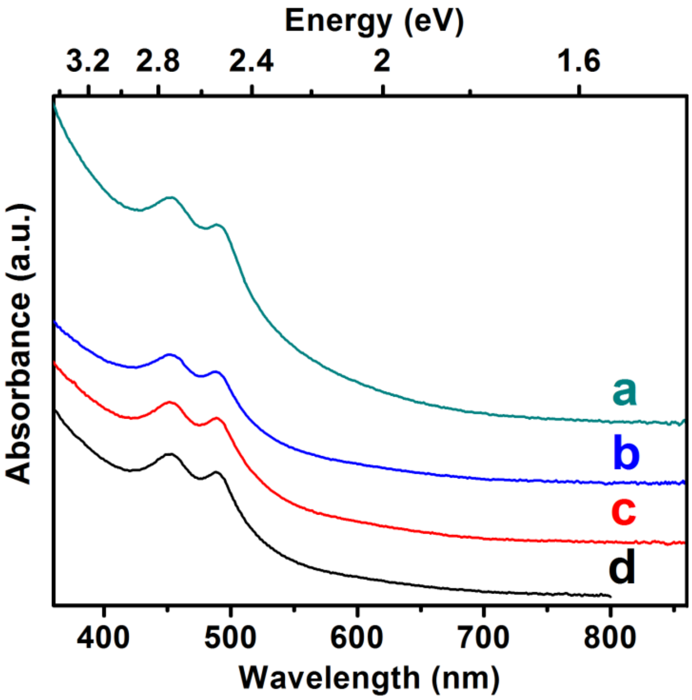

Figure 4.11. Extinction (absorption) spectra of $CuInS_2$ nanosheets resulting from ion exchange with the thinnest $Cu_{2-x}S$ nanosheets (1.73 nm, 5 MLs) under 120 ℃ for 45min. Spectra a, b, c, and d are obtained from different syntheses conducted under the same reaction conditions.

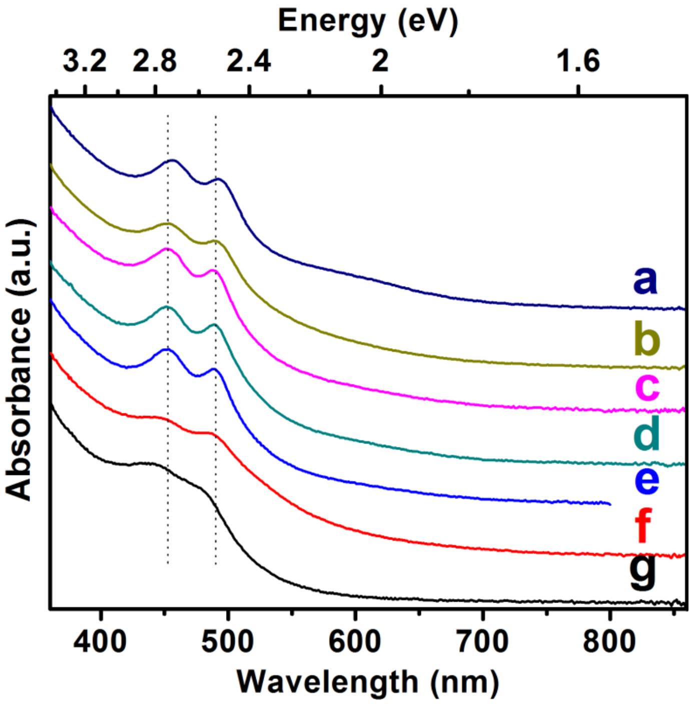

Figure 4.12. Extinction (absorption) spectra of $CuInS_2$ nanosheets resulting from ion exchange with the thinnest $Cu_{2-x}S$ nanosheets (1.73 nm, 5 MLs) under different reaction conditions, with guidelines along 453 nm and 490 nm. (a) 150 ℃, 45 min; (b), (c), (d), and (e) 120 ℃, 45 min; (f) and (g) 60 ℃, 2 h.

Bulk $CuInS_2$ in the chalcopyrite structure has a direct band gap centered at the Γ point. The highest valence band, which is triply degenerate in cubic semiconductors, is divided into A, B, and C bands by crystal-field splitting (Δ_{CF}) and the spin-orbit interaction (Δ_{SO}), as shown in Figure 4.13.[41] The B and C bands are energetically close, because of the small magnitude of Δ_{SO} in $CuInS_2$. Consequently, two near-band-edge optical transitions are observed in photoreflectivity spectra of bulk chalcopyrite $CuInS_2$, corresponding to A and unresolved BC excitons (Figure 4.13).[19,20] The energy separation between the A and BC transitions is about 10 – 20 meV at 77 – 80 K.[19,20] Our observed splitting of 200 meV (0.20 eV) was an order of magnitude larger.

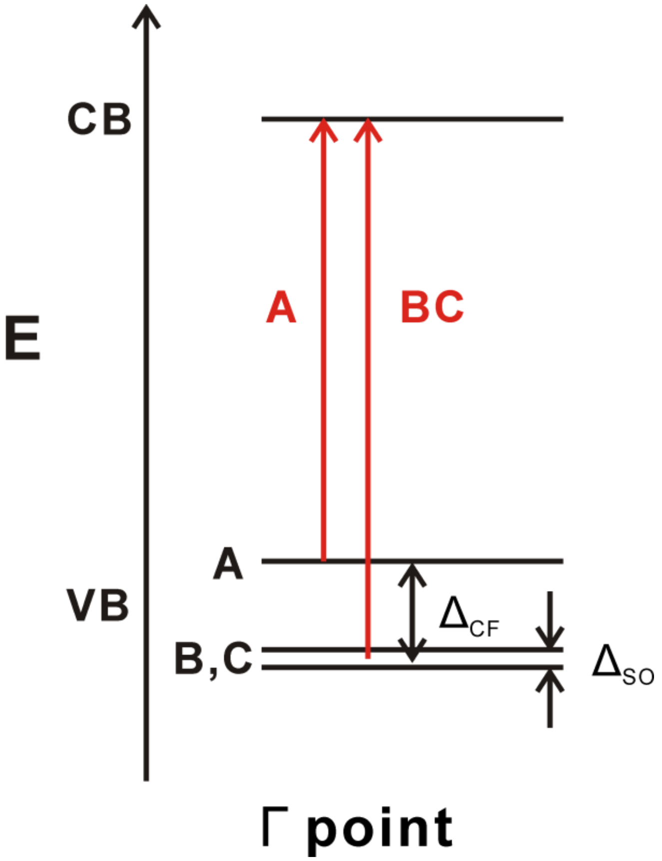

Figure 4.13. Schematic band diagram of $CuInS_2$ at the Γ point and in the vicinity of the highest A, B, and C valence bands and lowest conduction band. The optical transitions corresponding to the A and unresolved BC excitons are represented as red arrows.

As discussed above, the $CuInS_2$ nanosheets did not exhibit the conventional chalcopyrite crystal structure, but rather either a cation-disordered wurtzite structure, or a related, cation-ordered orthorhombic variant.[40] A recent band-structure calculation for the ordered variant shows a direct gap at the Γ point, and a similar splitting of the top valence band into what we have labeled A and closely spaced B and C components in Figure 4.13.[42] Thus, the chalcopyrite and orthorhombic variants have comparable electronic structures. Furthermore, the top two holes for the orthorhombic structure have quite different effective masses, 2.181 and 0.203 m_0, as do the corresponding holes masses for the chalcopyrite structure.[19,42] These differences justify the suggestion of an increased splitting between the A and BC (or AC and B) transitions due to quantum confinement in the thin $CuInS_2$ nanosheets. This proposed exciton-splitting model is further explored in the Discussion section.

4.4 Discussion

4.4.1 Cation-Exchange Process Affording $CuInS_2$ Nanosheets.

In the cation-exchange reaction described by eq 1, Cu^+ ions diffuse out of the precursor $Cu_{2-x}S$ nanosheets as In^{3+} ions diffuse in. Comparison of Figures 4.1 and 4.5 reveals that the initial pseudo-triangular and pseudo-hexagonal morphologies of the starting $Cu_{2-x}S$ nanosheets are largely retained in the product $CuInS_2$ nanosheets. Moreover, the $CuInS_2$ nanosheets do not contain large central holes. The results establish that the cation-exchange process is a topotactic reaction in which the hexagonal close-packed anion (S^{2-}) sub-lattice remains intact while the cation interdiffusion process occurs.

This outcome differs from that observed using thicker $Cu_{2-x}S$ nanoplatelets when the nanoscale Kirkendall Effect is operative.[23] In such nanoplatelets, cation exchange occurs preferentially through the thin nanoplatelet edges. When a significant reaction barrier exists for In^{3+} insertion into the $Cu_{2-x}S$ nanoplatelets, a net out-diffusion of $Cu_{2-x}S$ occurs towards the edges, ultimately yielding $CuInS_2$ nanoplatelets with large central holes, or nanorings.[23] The absence of a nanoscale Kirkendall Effect with the $Cu_{2-x}S$ nanosheets investigated here indicates either ideal exchange conditions and indium-precursor choice, or that exchange may also occur through the top and bottom facets of the thin, $Cu_{2-x}S$ nanosheets.

As reported above, the $CuInS_2$ nanosheets are obtained with discrete of 5-, 6- and 8-ML thicknesses. Thin semiconductor nanosheets and nanoribbons are commonly produced in discrete ML thickesses.[1] With such small thickness dimensions, the difference between a 5-ML and 6-ML thickness, for example, is 17%, a discrete difference. Moreover, such pseudo-2D nanocrystals tend to have crystallographically flat top and bottom facets, and remarkable thickness uniformity over their full dimensions. This is proposed to be due to the thermodynamic instability of small, incomplete steps or terraces on the top and bottom facets, which should redissolve.[1] Consequently, there is a strong tendency towards discrete, finite-ML thicknesses in specimens like the $CuInS_2$ nanosheets studied here.

4.4.2 Nature of Spectral Variations in $CuInS_2$ Nanosheets.

As described above, whereas the extinction spectra of the two thicker 6- and 8-ML $CuInS_2$ nanosheets contain only single, broadened features as is typical for $CuInS_2$ nanocrystals,[14-18] the thinnest, 5-ML nanosheets contain a well-resolved doublet feature (Figure 4.10). The peak positions for these features remain constant, at 452 nm (2.74 eV) and 489 nm (2.54 eV) for a fixed set of optimized reaction conditions. As noted above, at a lower cation-exchange temperature the doublet spectrum is broadened and shifted to slightly higher energy, we surmise due to incomplete substitution and/or the ordering of $CuInS_2$ into domains possessing some degree of additional quantum confinement in the lateral dimensions. At a higher cation-exchange temperature, the doublet spectrum is shifted to slightly lower energy, with the emergence of the broad feature corresponding to the 6-ML $CuInS_2$ nanosheets. We suspect that the slight red shift of the 5-ML spectrum is due to the background of the underlying 6-ML spectrum.

Thus, apart from the small temperature effects discussed above, the doublet spectrum of the 5-ML $CuInS_2$ nanosheets remains at fixed, invariant energies. This observed spectral invariance also strongly supports the assertion of a single, discrete thickness for these nanosheet specimens. The resolution of the doublet feature only in the thinnest, 5-ML specimens suggests that the energetic separation of the two doublet features is due to quantum confinement, which is strongest in the thinnest $CuInS_2$ nanosheets. The nature of this energetic separation is analyzed next.

4.4.3 Analysis of the Exciton Splitting in $CuInS_2$ Nanosheets.

We suggested above that the observed doublet spectrum of the thinnest, 5-ML $CuInS_2$ nanosheets is due to energetic splitting of inequivalent excitons derived from the top three A, B, and C hole bands in $CuInS_2$ (Figure 4.13). More specifically, we suggested that the energies of the B and C holes were unresolved, such that the lower-energy peak of the doublet is assigned to an A exciton, and the higher-energy peak to a BC exciton. Those assignments and the magnitude of the observed splitting are analyzed here.

We first show that the observed spectral splitting is inconsistent with the first two ($n = 1, 2$) quantum-well transitions in the $CuInS_2$ nanosheets. The bulk exciton Bohr radius in $CuInS_2$ is 4 nm:[24] therefore only the thickness dimension of the nanosheets is sufficiently small to induce quantum confinement. Consequently, the pseudo-2D nanosheets possess electronic structures corresponding to those of quantum wells.[1,43,44] Quantum wells exhibit a series of electronic transitions corresponding to confined electron and hole particle-in-a-box states approximated by eq 4.2, where E_n is the transition energy, E_g is the bulk band gap, h is Planck's constant, n is a quantum number, L_z is the thickness of the well, m_e^* is the effective mass of the electron, and m_h^* is the effective mass of the hole.[1,43,44]

$$E_n = E_g + \frac{h^2 n^2}{8 L_z^2}\left(\frac{1}{m_e^*} + \frac{1}{m_h^*}\right) \quad (4.2)$$

If the doublet feature corresponds to the first (E_1) and second (E_2) quantum-well transitions, then

$$E_n - E_g = \frac{h^2 n^2}{8L_z^2}\left(\frac{1}{m_e^*} + \frac{1}{m_h^*}\right) = K_1 n^2 \quad (4.3)$$

in which $K_1 = \frac{h^2}{8L_z^2}\left(\frac{1}{m_e^*} + \frac{1}{m_h^*}\right)$ is a constant, and the bulk band gap is $E_g = 1.53$ eV.

From eq 4.3, one may easily show that if the lowest-energy doublet peak (2.54 eV) corresponds to the $n = 1$ (E_1) quantum-well transition, then $K_1 = 1.01$ eV. The $n = 2$ (E_2) transition should appear near 5.57 eV, calculated using eq 4.3 and the same K_1 as above. The observed second doublet feature actually appears at 2.74 eV. The calculated (eq 4.3) splitting between the E_1 and E_2 quantum-well transitions is 3.03 eV, whereas the observed splitting in Figure 4.10c is 0.20 eV. Clearly, the observed splitting is too small to correspond to the first and second quantum-well transitions in the $CuInS_2$ nanosheets, and therefore both observed features are associated with the E_1 transition.

As noted above, the A and B, C holes at the Γ point in the bulk band structure of chalcopyrite $CuInS_2$ differ in energy by 10 – 20 meV (Figure 4.13).[19,20] However, the A, B, and C holes do not have the same effective masses, and thus quantum confinement will further separate the energies of the corresponding transitions associated with these inequivalent holes. Knowledge of the effective masses m_e^*, and m_h^* for the A, B, and C holes would allow estimation of the energy splittings, using eq 4.4, between the A, B, and C transitions associated with the $n = 1$ quantum-well state. Such splittings are directly analogous to the heavy-hole, light-hole splittings observed in the absorption spectra of GaAs quantum wells,[43] and CdSe nanosheets and quantum belts.[1]

$$E_n - E_g = \frac{h^2 n^2}{8L_z^2}\left(\frac{1}{m_e^*} + \frac{1}{m_h^*}\right) = K_2\left(\frac{1}{m_e^*} + \frac{1}{m_h^*}\right) \quad (4.4)$$

in which $K_2 = \frac{h^2 n^2}{8L_z^2}$ is a constant, and the bulk band gap is $E_g = 1.53$ eV.

A few reports of the effective carrier masses are available for $CuInS_2$, from which the corresponding exciton splittings (valence-band splittings) may be approximated. A simulation of the photoreflectivity spectrum of bulk, chalcopyrite $CuInS_2$ afforded $m_e^* = 0.23\ m_0$, $m_A = 2.87\ m_0$, $m_B = 1.2\ m_0$, and $m_C = 1.2\ m_0$.[19] Thus, the lighter, B and C holes were found to have the same effective masses. If the lowest-energy doublet peak (2.54 eV) corresponds to the heavy-hole-electron transition E_{hh}, K_2 is calculated using eq 4.4 as $0.215 m_0$ eV. Then the light-hole-electron transition is $E_{lh} = 2.64$ eV, calculated with eq 4.4 and the same K_2 as above. These values produce a splitting between the A and BC excitons of 0.10 eV, close to our observed splitting of 0.20 eV.

As noted above, the $CuInS_2$ nanosheets do not exhibit the chalcopyrite structure, but rather either a wurtzite, or ordered, orthorhombic variant of the wurtzite structure. The effective carrier masses have been determined theoretically for the ordered wurtzite variant, and reported to be $m_e^* = 0.173\ m_0$, $m_A = 2.181\ m_0$, and $m_B = 0.203\ m_0$.[42] The effective mass of the C hole was not reported, but visual inspection of the calculated band diagram[42] indicates that it has a heavier mass comparable to m_A. These values produce a splitting between the putative AC and B excitons of 0.72 eV, using the same model (eq 4.4) as that for chalcopyrite structure above.

Notably, the observed spectral splitting of 0.20 eV falls between the values estimated above for chalcopyrite (0.10 eV) and orthorhombic (0.72 eV) $CuInS_2$ quantum wells. Both estimated values are within an order of magnitude of the observed value. We further note that we have used bulk effective masses in the eqs-4.2, 4.3 and 4.4 calculations, whereas the actual effective masses in the quantum-confined nanosheets will likely differ. Given that neither the structure nor the effective carrier masses are well known for the $CuInS_2$ nanosheets, we assert that the reasonable agreement between the estimated exciton splittings and the observed spectral splitting is sufficient to support this inequivalent-exciton-splitting model. Clearly, the observed splitting is of the correct order of magnitude for excitons derived from heavy and light holes assigned reasonable effective masses for $CuInS_2$. Moreover, as noted above, this is essentially the same exciton-splitting phenomenon that is now well accepted for quantum-well nanostructures derived from III-V and II-VI semiconductors.[1,43]

The argument above claims that the observed spectral splitting in the 5-ML $CuInS_2$ nanosheets is primarily due to quantum confinement, and specifically to the differing quantum confinement experienced by the A, B, and C excitons due to their differing hole effective masses. Such splitting will decrease in magnitude in thicker nanosheets due to the decreasing confinement, and become more difficult to resolve. A simple eq-4.4 calculation using either the chalcopyrite or orthorhombic effective masses produce 0.05 eV or 0.36 eV, respectively, showing that the spectral splitting by the proposed mechanism is reduced by half in 6-ML $CuInS_2$ nanosheets. A reduction by half of the observed spectral splitting for the 5-ML nanosheets (0.20 eV, 37 nm in wavelength) corresponds to a 30-nm wavelength splitting within the 612-nm feature in the spectrum of the 6-ML nanosheets. Given the spectral broadening that accompanies the shift of the 6-ML nanosheet spectrum to lower energy (Figure 4.10), we propose that the smaller exciton splitting becomes unresolved.

4.5 Conclusions

The structured extinction spectrum reported here for the thinnest, 5-ML $CuInS_2$ nanosheets contrasts markedly with the unresolved spectra typical of $CuInS_2$ nanocrystals.[14-18] We propose herein an exciton-splitting model to explain the observed spectral splitting, based on the inequivalency of the top A, B, and C holes in the bulk band structure of $CuInS_2$.[19-22] The model accounts semi-quantitatively for the magnitude of the observed splitting, and is conceptually analogous to the heavy-hole, light-hole splitting well known in the absorption spectra of III-V quantum wells and pseudo-2D II-VI nanocrystals.[1,43] Moreover, because this exciton splitting is largely due to quantum confinement, the loss of resolved exciton splitting in the spectra of larger $CuInS_2$ nanocrystals is also rationalized.

4.6 References

1. Wang, F.; Wang, Y.; Liu, Y.-H.; Morrison, P. J.; Loomis, R. A.; Buhro, W. E. *Acc. Chem. Res.* **2015**, *48*, 13.

2. Joo, J.; Son, J. S.; Kwon, S. G.; Yu, J. H.; Hyeon, T. *J. Am. Chem. Soc.* **2006**, *128*, 5632.

3. Ithurria, S.; Dubertret, B. *J. Am. Chem. Soc.* **2008**, *130*, 16504.

4. Son, J. S.; Wen, X.-D.; Joo, J.; Chae, J.; Baek, S.-i.; Park, K.; Kim, J. H.; An, K.; Yu, J. H.; Kwon, S. G.; Choi, S.-H.; Wang, Z.; Kim, Y.-W.; Kuk, Y.; Hoffmann, R.; Hyeon, T. *Angew. Chem., Int. Ed.* **2009**, *48*, 6861.

5. Ithurria, S.; Tessier, M. D.; Mahler, B.; Lobo, R. P. S. M.; Dubertret, B.; Efros, A. L. *Nat Mater* **2011**, *10*, 936.

6. Ithurria, S.; Bousquet, G.; Dubertret, B. *J. Am. Chem. Soc.* **2011**, *133*, 3070.

7. Liu, Y.-H.; Wayman, V. L.; Gibbons, P. C.; Loomis, R. A.; Buhro, W. E. *Nano Lett.* **2010**, *10*, 352.

8. Liu, Y.-H.; Wang, F.; Wang, Y.; Gibbons, P. C.; Buhro, W. E. *J. Am. Chem. Soc.* **2011**, *133*, 17005.

9. Wang, Y.; Zhang, Y.; Wang, F.; Giblin, D. E.; Hoy, J.; Rohrs, H. W.; Loomis, R. A.; Buhro, W. E. *Chem. Mater.* **2014**, *26*, 2233.

10. Li, Z.; Peng, X. *J. Am. Chem. Soc.* **2011**, *133*, 6578.

11. Battaglia, D.; Peng, X. *Nano Lett.* **2002**, *2*, 1027.

12. Gary, D. C.; Terban, M. W.; Billinge, S. J. L.; Cossairt, B. M. *Chem. Mater.* **2015**, *27*, 1432.

13. Morrison, P. J.; Loomis, R. A.; Buhro, W. E. *Chem. Mater.* **2014**, *26*, 5012.

14. Xie, R.; Rutherford, M.; Peng, X. *J. Am. Chem. Soc.* **2009**, *131*, 5691.

15. van der Stam, W.; Berends, A. C.; de Mello Donega, C. *ChemPhysChem* **2016**, *17*, 559.

16. So, D.; Konstantatos, G. *Chem. Mater.* **2015**, *27*, 8424.

17. Zhong, H.; Lo, S. S.; Mirkovic, T.; Li, Y.; Ding, Y.; Li, Y.; Scholes, G. D. *ACS Nano* **2010**, *4*, 5253.

18. Li, L.; Pandey, A.; Werder, D. J.; Khanal, B. P.; Pietryga, J. M.; Klimov, V. I. *J. Am. Chem. Soc.* **2011**, *133*, 1176.

19. Syrbu, N. N.; Tiginyanu, I. M.; Nemerenco, L. L.; Ursaki, V. V.; Tezlevan, V. E.; Zalamai, V. V. *J. Phys. Chem. Solids* **2005**, *66*, 1974.

20. Eberhardt, J.; Metzner, H.; Schulz, K.; Reislöhner, U.; Hahn, T.; Cieslak, J.; Witthuhn, W.; Goldhahn, R.; Hudert, F.; Kräußlich, J. *J. Appl. Phys.* **2007**, *102*, 033503.

21. Ho, C.-H.; Lo, S.-F.; Chi, P.-C. *J. Electrochem. Soc.* **2010**, *157*, H219.

22. Yakushev, M. V.; Mudryi, A. V.; Feofanov, Y.; Ivaniukovich, A. V.; Victorov, I. V. *Thin Solid Films* **2006**, *511–512*, 130.

23. Mu, L.; Wang, F.; Sadtler, B.; Loomis, R. A.; Buhro, W. E. *ACS Nano* **2015**, *9*, 7419.

24. Czekelius, C.; Hilgendorff, M.; Spanhel, L.; Bedja, I.; Lerch, M.; Müller, G.; Bloeck, U.; Su, D.-S.; Giersig, M. *Adv. Mater.* **1999**, *11*, 643.

25. van der Stam, W.; Akkerman, Q. A.; Ke, X.; van Huis, M. A.; Bals, S.; de Mello Donega, C. *Chem. Mater.* **2015**, *27*, 283.

26. Wu, W.-Y.; Chakrabortty, S.; Chang, C. K. L.; Guchhait, A.; Lin, M.; Chan, Y. *Chem. Mater.* **2014**, *26*, 6120.

27. Potter, R. W. *Econ. Geol.* **1977**, *72*, 1524.

28. Sigman, M. B.; Ghezelbash, A.; Hanrath, T.; Saunders, A. E.; Lee, F.; Korgel, B. A. *J. Am. Chem. Soc.* **2003**, *125*, 16050.

29. Hsu, S.-W.; On, K.; Tao, A. R. *J. Am. Chem. Soc.* **2011**, *133*, 19072.

30. Li, X.; Shen, H.; Niu, J.; Li, S.; Zhang, Y.; Wang, H.; Li, L. S. *J. Am. Chem. Soc.* **2010**, *132*, 12778.

31. Yi, L.; Gao, M. *Cryst. Growth Des.* **2011**, *11*, 1109.

32. Li, X.; Wang, M.; Shen, H.; Zhang, Y.; Wang, H.; Li, L. S. *Chem. - Eur. J.* **2011**, *17*, 10357.

33. Evans, H. T., Jr. *Science* **1979**, *203*, 356.

34. Evans, H. T., Jr. *Z. Kristallogr.* **1979**, *150*, 299.

35. Pan, D.; An, L.; Sun, Z.; Hou, W.; Yang, Y.; Yang, Z.; Lu, Y. *J. Am. Chem. Soc.* **2008**, *130*, 5620.

36. Qi, Y.; Liu, Q.; Tang, K.; Liang, Z.; Ren, Z.; Liu, X. *J. Phys. Chem. C* **2009**, *113*, 3939.

37. Lu, X.; Zhuang, Z.; Peng, Q.; Li, Y. *CrystEngComm* **2011**, *13*, 4039.

38. Akkerman, Q. A.; Genovese, A.; George, C.; Prato, M.; Moreels, I.; Casu, A.; Marras, S.; Curcio, A.; Scarpellini, A.; Pellegrino, T.; Manna, L.; Lesnyak, V. *ACS Nano* **2015**, *9*, 521.

39. van der Stam, W.; Berends, A. C.; Rabouw, F. T.; Willhammar, T.; Ke, X.; Meeldijk, J. D.; Bals, S.; de Mello Donega, C. *Chem. Mater.* **2015**, *27*, 621.

40. Cholula-Diaz, J. L.; Wagner, G.; Friedrich, D.; Oeckler, O.; Krautscheid, H. *Dalton Transactions* **2015**, *44*, 14227.

41. Rowe, J. E.; Shay, J. L. *Phys. Rev. B* **1971**, *3*, 451.

42. Tomić, S.; Bernasconi, L.; Searle, B. G.; Harrison, N. M. *J. Phys. Chem. C* **2014**, *118*, 14478.

43. Dingle, R. *Confined Carrier Quantum States in Ultrathin Semiconductor Heterostructures*; Springer Berlin Heidelberg: Berlin, Heidelberg, 1975.

44. Yoffe, A. D. *Advances in Physics* **1993**, *42*, 173.

Chapter 5

Conclusions and Future Work

5.1 Conclusions

In this dissertation, synthesis of 2D $CuInS_2$ nanocrystals and study of their optical properties are reported. Specifically, the ion-exchange synthetic method accompanied by the nanoscale Kirkendall Effect under some reaction conditions, and exciton splitting in the extinction spectra of thin $CuInS_2$ nanosheets are discussed in detail.

In Chapter 2, hexagonal $CuInS_2$ NPs are first prepared using a one-pot method at 150 ℃, the size and morphology of which are found difficult to control. The increasing In/Cu ratio in the mixture as the reaction progresses, as monitored by EDS, suggests that Cu^+ reacts with S^{2-} first, forming a binary intermediate, likely Cu_2S. In^{3+} then incorporates into and reacts with Cu_2S to afford $CuInS_2$ composition. With this proposed pathway, an ion-exchange method is developed in Chapter 3 involving the purposeful synthesis of template $Cu_{2-x}S$ NPs followed by insertion of In^{3+} by ion exchange.

The morphology of $CuInS_2$ NPs by ion-exchange method is found to remarkably rely on the ion-exchange conditions. Higher exchange temperature and/or more ionic indium precursors produce intact $CuInS_2$ NPs with preserved size and morphology from the template $Cu_{2-x}S$ NPs, because of the comparable effective out- and in-diffusion rate of Cu^+ and In^{3+}, respectively. However, if lower exchange temperature and/or more covalent indium precursors are employed, the exchange process may occur in the reaction-limited regime. In that condition, the low relative rate of incorporation of In^{3+} activates the nanoscale Kirkendall Effect, consequently resulting in hollow-centered $CuInS_2$ nanocrystals.[1] Understanding the process of ion exchange and the origin of the nanoscale Kirkendall Effect assist in choosing proper reaction conditions for formation of intact NPs or intentional nanorings of $CuInS_2$ and other multinary semiconductor nanomaterials.

III-V quantum wells and pseudo-2D II-VI nanocrystals are well known for the heavy-hole, light-hole splitting in their absorption spectra,[2,3] but such a phenomenon has not been previously reported for $CuInS_2$ nanocrystals. We show herein in Chapter 4 a similar observation in the extinction spectra of thin $CuInS_2$ nanosheets. $CuInS_2$ nanosheets having three thicknesses are prepared by ion exchange with 5-, 6-, and 8-ML $Cu_{2-x}S$ nanosheets. $SnBr_4$ or HCl is employed as the morphology-control additive. The thinnest $CuInS_2$ nanosheets exhibit a well-resolved doublet feature in the extinction spectra. The exciton splitting is attributed to different effective masses of the top A, B, and C holes in the bulk band structure of $CuInS_2$[4-7], which is analogous to the heavy-hole, light-hole splitting mentioned above. Calculations also suggest the reduced energy splitting in thicker nanosheets due to weaker quantum confinement, resulting in that the resolved doublet feature is not observed in $CuInS_2$ nanosheets having the two larger thicknesses.

5.2 Future Work

First of all, to confirm the origin of the exciton splitting observed in $CuInS_2$ nanosheets shown in Chapter 4, theoretical calculations are being conducted by our collaborator Professor Li Yang. We will then compare the experimental results with calculations to better address the exciton splitting.

Moreover, PL has been reported for $CuInS_2$ dots previously,[8-11] but to the best of our knowledge, not for 2D $CuInS_2$ nanocrystals. Although the 5-ML $CuInS_2$ nanosheets we report in Chapter 4 display well-resolved doublet exciton feature in the extinction spectra, no PL is evident, probably due to surface defects. The reaction conditions need to be optimized to produce nanosheets with better surface passivation, to prevent electron and hole surface trapping, thus increasing PL efficiencies.

Finally, this dissertation focuses on $CuInS_2$ nanocrystals. But other ternary I-III-VI_2 semiconductor nanomaterials prepared using ion-exchange methods are also worthy of investigation, such as $CuInSe_2$, $CuGaS_2$, $CuGaSe_2$, and $CuIn_xGa_{1-x}S_ySe_{2-y}$. Preliminary research on ion-exchange preparation of $CuGaS_2$ using similar protocols as in Chapter 3 was conducted. Ion exchange between $GaCl_3$ and template $Cu_{2-x}S$ NPs at 200 ℃ produced $CuGaS_2$ nanorings, although intact $CuInS_2$ NPs were obtained using $InCl_3$ under the same temperature. The more severe erosion in $CuGaS_2$ NPs than that in $CuInS_2$ NPs with corresponding metal (Ga or In) precursors under the same reaction conditions may be ascribed to the higher covalence of Ga precursors, according to the reaction mechanism we propose in Chapter 3. More experiments need to be conducted to optimize the choice of reagents and reaction conditions for 2D $CuGaS_2$ and other ternary I-III-VI_2 nanocrystals, and further confirm the proposed mechanism. Furthermore, this ion-exchange method may be also be applied to more complicated nanomaterials, such as quaternary Cu_2ZnSnS_4 consisting of only earth-abundant and non-toxic elements, for better and broader choices of absorption materials in thin film solar cells.

5.3 References

1. Mu, L.; Wang, F.; Sadtler, B.; Loomis, R. A.; Buhro, W. E. *ACS Nano* **2015**, *9*, 7419.

2. Wang, F.; Wang, Y.; Liu, Y.-H.; Morrison, P. J.; Loomis, R. A.; Buhro, W. E. *Acc. Chem. Res.* **2015**, *48*, 13.

3. Dingle, R. *Confined Carrier Quantum States in Ultrathin Semiconductor Heterostructures*; Springer Berlin Heidelberg: Berlin, Heidelberg, 1975.

4. Syrbu, N. N.; Tiginyanu, I. M.; Nemerenco, L. L.; Ursaki, V. V.; Tezlevan, V. E.; Zalamai, V. V. *J. Phys. Chem. Solids* **2005**, *66*, 1974.

5. Eberhardt, J.; Metzner, H.; Schulz, K.; Reislöhner, U.; Hahn, T.; Cieslak, J.; Witthuhn, W.; Goldhahn, R.; Hudert, F.; Kräußlich, J. *J. Appl. Phys.* **2007**, *102*, 033503.

6. Ho, C.-H.; Lo, S.-F.; Chi, P.-C. *J. Electrochem. Soc.* **2010**, *157*, H219.

7. Yakushev, M. V.; Mudryi, A. V.; Feofanov, Y.; Ivaniukovich, A. V.; Victorov, I. V. *Thin Solid Films* **2006**, *511–512*, 130.

8. van der Stam, W.; Berends, A. C.; de Mello Donega, C. *ChemPhysChem* **2016**, *17*, 559.

9. Kolny-Olesiak, J.; Weller, H. *ACS Appl. Mater. Interfaces* **2013**, *5*, 12221.

10. Knowles, K. E.; Nelson, H. D.; Kilburn, T. B.; Gamelin, D. R. *J. Am. Chem. Soc.* **2015**, *137*, 13138.

11. So, D.; Konstantatos, G. *Chem. Mater.* **2015**, *27*, 8424.